PERGAMON

Progress in Materials Science 44 (1999) 291–433

Progress in Materials Science

Amorphous and nanocrystalline materials for applications as soft magnets

Michael E. McHenry*, Matthew A. Willard, David E. Laughlin

Department of Materials Science and Engineering, Carnegie Mellon University, Pittsburgh, Pennsylvania 15213, USA

Received 30 November 1998

Abstract

This review seeks to summarize the recent developments in the synthesis, structural characterization, properties, and applications in the fields of amorphous, bulk amorphous, and nanocrystalline soft magnetic materials. Conventional physical metallurgical approaches to improving soft ferromagnetic properties have relied on the optimization of chemical and microstructural features. Within the last decade, the development and rapid increase in research of nanocrystalline materials has shown that through proper modifications, revolutionary contributions can be made to better materials' properties. A wide range of materials' properties are examined in this review, including: kinetics and thermodynamics, structure, microstructure, and intrinsic and extrinsic magnetic properties.

Contents

1. Introduction and historical perspective 300
   1.1. Technical considerations 302

2. Alloy design issues. 306
   2.1. Magnetic dipole moments and magnetization. 307

* Corresponding author. Tel.: +1-412-268-2703; fax: +1-412-268-3113.
E-mail address: mm7g@andrew.cmu.edu (M.E. McHenry).

0079-6425/99/$ - see front matter
PII: S0079-6425(99)00002-X

2.2. Ferromagnetic ordering (Curie) temperatures . . . 310
2.3. Magnetocrystalline anisotropy and magnetostriction . . . 313
2.4. Magnetic domains and domain wall mobility . . . 315
2.5. AC magnetic response . . . 317
2.6. Considerations of glass forming ability and crystallization . . . 318

3. Synthesis of nanoparticles, amorphous, bulk amorphous and nanocrystalline alloys . . . 321
3.1. Powder synthesis of nanoparticles and nanoencapsulates . . . 322
3.1.1. Carbon arc synthesis . . . 322
3.1.2. Plasma torch synthesis . . . 312
3.1.3. Mechanical milling techniques . . . 327
3.1.4. Powder consolidation . . . 330
3.2. Rapid solidification processing . . . 331
3.3. Solidification processing of bulk amorphous alloys . . . 333
3.4. Primary nanocrystallization of amorphous precursors . . . 333

4. Thermodynamic and transformation kinetic considerations for amorphous and nanocrystalline materials . . . 335
4.1. Calorimetry and stability of bulk amorphous materials . . . 337
4.2. Primary and secondary crystallization events in nanocrystalline alloys . . . 340
4.2.1. FINEMET alloys . . . 340
4.2.2. NANOPERM alloys . . . 342
4.2.3. HITPERM alloys . . . 343
4.2.4. Other alloys . . . 343
4.3. Surface crystallization kinetics . . . 343
4.4. Crystallization kinetics . . . 344
4.4.1. FINEMET alloys . . . 344
4.4.2. NANOPERM alloys . . . 346
4.4.3. HITPERM alloys . . . 346
4.4.4. Other alloys . . . 346
4.5. Ordering and structural phase transitions in nanocrystalline alloys . . . 347
4.5.1. Nanoparticles and nanoencapsulates . . . 347
4.5.2. FINEMET alloys . . . 349
4.5.3. NANOPERM alloys . . . 350
4.5.4. HITPERM alloys . . . 350

5. Structure and microstructure of amorphous and nanocrystalline alloys . . . 352
5.1. Background information . . . 352
5.1.1. Amorphous alloys . . . 352
5.1.2. Nanocrystalline phases . . . 354
5.1.3. Microstructural characterization and spectroscopic analysis (amorphous and nanocrystalline alloys) . . . 355
5.2. Experimental observations: X-ray scattering and EXAFS . . . 358
5.2.1. FINEMET alloys . . . 362
5.2.2. NANOPERM alloys . . . 363
5.2.3. HITPERM alloys . . . 363
5.3. Experimental observations: neutron scattering . . . 364
5.3.1. Nanoparticle powders . . . 364

5.3.2. Nanocrystalline materials . . . 365
5.4. Experimental observations: microscopy . . . 365
5.4.1. Nanoparticle powders . . . 365
5.4.2. FINEMET alloys . . . 367
5.4.3. NANOPERM alloys . . . 370
5.4.4. HITPERM alloys . . . 374
5.4.5. Other alloys . . . 376
5.5. Experimental observations: Mössbauer spectcroscopy . . . 377
5.5.1. FINEMET alloys . . . 377
5.5.2. NANOPERM alloys . . . 377
5.5.3. HITPERM alloys . . . 382

6. Intrinsic magnetic properties . . . 382
6.1. Magnetic dipole moments . . . 382
6.1.1. Amorphous alloys . . . 382
6.1.2. Nanocrystalline alloys . . . 385
6.2. Magnetic exchange interactions and T-Dependent ferromagnetic response . 387
6.2.1. Amorphous alloys . . . 387
6.2.2. Nanocrystalline alloys . . . 391

7. Extrinsic magnetic properties . . . 395
7.1. Magnetic anisotropy and magnetostriction . . . 395
7.1.1. Amorphous alloys . . . 395
7.1.2. Weakly exchange coupled nanocrystalline alloys . . . 396
7.1.3. Strongly exchange coupled nanocrystalline alloys . . . 396
7.2. Induced anisotropies . . . 402
7.3. Magnetic coupling in two phase microstructures . . . 403
7.4. Experimental observations in bulk amorphous alloys . . . 410
7.5. Experimental observations in nanocrystalline alloys . . . 412
7.5.1. FINEMET alloys . . . 412
7.5.2. NANOPERM alloys . . . 417
7.5.3. HITPERM alloys . . . 419

8. Applications of amorphous and nanocrystalline materials . . . 420
8.1. Amorphous materials . . . 420
8.2. Nanocrystalline materials . . . 422
8.2.1. FINEMET alloys . . . 422
8.2.2. NANOPERM alloys . . . 422
8.2.3. HITPERM alloys . . . 423

9. Conclusions . . . 425

Acknowledgements . . . 426

References . . . 426

Nomenclature

a	Lattice parameter
A	Exchange stiffness
A_{am}	Exchange stiffness amorphous phase
A_{cx}	Exchange stiffness, crystalline phase
A_{W}	Domain wall area
$A(\mathbf{r})$	Local exchange stiffness
$\mathbf{B}$, B	Induction, flux density
B_{Θ}	Breadth of an X-ray peak
B_{hf}	Hyperfine field
B_{max}	(AC) induction amplitude
B_{r}	Remanent induction
B_{s}	Saturation induction
$B_J(x)$	Brillouin function
$B_S(x)$	Spin-only Brillouin function
c	Speed of light
C	Specific heat
C_V,C_P	Specific heat, constant V, P
C_M,C_H	Specific heat, constant M, H
C_{h},C_{e}	Power loss coefficients
d	Skin depth
d_{p}	Atomic plane spacing
dl	Displacement
D	Diffusivity
D_{A}	A-atom diffusivity
D_{B}	B-atom diffusivity
D, D_{g}	Grain size
E	Activation energy
E_{F}	Fermi energy
E_{p}	Potential energy
E_{γ}	Energy of gamma radiation
f	Frequency
F_m	Helmholtz free energy
$g(r)$	Pair correlation function
$g(E)$	Density of states
$g_{+}(E)$	Spin up density of states
$g_{-}(E)$	Spin down density of states
h	Planck's constant
H	Magnetic field
$\mathbf{H}_{\mathrm{a}}$	Applied magnetic field vector
H_{c}	Coercive field
H_{INT}	Internal magnetic field

H_K	Anisotropy field
H_{m}	Field amplitude (AC)
H_{mix}	Heat of mixing
H_{N}	Domain nucleation field
H_0	Hyperfine splitting
H_{W}	Domain wall pinning field
I	Current
I	Intensity
J, J_{ex}	Exchange energy density
k_{B}	Boltzmann constant
k	Equilibrium constant
K	Magnetic anisotropy
K_{eff}	Effective magnetic anisotropy
K_{l}	Magnetic anisotropy lead term
$K_{\mathrm{l}}(\mathbf{r})$	Local anisotropy lead term
K_{u}	Uniaxial magnetic anisotropy
k^*	'Structural' anisotropy
k_0	Macroscopic anisotropy
l	Length
ℓ	Angular momentum quantum number
ℓ_{s}	Structural fluctuation length
$l(R)$	Dipolar magnetic anisotropy
L	Latent heat
L_{ex}	Exchange correlation length
L_{am}	L_{ex}-amorphous phase
L^*	Modified L_{ex}
Ln	Lanthanide
$\mathbf{M}$, M	Magnetization (avg), magnitude
M	Metalloid
M_{s}	Saturation magnetization
$M_{\mathrm{s}}^{\mathrm{am}}$	M_{s}-amorphous phase
$\mathbf{m}$, m	Reduced magnetization, magnitude
n	Power law exponent
n_e	Number of electrons
n_+	Number of spin-up electrons
n_-	Number of spin-down electrons
N_{v}	Number of atoms/unit volume
N_{p}	Number of atomic planes
N	Number of grains
N_{d}	Number of d-electrons
N_{eq}	Equilibrium number of atomic planes in a domain wall
N_m	Dipoles per unit volume
N_{s}	Number of s-electrons

$N_{\Uparrow}$	Number of spin-up electrons
$N_{\Downarrow}$	Number of spin-down electrons
p	Momentum
p_e	Nucleation rate exponent
$P(B_{hf})$	Hyperfine field distribution
P_h	Hysteresis power loss
P_e	Eddy current power loss
P_{TOT}	Total power loss
q_e	Growth rate exponent
q	Momentum (X-ray scattering)
$q(R)$	Quadrupolar anisotropy coefficient
r	Radius
R, $R(t)$	Resistance, time dependent R
R_c	Cooling rate
$\mathbf{S}$	Spin angular momentum vector
S	Hoffmann ripple parameter
t	Time
t_{eq}	Thickness
T	Temperature
T_a	Annealing temperature
T_C	Curie temperature
T_C^{am}	Curie temperature, amorphous phase
T_C^{cr}	Curie temperature, crystalline phase
T_E	Eutectic temperature
TE	Early transition metal
T_g	Glass transition temperature
T_L	Liquidus temperature
TL	Late transition metal
T_{rg}	Reduced glass transition T
T_x	Crystallization temperature
T_{x1}	Primary crystallization T
T_{x2}	Secondary crystallization T
X	Volume fraction
X_{am}	Volume fraction amorphous phase
x_E	Eutectic temperature
v	Velocity
V	Voltage
w_i	Néel pair anisotropy energy
W	Band-width
W_h	Hysteresis loss
Z_n	Coordination number
Z	Chemical valence
Z_M	Magnetic valence

α	Power law exponent
β	Critical exponent
θ	Angle
θ_B	Bragg angle
Δ	Quadrupole splitting
δ	Mössbauer line position
δ_{ex}	Reduced exchange fluctuation
$\delta_{0\ ex}$	Reduced exchange fluctuation (0 K)
δ_+,δ_-	Asymmetric reduced exchange fluctuation
δ_W	Domain (Bloch) wall width
δ^*	Critical crystallite size
δ_0	Maximum crystallite size
ΔD_+, ΔD_-	Near neighbor distance fluctuation
ΔT_x	Width of supercooled region
ΔH_f	Heat of formation
ΔH_{mix}	Enthalpy of mixing
ΔH_x	Heat of crystallization
ΔJ	Exchange fluctuation
ΔZ	Valence difference
ϕ	Flux
Γ	Mössbauer line width
γ	Gamma radiation
γ_{ex}	Exchange interaction parameter
γ_{am}	γ parameter amorphous phase
γ_s	γ parameter crystalline phase
γ_{wall}	Domain wall interfacial energy
$\gamma(x)$	γ_{wall}, local
γ_{exc}	Exchange contribution to γ_{wall}
γ_K	Anisotropy contribution to γ_{wall}
κ	Magnetic hardness parameter
Λ	Intergranular spacing parameter
λ	X-ray wavelength
λ_W	Weiss molecular field constant
λ_{111}	Magnetostriction-111 direction
λ_{100}	Magnetostriction-100 direction
λ_S	Saturation magnetostriction
λ_{am}	Magnetostriction coefficient, amorphous phase
λ_{cr}	Magnetostriction coefficient, crystalline phase
μ_X	X-ray absorption coefficient
μ	Permeability
μ'	Real permeability
μ''	Imaginary permeability
μ_m	Magnetic dipole moment

μ_{av}	Average dipole moment
μ_{matrix}	Matrix atom dipole moment
μ_B	Bohr magneton
μ_i	Initial permeability
μ_M^{atom}	Atomic dipole moment
μ_0	Permeability of free space
π	Pi
σ	Electrical conductivity
τ	Lifetime, Time constant
τ_r	Reduced temperature
χ	Magnetic susceptibility
$\chi(k)$	EXAFS oscillations
ρ_e	Resistivity
ρ	Density
$\rho(r)$	Atom density
Ω	Atomic volume
Å	Angstrom
nm	nanometer
NANOPERM	Fe–M–B–Cu alloys
FINEMET	Fe–M–Si–B–Cu alloys
HITPERM	Fe–Co–M–B–Cu alloys
AC	Alternating current
AFM	Atomic force microscopy
APFIM	Atom probe field ion microscopy
BCC	Body centered cubic
DC	Direct current
DRPHS	Dense random packing of hard spheres
DSC	Differential scanning calorimetry
DTA	Differential thermal analysis
CEMS	CoConversion electron Mössbauer spectroscopy
DSP	Dislocation solute pumping
ED	Electron diffraction
EDS	Energy dispersive X-ray spectroscopy
EDX	Energy dispersive X-ray analysis
EELS	Electron energy loss spectroscopy
EFM	Energy filtered microscopy
EFTEM	Energy filtered TEM
EXAFS	Extended X-ray absorption fine structure
FCC	Face centered cubic
FIM	Field ion microscopy
FWHM	Full width at half maximum
GFA	Glass forming ability
GW	Gao–Wang kinetics

HCP	Hexagonal close packed
HRTEM	High resolution TEM
HV	Vickers hardness
IPU	Integrated power unit
JMA	Johnson–Mehl–Avrami kinetics
KP	Kissinger plot
LKKR	Layer Korringa–Kohn–Rostoker
LRO	Long range order
MA	Mechanical alloying
MAE	Magnetic after effect
MEA	More electric aircraft
MFM	Magnetic force microscopy
MOKE	Magneto-optic Kerr effect
MRO	Medium range order
NM	Noble metal
NN	Nearest neighbors
RDF	Radial distribution function
PEELS	Parallel EELS
PPM	Parts per million
RF	Radio frequency
RMS	Root mean square
RPM	Revolutions per minute
RXN	Reaction
SANS	Small angle neutrons scattering
SAXS	Small angle X-ray scattering
SQUID	Superconducting quantum interference device
SP	Slater–Pauling
SRO	Short range order
STEM	Scanning transmission electron microscopy
STM	Scanning tunneling microscopy
TEM	Transmission electron microscopy
TEP	Thermoelectric power
TMA	Thermomagnetic analysis
TMG	Thermomagnetic gravimetry
TTT	Time temperature transformation
VSM	Vibrating sample magnetometer
VBS	Virtual bound state
XRD	X-ray diffraction

1. Introduction and historical perspective

Over the past several decades, amorphous and more recently nanocrystalline materials have been investigated for applications in magnetic devices requiring magnetically soft materials such as transformers, inductive devices, etc. Most recently, research interest in nanocrystalline soft magnetic alloys has dramatically increased. This is due, in part, to the properties common to both amorphous and crystalline materials and the ability of these alloys to compete with their amorphous and crystalline counterparts. The benefits found in the nanocrystalline alloys stem from their chemical and structural variations on a nanoscale which are important for developing optimal magnetic properties.

This review is intended to summarize recent developments in the synthesis, structural characterization, properties and applications of nanocrystalline and amorphous magnets. The term 'nanocrystalline alloy' will be used for those alloys that have a majority of grain diameters in the typical range from ~1–50 nm. This term will include alloys made by rapid solidification, deposition techniques and solid state reactions where the initial material may be in the amorphous state and subsequently crystallized. We consider processing routes and methods to control chemistry and microstructural morphology on increasingly smaller length scales, and various developing experimental techniques which allow more accurate and quantitative probes of structure (including magnetic domain structure) on smaller length scales. We review the impact of microstructural control on the development of state of the art soft magnetic materials.

The demands on bulk soft magnetic materials include (1) higher combined induction and permeabilities and for some applications (2) magnets capable of operating at higher temperatures, as well as many non-magnetic issues such as mechanical properties, corrosion resistance, etc. In achieving such goals, key issues include alloy chemistry, structure and importantly the ability to tailor microstructural features. It is clear that the magnets used in soft magnetic applications must be optimized in terms of their intrinsic and extrinsic magnetic properties as well as their morphology. The key intrinsic magnetic properties, the saturation magnetic induction, B_S, and Curie temperatures, T_C, are determined by alloy composition and crystal structure.

Premiere high induction bulk materials include body centered cubic (BCC) Fe, Fe–Si, face centered cubic (FCC) α-Co and FeCo alloys (for reviews see for example Refs. [24,32]). FeCo bulk alloys [225,230] are particularly attractive because of their high inductions, but their permeabilities are smaller than those of amorphous and nanocrystalline alloys and Si steels. The extrinsic property of interest is the magnetic permeability, μ, the magnetic response function in an applied field, which usually is inversely related to the material's coercivity, H_c. The magnetic permeability, μ, is determined by chemistry, crystal structure, microstructure and morphology (shape). In particular, alloys with small magnetocrystalline anisotropies and magnetostrictive coefficients give rise to particularly soft magnetic materials.

Choice of soft magnetic materials for applications has been guided by recent

developments in the field of soft magnetic materials. Amorphous and nanocrystalline magnetic materials, in terms of combined induction and permeabilities are now competitive with SiFe bulk alloys, and the above mentioned Fe–Co alloys. In Fig. 1 (see Ref. [193]), figures of merit for Co-based amorphous alloys, Fe-based amorphous alloys, and nanocrystalline alloys are summarized. Co-based amorphous alloys, Fe-based amorphous alloys, and nanocrystalline alloys have evolved over the past decades with soft magnetic properties which now exceed those of the bulk alloys based on Fe, Co and Fe–Co.

Nanocrystalline alloys can be described in general as $TL_{1-x}(TE,M,NM)_x$ where TL denotes a late (ferromagnetic) transition metal element, TE is an early transition metal element, M is a metalloid, and NM is a noble metal. This composition usually has $x < 0.20$ i.e. with as much late ferromagnetic transition metals (TL of Co, Ni, or Fe) as possible. The remaining early transition metals (TE = Zr, Nb, Hf, Ta, etc.) and metalloids (M = B, P, Si, etc.) are added to promote glass formation in the precursor. The noble metal elements (TN = Cu, Ag, Au, etc.) serve as nucleating agents for the ferromagnetic nanocrystalline phase. The compositions are limited by where glass formation can occur prior to the nanocrystallization route. These alloys may be single phase (Type I) but are generally two phase materials with a nanocrystalline ferromagnetic phase and a

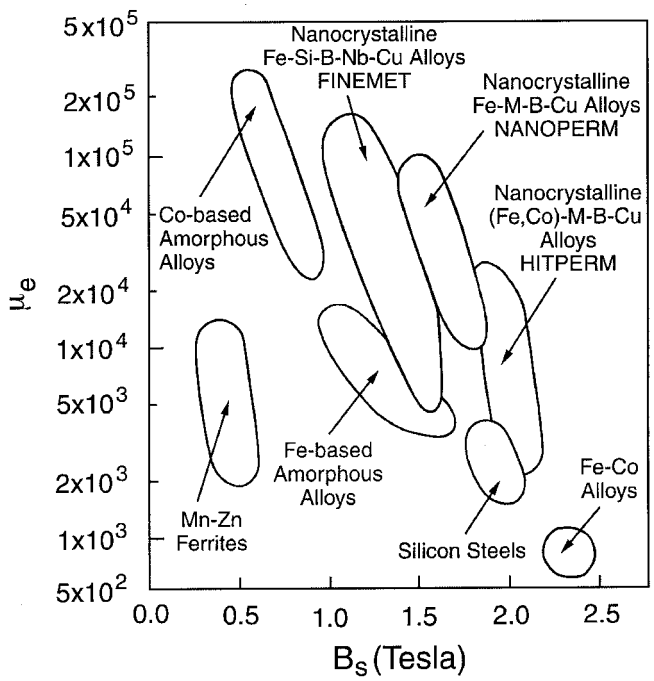

Fig. 1. Relationship between permeability, μ_e (at 1 kHz) and saturation polarization for soft magnetic materials (adapted from Ref. [193]).

residual amorphous phase at the grain boundaries (Type II). The Type II nanocryatalline alloys might have general properties (1) relatively high resistivity (50–80 μΩ cm) (2) low magnetocrystalline anisotropy (3) increased mechanical strength. With properties such as these, nanocrystalline alloys have great potential as soft magnetic materials.

Nanocrystalline Fe–Si–B–Nb–Cu alloys have been patented under the trade name FINEMET@^{TM}) [282,283]. Soft materials, based on Fe–M–B–Cu, have been patented by Kojima et al. [157] under the trade name NANOPERM@$^{®}$. These Fe–M–B–Cu (M = Zr, Nb, Hf,...) nanocrystalline alloys have all been optimized to achieve small magnetostrictive coefficients and concomitant large permeabilities. More recently (Fe,Co)–M–B–Cu (M = Nb, Hf, or Zr) nanocrystalline alloys, called HITPERM have been shown to have attractive inductions (1.6–2.1 T) combined with high permeabilities and high Curie temperatures. In FINEMETS α-FeSi nanoparticles with a DO_3 structure are observed, in NANOPERM α-Fe particles with a BCC structure are formed. In HITPERM alloys [134,276,277] nanocrystalline α-and α′ BCC and B2–FeSi (B2)-FeCo are formed with significantly improved high temperature magnetic properties than in the former two. HITPERM materials have been developed for applications with smaller permeability requirements but required large inductions at high temperatures.

NANOPERM (the original composition was Fe–Zr–B) was developed in Prof. Masumoto's laboratory at IMR Tohoku University in 1989. K. Suzuki joined the group at IMR to carry out a mechanical alloying project (development of bulk high-B materials from Fe-early-transition-metal nanocrystalline mechanically alloyed (MA) powders as originally proposed by A. Makino from ALPS Electric and Prof. A. Inoue. Contamination and oxidation effects in the MA process led Suzuki and Dr. Kataoka to the idea of using melt-spinning. They first expected to have a nanoscale α-Fe/ZrB material, but were pleased to discover that their Fe–Zr–B melt-spun amorphous alloy crystallized to two-phase α-Fe/amorphous materials similar to the microstructure previously observed in FINEMET [299]. HITPERM alloys were recently discovered by our group at CMU in 1997 while investigating materials for high temperature soft magnetic applications. This story is still unfolding, but we summarize some of the important and exciting initial results of studies of this material as part of this review.

1.1. Technical considerations

Magnetic hysteresis is a useful attribute of a permanent magnet material in which we wish to store a large metastable magnetization. On the other hand, a large class of applications requires small hysteresis losses per cycle. These include applications as inductors, low and high frequency transformers, alternating current machines, motors, generators and magnetic amplifiers. The desired technical properties of interest for soft magnetic materials include (see Fig. 2(a)):

1. *High permeability*: Permeability, $\mu = B/H = (1 + \chi)$, is the material's parameter

which describes the flux density, B, produced by a given applied field, H. In high permeability materials, we can produce very large changes in magnetic flux density in very small fields.

2. *Low hysteresis loss*: Hysteresis loss is the energy consumed in cycling a material between a field H and $-H$ and then back again. The energy consumed in one cycle is $W_h = \oint M\,dB$ or the area inside the hysteresis loop. The power loss of an AC device includes a term equal to the frequency multiplied by the hysteretic loss per cycle. Also of concern at high frequencies are eddy current losses that are intimately related to the material's resistivity, ρ.
3. *Large saturation and remnant magnetizations*: A large saturation magnetization, M_s, and induction, B_s, is desirable in applications of soft magnetic materials.
4. *High Curie temperature*: The ability to use soft magnetic materials at elevated temperatures is intimately dependent on the Curie temperature or magnetic ordering temperature of the material.

Conventional physical metallurgy approaches to improving soft ferromagnetic properties involve tailoring the chemistry and optimizing the microstructure. Significant in the optimizing of the microstructure is recognition of the fact that a measure of the magnetic hardness (the coercivity, H_c) is roughly inversely proportional to the grain size (D_g) for grain sizes exceeding ~0.1–1 μm (where the grain size exceeds the domain (Bloch) wall thickness, δ_W). In such cases grain boundaries act as impediments to domain wall motion, and thus fine-grained materials are usually magnetically harder than large grain materials. Significant recent developments in the understanding of magnetic coercivity mechanisms have lead to the realization that for very small grain sizes $D_g < \sim 100$ nm [99–

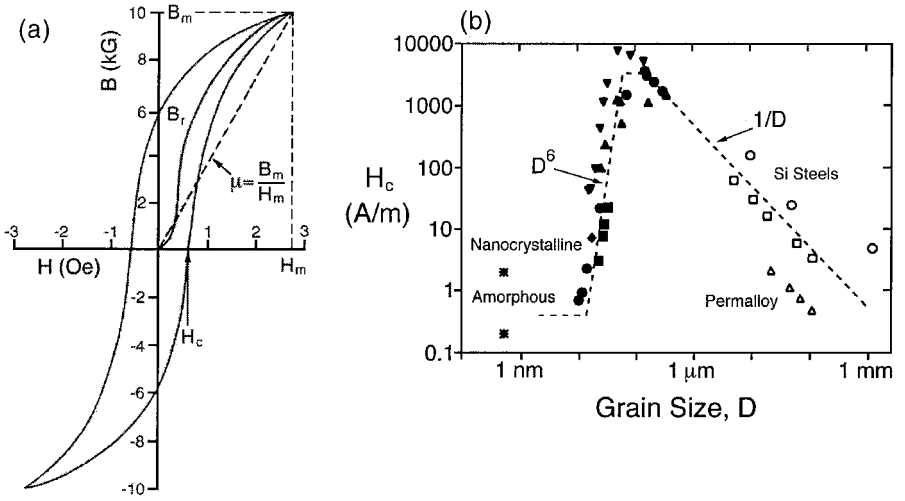

Fig. 2. Schematic of a hysteresis curve for a soft magnetic material defining some technical magnetic parameters [25] and (b) Herzer diagram [99,108] illustrating dependence of the coercivity, H_c, with grain size in magnetic alloys.

102,104,105] H_c decreases rapidly with decreasing grain size (see Fig. 2b). This can be understood by the fact that the domain wall, whose thickness, δ_W, exceeds the grain size, now samples several (or many) grains so that fluctuations in magnetic anisotropy on the grain size length scale are irrelevant to domain wall pinning. This important concept suggests that nanocrystalline and amorphous alloys have significant potential as soft magnetic materials. Soft magnetic properties require that nanocrystalline grains be exchange coupled and therefore any of the processing routes yielding free standing nanoparticles must include a compaction method in which the magnetic nanoparticles end up exchange coupled. Similar ideas have been stated for so called spring exchange hard magnetic materials [37,150, 244].

In this review, we will explore issues which are pertinent to the general understanding of the magnetic properties of amorphous and nanocrystalline materials. As the state of the art for amorphous magnetic materials is well developed and much of which has been thoroughly reviewed (see Refs. [92,93,183,219]), we will concentrate on highlights and recent developments. The development of nanocrystalline materials for soft magnetic applications is an emerging field for which we will try to offer a current perspective that may well evolve further with time.

The development of soft magnetic materials for applications requires attention to a variety of intrinsic magnetic properties (some of them ancillary) as well as development of extrinsic magnetic properties through an appropriate optimization of the microstructure. As intrinsic properties we take to mean microstructure insensitive properties. Among the fundamental intrinsic properties (which depend on alloy chemistry and crystal structure) the saturation magnetization, Curie temperature, magnetocrystalline anisotropy and the magnetostrictive coefficients are all important. In a broader sense, magnetic anisotropy and magnetostriction can be considered as extrinsic in that for a two-phase material (in aggregate) they depend on the microstructure. The desire for large magnetic inductions typically limits choices to alloys of Fe and Co (the elemental transition metal magnets with the largest atomic dipole moments). Curie temperatures are also largest for elemental Fe (770°C) and Co (1100°C), suggesting the use of Fe or Co (or Fe–Co) alloys especially in high temperature applications. It is these alloys which are discussed in most detail here. Magnetocrystalline anisotropy and magnetostriction which are determining factors in the ease in which the magnetization vector can be rotated into the direction of the applied field are also sensitively dependent on alloy chemistry. Many important soft magnetic alloy systems have zero crossings of the magnetocrystalline anisotropy, or magnetostriction coefficients which can be exploited in the development of premiere soft magnet materials.

A vast literature exists on the variation of intrinsic magnetic properties with alloy chemistry. Though new discoveries continue to be made in this area, it can be safely stated that a more wide open area in the development of magnetic materials for applications is the fundamental understanding and exploitation of microstructure's influence on the extrinsic magnetic properties. Important microstructural features include grain size, shape and orientation, defect

concentrations, compositional inhomogeneities, magnetic domains and domain walls. The interaction of magnetic domain walls with microstructural impediments to their motion is of particular importance to the understanding of soft magnetic properties. Extrinsic magnetic properties important in soft magnetic materials include the magnetic permeability and the coercivity, which typically have an inverse relationship. Remnant magnetization, squareness of the hysteresis loop and magnetic anisotropy (crystalline, shape or stress related) are also important in determining magnetic softness. Thorough discussions of soft magnetic materials are developed in texts such as in Refs. [28,32,35,43] and review articles as in Ref. [25].

This article is organized as follows. Section 1 gives introduction and historical perspective. Section 2 describes issues important to the design of soft magnetic alloys. This section introduces the topics: magnetic dipole moments and magnetization, ferromagnetic ordering (Curie) temperatures, magnetocrystalline anisotropy and magnetostriction, magnetic domains and magnetic domain wall mobility, AC magnetic response and considerations of glass forming ability. Section 3 discusses selected techniques used in the synthesis of amorphous and nanocrystalline magnetic materials. These include: powder synthesis of nanoparticles and nanoencapsulates (carbon arc synthesis, plasma torch synthesis, mechanical milling and powder consolidation), rapid solidification processing, solidification processing of bulk amorphous alloys and primary nanocrystallization of amorphous precursors. This is a selected and not exhaustive list of techniques that are finding or have the potential to find commercial relevance for producing materials. Section 4 describes thermodynamics, crystallization of amorphous materials, crystallization reactions, surface crystallization, kinetics of crystallization, and ordering and structural phase transitions in nanocrystalline materials. This includes summaries of experimental observations of the same. Section 5 discusses the structural observations of amorphous and nanocrystalline magnetic materials. These include X-ray scattering experiments; observation of microstructure and domain structure by transmission electron microscopy (TEM), high resolution TEM (HRTEM), Lorentz microscopy, optical microscopy and tunneling microscopy and spectroscopic observations by Mössbauer spectroscopy. Section 6 discusses models for magnetic dipole moments, magnetic valence, spin polarized energy bands, and random exchange. It also describes intrinsic (microstructure insensitive) magnetic properties including magnetic dipole moments, exchange interactions and Curie temperatures and observations in amorphous, bulk amorphous and nanocrystalline alloys. Exchange in disordered systems is discussed. Section 7 discusses models for random anisotropy, coupling in two-phase microstructures, induced anisotropies, etc. This includes much of the recent theoretical impetus behind the developments of nanocrystalline soft materials. Key issues connecting fundamental magnetic properties and microstructure are developed. Here we describe extrinsic (microstructure sensitive) magnetic properties including magnetic anisotropy, magnetostriction, induced magnetic anisotropy and magnetic coupling mediated through amorphous phases and observations in amorphous, bulk amorphous and nanocrystalline alloys.

Section 8 summarizes applications of amorphous and nanocrystalline soft magnetic materials putting the recent developments in a historical perspective and introducing some possible new applications for these materials. Section 9 summarizes conclusions.

2. Alloy design issues

Alloy design issues include issues of chemistry and processing designed to (1) optimize one of a number of important intrinsic and/or extrinsic magnetic properties as well as to (2) optimize structural or microstructural features which promote important (usually extrinsic) magnetic properties. The first of these issues concerns the choice of chemistry so as to impact the intrinsic magnetization of the material. The second issue pertinent to further discussions here are alloy additions designed at aiding formation of an amorphous or bulk amorphous phase, as a means to an end or as a precursor to producing a nanocrystalline material.

Alloy design issues are in many ways influenced by the processing routes used to achieve desired microstructures. Fig. 3 illustrates a flow chart for the considerations in designing and developing a nanocrystalline soft magnetic material from an amorphous precursor route as one example of the design process. Here, we consider first the effects of alloy composition on intrinsic magnetic properties. This is followed by a consideration of alloying additions necessary to produce an appropriate amorphous precursor. Typical experimental

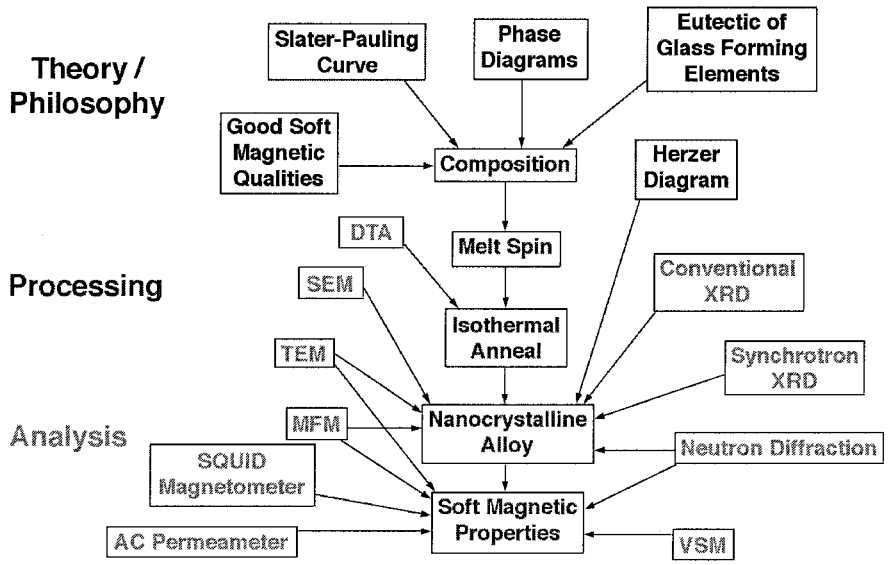

Fig. 3. Flow chart for the considerations in designing and developing a nanocrystalline soft magnetic material from an amorphous precursor route.

steps used to identify the structure and properties of the resulting materials are also illustrated. In the following we offer an introductory discussion of the issues in soft magnetic materials alloy design. Many of the issues introduced here will be discussed in further detail, in the context of recent developments in later sections.

2.1. Magnetic dipole moments and magnetization

The vast majority of soft magnetic materials have one or more of the ferromagnetic transition metal elements, Fe, Co or Ni, or the rare earth metal Gd as a majority component. The magnetic dipole moments of elemental and alloy magnets are most completely understood through the *band theory of solids* [170]. The band theory of solids considers the broadening of localized atomic states with discrete eigenvalues into a continuum of states for more itinerant electrons over a range of energies. The theory allows for calculation of energy dispersion (i.e. energy as a function of wave vector) and orbital angular momentum specific and spin-resolved densities of states. The calculation of spin-resolved energy bands and densities of states allows for the description of atom resolved magnetic dipole moments and, therefore, spontaneous magnetization of elemental and alloy magnetic solids. Among the successes of the band theory descriptions of magnetic properties are:

1. The prediction of non-integral or half integral atomic dipole moments and resulting ground state magnetizations in metals and alloys.
2. The prediction that band widths and *exchange splitting* (energy differences between spin up and spin down bands) are intimately dependent on magnetic coordination number and atomic volume.

Table 1 summarizes absolute zero and room temperature (where applicable) magnetizations and atomic dipole moments for some important transition metal and rare earth elemental magnets. Also shown are Curie temperatures (ferromagnetic ordering temperatures, discussed in Section 2.2.) which are not ground state properties that are directly calculable from band theory.

State of the art band structure techniques use the so-called one electron and

Table 1
Spontaneous and room temperature magnetizations, magnetic dipole moments, and Curie temperature for elemental ferromagnets

Element	μ_m @ 0 K(μ_B)	M_s @ 0 K	M_s @ RT	T_C (K)
		(G)	(G)	
Fe	2.22	1740	1707	1043
Co	1.72	1446	1400	1388
Ni	0.606	510	485	627
Gd	7.63	2060	–	292
Dy	10.2	2920	–	88

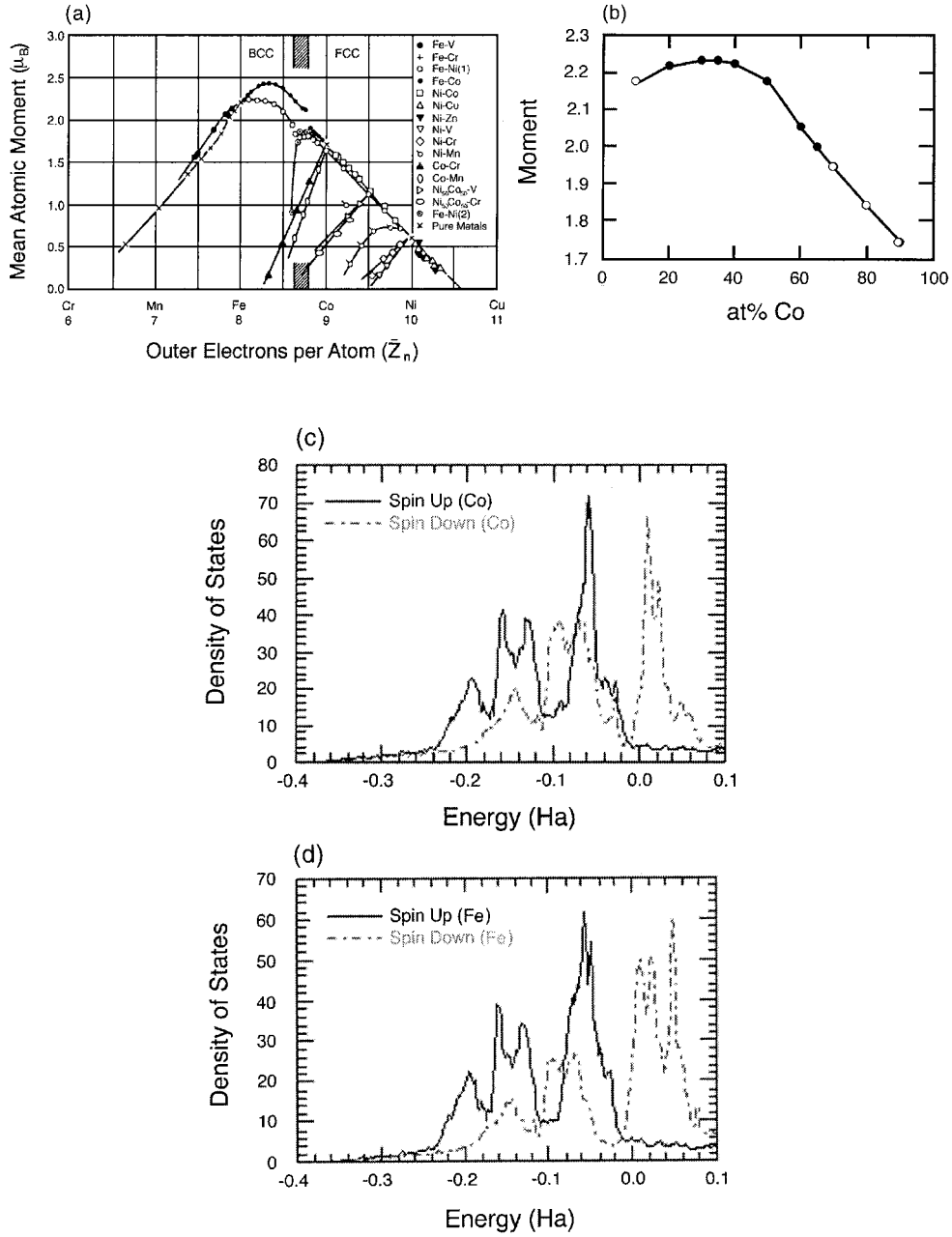

Fig. 4. (a) Slater–Pauling curve for TM alloys (after Bozorth); (b) Spin-only Slater–Pauling curve for the ordered Fe–Co alloy as determined from LKKR band structure calculations; Density of states for Co (c) and Fe (d) in the ordered equiatomic alloy [184]. The Fermi level is taken as the zero of energy.

local density approximations (for example the LKKR technique [185] whose results are consider in Table 1). These treat the electronic potential more accurately, but still not at the level of consideration of all individual electron–electron interactions. These result, for example, in densities of states with more structure than in the simple free electron model and in more accurate description of the magnetic states in solids. A detailed discussion of band structure techniques is beyond the scope of this article. However, we do wish to illustrate some example of the results of band theory in describing alloying effects on magnetic dipole moments in solids.

Fig. 4(a) shows the Slater–Pauling curve that illustrates the variation of the mean atomic magnetic dipole moment as a function of composition in transition metal alloy systems. Fig. 4(c) and (d) shows spin resolved densities of states $g_+(E)$ and $g_-(E)$ for Co and Fe atoms, in an equiatomic FeCo alloy, as a function of energy (where the Fermi energy, E_F, is taken as the zero of energy). The number of spin up, n_+ and spin down, n_- electrons in each band can again be calculated by integrating these densities of state:

$$n_+ = \int_0^{E_F^+} g_+(E)\,dE \quad \text{and} \quad n_- = \int_0^{E_F^-} g_-(E)\,dE \tag{1}$$

(here the Fermi energies, E_F, are the same and the zero's of energy are different for the two spin bands) and the atom resolved (i.e. Fe on Co) magnetic dipole moments can be calculated as:

$$\mu_m = (n_+ - n_-)\mu_B \tag{2}$$

Knowledge of atomic volumes or alloy density, then allows for the direct calculation of the alloy magnetization. Fig. 4(b) shows the band theory prediction of the average (spin only) dipole moment in a $Fe_{1-x}Co_x$ alloys as a function of composition to be in good quantitative agreement with the experimentally derived Slater–Pauling curve.

For magnetic alloy design the Slater–Pauling curve is an important starting point. The desire for large induction limits choices of alloys to those rich in Fe or Co and therefore near the top of the Slater–Pauling curve. As described in the Slater–Pauling curve Fe–Co alloys exhibit the largest magnetic inductions of any material, and also have Curie temperatures which are desirable for high temperature applications. Alloys near the equiatomic composition are particularly soft and exhibit large permeabilities, but this magnetic softness is rooted in small values of the first-order magnetic anisotropy constant, K_1, which will be discussed further in Section 2.3. Fe-rich alloys typically have smaller inductions and lower Curie temperatures than Fe–Co alloys. Fe–Si is another premiere crystalline soft material whose significant application includes transformer laminate. Co alloys can also be soft but only if the FCC phase of Co is present. Co-rich alloys typically have smaller inductions and larger T_C's.

2.2. Ferromagnetic ordering (Curie) temperatures

Ferromagnetism is a collective phenomenon since individual atomic moments interact so as to promote alignment with one another. This collective interaction gives rise to the temperature dependence of the magnetization. Two models have explained the interaction between atomic moments. Mean Field Theory considers the existence of a non-local internal magnetic field, called the Weiss field, which acts to align magnetic dipole moments even in the absence of an applied field H_a. Heisenberg Exchange Theory considers a local (usually nearest neighbor) interaction between atomic moments (spins) which acts to align adjacent moments even in the absence of a field.

The basic assumption of the mean field theory is that this internal field is non-local and is directly proportional to the sample magnetization, $H_{INT} = \lambda_W \mathbf{M}$, where the constant of proportionality, λ_W, is called the Weiss molecular field constant. To consider ferromagnetic response in applied field, $\mathbf{H}_a$, as well as the randomizing effects of temperature, we consider the superposition of the applied and internal magnetic fields. By analogy with the problem of paramagnetic moments, the average atomic dipole moment can be expressed in terms of the Brillouin function $< \mu_m >= \mu_m^{atom} B_J(a')$, where $a' = (\mu_0 \mu_m^{atom}/k_B T)(H + \lambda_W M)$ for a collection of classical dipole moments. Similarly, the saturation magnetization, $M_s = N_m < \mu_m^{atom} >$ and:

$$\frac{M}{N_m \mu_m^{atom}} = \frac{M}{M_s} = B_J\{H + \lambda_W M\} \tag{3}$$

Under appropriate conditions, this leads to solutions for which there is a non-zero magnetization (spontaneous magnetization) even in the absence of an applied field. For $T > T_{C'}$ the ferromagnetic Curie temperature the only solution to Eq. (3) is $M = 0$, i.e., no spontaneous magnetization and thus paramagnetic response. For $T < T_C$, we obtain solutions with a non-zero, spontaneous, magnetization, the defining feature of a ferromagnet.

The Heisenberg model considers ferromagnetism and the defining spontaneous magnetization to result from nearest neighbor exchange interactions, which act to align spins in a parallel configuration, instead of a non-local, mean field. The Heisenberg model can be further generalized to account for atomic moments of different magnitude and signs, i.e., in alloys, and for exchange interactions, which act to align nearest neighbor moments in an anti-parallel fashion, or in a non-collinear relationship. Let us consider first the Heisenberg ferromagnet. Here we assume that the atomic moments (due to a spin vector $\mathbf{S}$) on nearest neighbor sites are coupled by a nearest neighbor exchange interaction that gives rise to a potential energy:

$$E_p = -J_{ex} \mathbf{S}_i \times \mathbf{S}_{i+1} \tag{4}$$

that for $J_{ex} > 0$ favors parallel alignment of the spins. The exchange energy, suitably scaled, replaces the Weiss molecular field constant in the mean field

theory of ferromagnetism to explain the temperature dependence of the magnetization.

Ferromagnetic exchange interactions set the scale for Curie temperatures in ferromagnetic alloys. Interatomic exchange couplings can be calculated from first principles by considering the energy change associated with rotation of individual spins in the host material. These exchange interactions can be used within a mean field theory to estimate the Curie temperature. An empirical description of the variations of the exchange energy with interatomic spacing called the Bethe–Slater curve is instructive in describing the effect of alloying on ferromagnetic Curie temperatures. In 3*d* transition metal solids, the Bethe–Slater curve, shown in Fig. 5 predicts the sign of the exchange interaction. The interplay between electron–electron Coulomb interactions and the constraints of the Pauli exclusion principle determine the sign of the exchange interaction. In transition metal solids a measure of the overlap between nearest neighbor d-orbitals is given by the ratio of the atomic to the 3*d* ionic (or nearest neighbor) radius. In mean field theory the Curie temperature can be related to the exchange energy as follows:

$$T_C = \frac{2ZJ_{ex}S(S+1)}{3k_B} \tag{5}$$

where Z is the nearest neighbor coordination number and S is the total spin angular momentum.

Alloying effects and the effects of disorder can be qualitatively understood by appealing to Eq. (4) and the Bethe–Slater curve (Fig. 5). From the shape of the Bethe–Slater curve and the relative positions of Fe and Co on the curve it can be inferred, for example, that $M(T)$ in Co-based alloys will be relatively invariant to disorder as compared with Fe-based alloys [61]. In the amorphous phase, structural fluctuations give rise to fluctuations in the exchange interactions. These, in turn, cause a depression of the reduced magnetization versus reduced

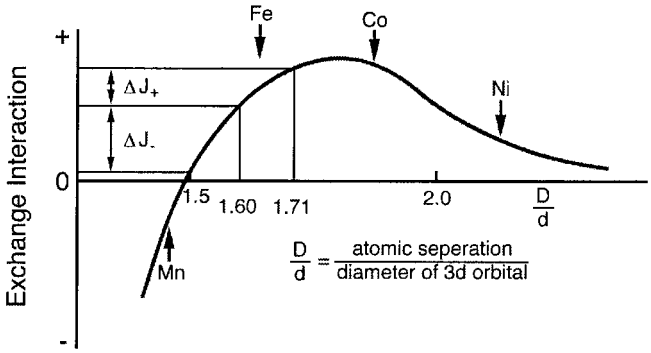

Fig. 5. Bethe–Slater curve for the magnetic exchange interaction energy as a function of interatomic spacing (normalized by the spatial extent of the magnetic 3d orbitals). Also showing large variations of J with position on the left of the curve (see Ref. [32]).

temperature curve as illustrated above. A first order theory as to the fluctuation in the exchange interactions with fluctuations in interatomic spacing can be offered by considering a Taylor series expansion of the exchange interaction as a function of nearest neighbor spacing of the form:

$$J_{ex} = J^0_{ex} + \left(\frac{\partial J_{ex}}{\partial X}\right)_{x_0} \Delta X + \cdots \tag{6}$$

It can be readily seen that alloys which have exchange energies, J^0_{ex}, which lie near the peak in the Bethe–Slater curve (see Fig. 6(b)) (e.g., Co, FeCo) will be relatively insensitive to fluctuations in the interatomic separation since $dJ/dx \sim 0$. On the other hand, alloys for which J^0_{ex} lies well away from the peak (e.g. Fe- and Ni- based alloys for which $dJ/dx \neq 0$) will have J_{ex} be more sensitive to fluctuations in the interatomic separation (see Fig. 6(a)). It should be noted that alloy additions which reduce the magnetic coordination numbers for Fe and Co should shift J^0_{ex} to the left of the elemental values.

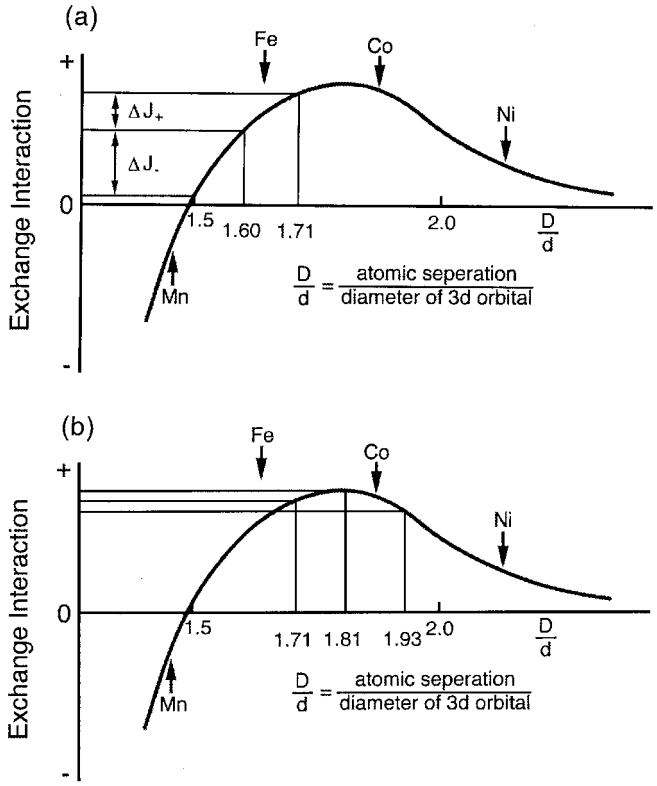

Fig. 6. Bethe–Slater curves for (a) Fe-rich and (b) Co-rich amorphous alloys, respectively showing fluctuations in interatomic distances and resulting fluctuations in the exchange interactions [61].

2.3. Magnetocrystalline anisotropy and magnetostriction

The magnetization curve (Fig. 2(a)) illustrates the technical magnetic properties of a ferromagnetic material. Its shape is determined by minimizing the material's magnetic free energy. The magnetic free energy consists of terms associated with the field energy (Zeeman energy), self-field (demagnetization energy), wall energy, and magnetic anisotropy energy. The magnetic Helmholtz free energy [37] can be determined by integrating a magnetic energy density as follows:

$$F_M = \int \left[A(\mathbf{r}) \left[\frac{\nabla \mathbf{M}}{\mathbf{M}_s} \right]^2 - K_l(\mathbf{r}) \left[\frac{\mathbf{M} \times \mathbf{n}}{\mathbf{M}_s} \right]^2 - \mu_0 \mathbf{M} \times \mathbf{H} \right] d\mathbf{r} \tag{7}$$

where $A(\mathbf{r})$ is the local exchange stiffness ($A = CJS^2/a$ at 0 K, with $C \sim 1$ depending on crystal structure and a is the interatomic spacing), $K_1(\mathbf{r})$ is the (leading term) local magnetic anisotropy energy density, $\mathbf{M}$ is the magnetization vector, $\mathbf{n}$ is a unit vector parallel to the easy direction of magnetization and $\mathbf{H}$ is the sum of the applied field and demagnetization field vectors. The magnetic anisotropy energy describes the angular dependence of the magnetic energy, i.e. its dependence on angles θ and ϕ between the magnetization and an easy axis of magnetization [37,244]. The anisotropy energy can be further subdivided into magnetocrystalline, shape and stress anisotropies, etc.

Since the magnetic anisotropy represents a barrier to switching the magnetization for soft magnetic materials, a small magnetic anisotropy is desired so as to minimize the hysteretic losses and maximize the permeability. The desire for small magnetocrystalline anisotropy necessitates the choice of cubic crystalline phases of Fe, Co, Ni or alloys such as FeCo, FeNi, etc. (with small values of K_1). In crystalline alloys, such as permalloy or FeCo, the alloy chemistry is varied so that the first order magnetocrystalline anisotropy energy density, K_1, is minimized. Similarly, stress anisotropy is reduced in alloys with nearly zero magnetostriction. Shape anisotropy results from demagnetization effects and is minimized by producing materials with magnetic grains with large aspects ratios. Amorphous alloys are a special class of soft materials where (in some notable cases) low magnetic anisotropies result from the lack of crystalline periodicity.

Magnetostriction is the process by which the shape of a ferromagnetic materials changes in the process of magnetization as a result of magnetoelastic interactions. It is included as a magnetic anisotropy effect because of its angular dependence, but in reality it represents a higher order effect in that it involves the coupling of the magnetic anisotropy and elastic properties of the material. Magnetostriction results in the ferromagnetic material being strained during the process of magnetization. The average strain dl/l for a typical transition metal ferromagnet is in the order of 10^{-5}–10^{-6}. Magnetostriction is a deleterious property for soft magnetic applications (i.e. it is the source of loss in transformers which is accompanied by transformer hum). The strain in a magnetostrictive material increases with increasing field until such point that it saturates having a value, λ_s.

The physical origin of magnetostrictive response lies in spin-orbit interactions as

is also the case for magnetocrystalline anisotropy. Where magnetocrystalline anisotropy results from coupling of the magnetization and easy crystalline axes, the magnetostrictive component involves magnetoelastic coupling and the dilation or expansion of the lattice as a consequence of rotation of the magnetization in the magnetization process. Magnetostrictive coefficients are also dependent on chemical composition and can be optimized (subject to other constraints) by varying the chemistry [110].

As an example of the dependence of magnetic anisotropy and magnetostriction (as well as magnetization) on alloy chemistry, Fig. 7 illustrates the variation of saturation induction, Curie temperature, magnetocrystalline anisotropy, K_1, and magnetostriction, λ, in FeCo alloys. In choosing a binary alloy composition in the binary $Fe_{1-x}Co_x$ system it is important to consider the maximum induction which occurs near $x = 0.3$, the minimum magnetocrystalline anisotropy which occurs near $x = 0.5$, and finally compositions which minimize magnetostrictive

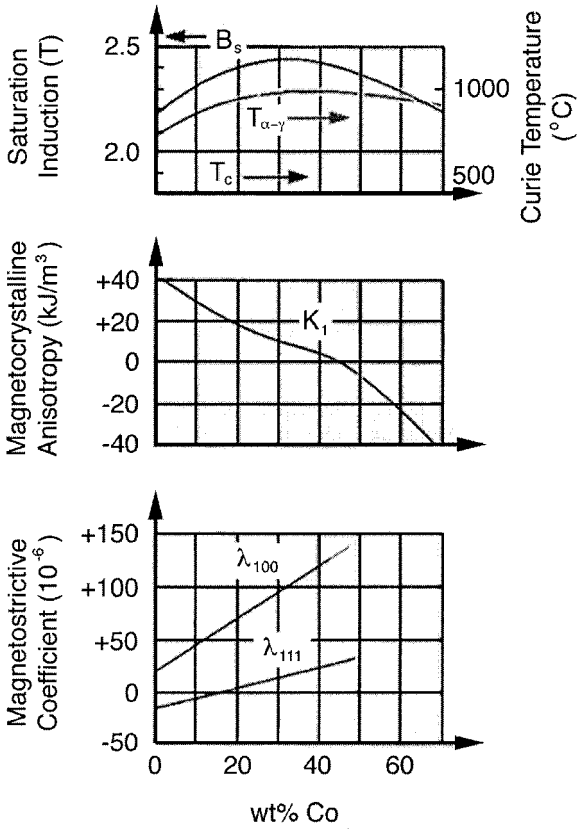

Fig. 7. (a) Saturation magnetization and Curie temperature, (b) magnetocrystalline anisotropy, K_1 and magnetostriction. λ, in the FeCo system (reproduced from Pfiefer and Radeloff [225]).

coefficients. In the FeCo alloys magnetostriction coefficients, λ_{111} and λ_{100} are both substantial near the equiatomic composition where the magnetocrystalline anisotropy vanishes. Across this alloy system, Curie temperatures are large enough to cause no problems in high temperature magnetization (i.e. 500°C). These considerations have been coupled with consideration of alloy resistivity (important for determining eddy current losses) and alloy additions which influence mechanical properties to design an alloy for rotor applications in electric aircraft engines. Magnetostriction considerations are also known to be quite important in the design of soft magnetic materials for inductive devices, transformers and a host of other applications.

2.4. Magnetic domains and domain wall mobility

In a ferromagnet there are macroscopic volumes, called magnetic domains, over which atomic magnetic moments are aligned due to the internal (Weiss) field or alternatively the ferromagnetic exchange interaction. In a typical magnetic material a macroscopic volume of the material contains many domains. Each of these domains has a spontaneous magnetization of magnitude, M_s. In the absence of an aligning field the magnetization vectors are aligned differently from domain to domain. Thus if we take the vector average of the magnetization over many domains we arrive at zero sample magnetization, $\langle M \rangle = 0$, because of vector cancellation of the random domain moments. The magnetization process involves the growth of domains that are favorably oriented with the applied magnetic field at the expense of those that are not.

Having more than one domain requires an interfacial region between domains called a domain wall. Associated with this interface is a positive domain wall energy. The ultimate number and size, of magnetic domains in a sample is determined by a balance between the volume, magnetostatic, and interfacial domain wall energies. In soft materials, which have been optimized to have very low rotational energy barriers, the major determinant of the shape of the magnetization curve is domain wall motion.

In future discussions, we will find it useful to describe several length scales that are associated with domains and domain walls. These are expressed through consideration of domain wall energetics. The energy per unit area in the wall can be expressed as a sum of exchange and anisotropy energy terms:

$$\gamma_{\text{Wall}} = \gamma_{\text{exc}} + \gamma_K \tag{8}$$

where the anisotropy energy per unit volume, K, is multiplied by volume contained in a domain wall, $A_W \delta_W$, and divided by cross-sectional area to arrive at an anisotropy energy per unit area:

$$\gamma_K = K\left(\frac{A_W \delta_W}{A_W}\right) = K\delta_W = K(Na) \tag{9}$$

where $\delta_W = N_p a$ (a is the lattice constant in the direction of rotation and N is the

number of planes over which the rotation takes place) is the thickness of the wall. Thus γ_{wall} can be expressed:

$$\gamma_{\text{wall}} = \frac{\pi^2 J_{\text{ex}} S^2}{Na^2} + K_1(N_p a) \tag{10}$$

where the first term considers the cost in exchange energy in rotating magnetic dipole moments in a 180° domain wall as illustrated in Fig. 8. To determine the optimal wall thickness we differentiate γ_{W} with respect to δ_{W}:

$$\frac{1}{a}\frac{\partial \gamma_{\text{wall}}}{\partial N_p} = 0 = -\frac{\pi^2 J_{\text{ex}} S^2}{N_p^2 a^2} + K_1 \tag{11}$$

yielding:

$$N_{\text{eq}} = \sqrt{\frac{\pi^2 J_{\text{ex}} S^2}{K_1 a^3}} \tag{12}$$

For Fe, $N_{\text{eq}} \sim 300$ and the equilibrium thickness, $t_{\text{eq}} = N_{\text{eq}} a \sim 50$ nm. Expressed in terms of the exchange stiffness, A_{ex}, the domain wall width, δ_{W} is:

$$\delta_{\text{W}} = \pi\sqrt{\frac{A_{\text{ex}}}{K_1}} \tag{13}$$

Another important length scale is the distance over which the perturbation due to the switching of a single spin decays in a soft material. This length is called the ferromagnetic exchange length, L_{ex}, and can be expressed:

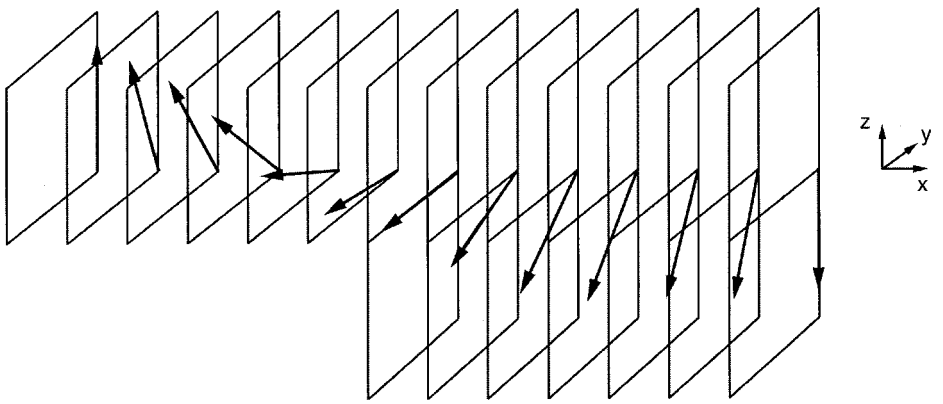

Fig. 8. Rotation of atomic magnetic dipole moments in a 180° (Bloch) domain wall in a ferromagnetic material.

$$L_{ex} = \sqrt{\frac{A_{ex}}{\mu_0 M_s^2}} \tag{14}$$

The ferromagnetic exchange length is ~3 nm. for ferromagnetic iron- or cobalt-based alloys. The ratio of the exchange length to δ_W/π is a dimensionless parameter, κ, called the magnetic hardness parameter:

$$\kappa = \frac{\pi L_{ex}}{\delta_W} = \sqrt{\frac{K_1}{\mu_0 M_s^2}} \tag{15}$$

For hard magnetic materials κ is in the order of unity and thus there is little difference between the ferromagnetic exchange length and the domain wall width. On the other hand, for good soft magnetic materials, where K_1 approaches zero, can deviate substantially from unity.

Structure sensitive magnetic properties may depend on defect concentration (point, line and planar defects), atomic order, impurities, second phases, thermal history, etc. In multi-domain materials, the domain wall energy density, $\gamma = 4(AK_1)^{1/2} = \gamma(x)$, is spatially varying as a result of local variations in properties due to chemical variation, defects, etc. A domain wall will prefer to locate itself in regions where the magnetic order parameter is suppressed, i. e. pinning sites. Since changes in induction in high-permeability materials occur by domain wall motion, it is desirable to limit variation of $\gamma(x)$ (pinning). This is one of the key design issues in developing soft magnetic materials, i.e. that of process control of the microstructure so as to optimize the soft magnetic properties.

2.5. AC magnetic response

Soft magnetic material's magnetic loss mechanisms include: (1) hysteresis loss due to irreversible domain wall motion and rotational out of easy axes loss mechanism, (2) eddy current losses and (3) anomalous losses. The energy loss per cycle is given by $\oint B\,dH$ and for linear response the power loss is $f \times B^2/2\mu$, where f is the frequency. In real materials (which are nonlinear) we express the hysteresis power loss as:

$$P_h \sim C_h f B_{max}^n \tag{16}$$

where C_h may vary with the material, and a typical exponent n is ~ 1.6. Eddy current loss results from the fact that $d\phi/dt$ induces voltages in the core material with consequent V^2/R power loss appearing as heat. This power loss can be reduced by decreasing V and increasing R. Since $V \sim f B_{max}$ then the power loss due to eddy currents is proportional to $f^2 B_{max}^2$, i.e.:

$$P_e = C_e f^2 B_{max}^2 \tag{17}$$

To reduce the eddy current loss in sheet transformers, they are often laminated so as to reduce the length scale of eddy current loops. In designing transformers the

total power loss:

$$P_{TOT} = P_h + P_e = C_h f B_{max}^n + C_e f^2 B_{max}^2 \quad (18)$$

must be minimized.

The important physical parameters which can be altered to minimize alternating current (AC) losses are those influencing the hysteresis loss as described above and those which influence the eddy current losses. By and large the most important physical parameter which influence the eddy current losses and therefore the high frequency losses is the electrical resistivity, ρ. Large electrical resistivities are essential for reducing AC losses. Electrical resistivities in amorphous alloys can be several hundred $\mu\Omega$ cm and for nanocrystalline alloys $\sim$50 $\mu\Omega$ cm, which in both cases offer significant advantage over crystalline metallic magnetic materials ($\sim$1–10 $\mu\Omega$ cm).

2.6. Considerations of glass forming ability and crystallization

The considerations for synthesizing amorphous metallic alloys are often at odds with the considerations for optimizing magnetic properties. This is because the addition of typical glass forming agents has a deleterious effect on such intrinsic magnetic properties as the saturation induction and the Curie temperature. Considerations for glass forming ability in binary systems include the temperature and composition of the eutectic, the terminal phases to the right and left of the eutectic composition, the slope of the liquidus as a function of composition, etc. If the amorphous alloy is to be used as a precursor for the production of a nanocrystalline material the primary and secondary crystallization temperatures are of importance as is the structure of the ferromagnetic nanocrystalline phase that is the product of primary crystallization. Table 2 summarizes these parameters for selected binary Co- and Fe- with early transition metals (TE) and metalloids (M).

The alloy chemistry considerations for synthesizing amorphous metallic alloys, bulk amorphous alloys and amorphous precursors for nanocrystallization routes can all be different and will be discussed in more detail in Section 3. Some general observations can be made, however, which offer useful insights in magnetic alloy design. First, alloying additions with non-magnetic species will reduce average magnetic dipole moments at the least by dilution and more if the solute potential is strongly perturbing or if strong chemical bonding between the magnetic transition metal and second component occurs (as is the case in TL–M systems). It is, therefore, desirable to have the eutectic composition as close to pure TL as possible, so as to keep the magnetization high.

Typical phase diagrams for a TL–TE (Fe–Zr) and TL–M (Fe–B) are illustrated in Fig. 9. TL–TE systems typically have much lower eutectic compositions than TL–M. In typical metallic glasses the TL–M eutectic occurs near 20 at% M and inductions exceeding $\sim$1.3 T are generally not possible. In synthesizing bulk amorphous materials the considerations are different and the so-called 'confusion

Table 2
Considerations for select glass forming ability in binary systems: temperature and composition of the eutectic, the slope of the liquidus, and the terminal phases to the right and left of the eutectic composition [197]

Binary alloy	x_E at% (wt%)	T_E(°C)	dT_L/dx	Terminal phases	
Fe–B	17 (3.8)	1174	21.4	Fe	Fe_2B
Co–B	18.5 (4)	1110	20.8	Co	$Co_2B(Co_3B)$
Fe–Si	33 (20)	1212	~ 10	Fe	$Fe_2Si(Fe_3Si)$
Co–Si	23.5 (12.8)	1200	~ 13	Co	$Co_2Si(Co_3Si)$
Fe–Sc	9 (7.4)	1200	~ 40	Fe	Fe_2Sc
Co–Sc	13.7(10.8)	1140	~ 26.3	Co	Co_2Sc
Fe–Zr	10 (15)	1337	20	Fe	$Fe_2Zr(Fe_3Zr)$
Co–Zr	9.5 (14.33)	1232	27.7	Co	γ
Fe–Hf	8.5 (22)	1390	18	Co	λ
Co–Hf	11 (22.9)	1230	24	Co	Co_7Hf,Co_7Hf_2, $Co_{23}Hf_6$
Fe–Nb	12 (18.5)	1373	~ 14	Fe	ε
Co–Nb	14 (22.5)	1247	~ 18	Co	Co_3B,α/β Co_2B
Fe–Ta	7.9 (21)	1442	12.5	Fe	ε
Co–Ta	13.5 (32.5)	1276	~ 22	Co	Co_2Ta
Fe–Y	8.25 (12.5)	1350	~ 23	Fe	$Fe_{17}Y_2$
Co–Y	7.5 (11)	1340	~ 21	Co	$Co_{17}Y_2$
Fe–La	9 (19.5)	1460	~ 9	Fe	$Fe_{13}La$(?)
Co–La	69 (84)	500	~ 14.5	Co	$Co_{13}La$

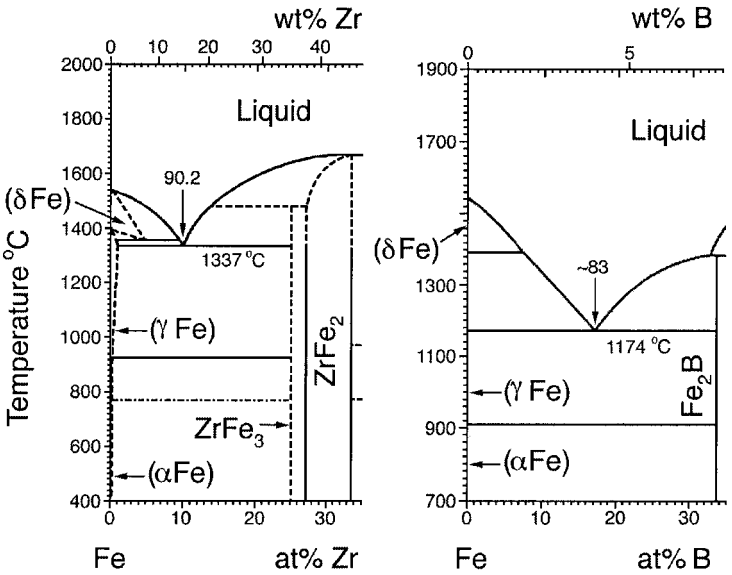

Fig. 9. Equilibrium phase diagrams, showing eutectics for two prototypical alloy systems for which amorphous alloys are readily produced, the Fe–Zr and Fe–B systems [197].

principle' suggest having a multicomponent system and TM contents of ~70 at% or less are common with consequently lower inductions. Three empirical rules for synthesis of bulk amorphous alloys with large glass forming abilities have been proposed by Inoue [127]. These are (1) multicomponent systems with three or more constituent elements, (2) significantly different atomic size ratios typically with difference exceeding ~13% and (3) negative heats of mixing among constituents. A second observation is that the TL–M and TL–M systems described above the primary crystallization is typically of the magnetic transition metal and occurs at temperatures of approximately 500°C, but can vary for different compositions. The primary crystallization temperature, T_{x1}, (or a fraction thereof) represents the upper limit of use for an amorphous material. For synthesis of a nanocrystalline material this is the useful crystallization event. In the amorphous precursor route to producing nanocrystalline materials secondary crystallization is typically of a terminal TL–TE and/or TL–M phase. This phase is typically deleterious in that it lowers magnetic permeability by domain wall pinning. The secondary crystallization temperature, T_{x2}, represents the upper limit of use for nanocrystalline materials.

Fig. 10 illustrates a differential thermal analysis (DTA) plot of heat evolved as a function of temperature for a $Fe_{44}Co_{44}Zr_7B_4Cu_1$ (HITPERM) alloy. This figure shows two distinct crystallization events as exothermic peaks in the DTA data. These are labeled T_{x1} at 510°C and T_{x2} at 700°C. These peaks correspond to the crystallization of α′-FeCo and $(Fe, Co)_3Zr$, respectively. At temperatures higher than T_{x2}, the instability of the intergranular amorphous phase may allow for the formation of additional precipitates, such as refractory borides. In interesting TM–TE systems, the primary crystallization event yields nanocrystals of a soft magnetic phase (α-Fe, α-Co, α-Fe–Si or α- or α′-FeCo) surrounded by a more

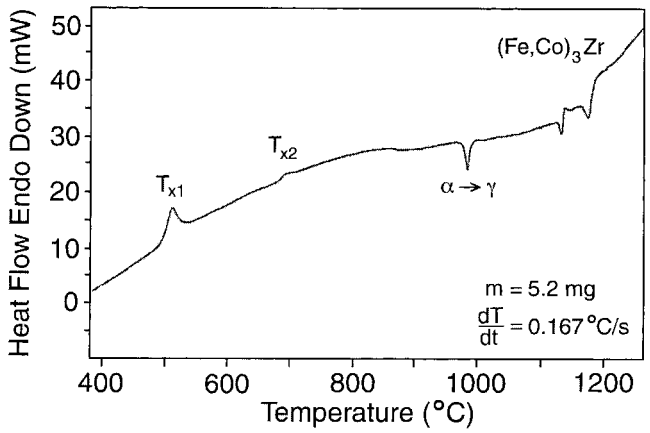

Fig. 10. Differential thermal analysis (DTA) plot of heat evolved as a function of temperature for a $Fe_{44}Co_{44}Zr_7B_4Cu_1$ alloy showing two distinct crystallization events [276,277].

stable intergranular amorphous phase. The composition of this intergranular amorphous phase is also important in determining its ultimate stability and its magnetic properties as will be discussed further in subsequent sections.

Further alloy considerations in the amorphous precursor route are the additions of other components (e.g. Cu) which come out of solution early and provide many nucleation sites for the primary crystallization events [10,118]. The addition of small amounts of Cu to alloys is also commonly thought to depress T_x. Of course, the above mentioned considerations based on the influence of alloy composition and its effects on intrinsic and extrinsic magnetic properties must be considered along with the considerations of microstructural control to optimize the magnetic properties of the final material.

3. Synthesis of nanoparticles, amorphous, bulk amorphous and nanocrystalline alloys

The synthesis of amorphous and nanocrystalline alloys requires consideration of the alloy design issues as discussed in the previous section. However, judicious choice of the processing method is necessary to produce alloys in the amorphous state. Circumventing the crystallization process is also necessary for alloy formation in the amorphous state, either as an end product or as precursor to nanocrystallization. The kinetics of crystallization will be discussed in the next section. In this section, synthesis routes that have proven successful for producing amorphous and nanocrystalline alloys will be discussed.

We will limit our discussion to the following four synthesis routes (though others certainly exist) which are viable for producing alloys for larger scale applications, as opposed to thin film synthesis for microelectronic applications, for example. These synthesis routes are:

1. *Powder synthesis techniques*: Magnetic nanocrystals may be synthesized as free standing powders or nanoencapsulates which must then be compacted to form a bulk alloy with nanocrystalline grains. Examples of these techniques include Carbon-arc synthesis, plasma torch synthesis and gas atomization techniques, among others. We discuss selected powder synthesis techniques that include C-arc synthesis, plasma torch synthesis and mechanical milling techniques.
2. *Rapid solidification processing*: Amorphous alloys can be produced by a variety of rapid solidification processing routes. These typically require cooling rates of $> 10^4$ K/s for typical alloys at a eutectic composition. Examples of these techniques include splat quenching, melt spinning, etc. Slower cooling rate are possible for bulk amorphous alloys as described next.
3. *Solidification processing of bulk amorphous alloys*: Bulk amorphous alloys are formed by more conventional solidification routes with slower cooling rates. The so-called large glass forming abilities of these alloys allows for production of amorphous materials with much larger dimensions, thus the name bulk amorphous alloys.
4. *Crystallization of amorphous precursors*: Bulk alloys with nanocrystalline grains

can also be produced by solid state reaction (crystallization) of an amorphous precursor.

3.1. Powder synthesis of nanoparticles and nanoencapsulates

Nanometer-sized atomic clusters have demonstrated remarkable magnetic properties that differ both from the properties of the individual atoms and from the properties of bulk crystalline solids. Nanoencapsulated materials refer to such particles which are passivated by encapsulation with a protective chemically distinct coating. The utility of nanoencapsulated materials depends on the ability to tailor magnetic properties by controlling the size distribution, morphology, and chemical composition on a nanoscale. A variety of synthesis techniques have been used to produce nanoparticles at the research level including gas condensation, mechanical attrition, chemical or physical vapor deposition, chemical precipitation, aerosol reactions, atomization, biological templating, electrodeposition, and rapid solidification. Synthesis routes capable of scaling to industrial production levels and accomplishing nanoencapsulation include C-arc and plasma technology and mechanical milling techniques that will be discussed below. The former are two techniques which have been employed by the Carnegie Mellon University group in the synthesis of magnetic nanoparticles and encapsulated magnetic nanoparticles which are discussed as examples of current processing routes for the production of magnetic nanoparticles and nanoencapsulates. The latter has been used commonly as a synthesis route for nanoparticles.

3.1.1. Carbon arc synthesis

The Krätschmer–Huffman carbon arc process [171] has been a primary method employed to synthesize nanoencapsulates, nanotubes and endohedral fullerenes [18]. Carbon electrodes, with metal or metal oxide, graphite, and an organic binder have been commonly employed. The technique allows for production of metal or metal carbide nanoparticles with protective carbon coatings. An example of a C-arc reactor is illustrated in Fig. 11. A water-cooled bath reactor is shown that has been employed by the group at Carnegie Mellon University to synthesize nanoencapsulates of a variety of materials.

As an illustrative example of the morphology of these particles, Fig. 12 shows a high resolution transmission electron microscopy (HRTEM) image of Gd_2C_3 carbide nanocrystals encapsulated in curved graphitic shells particle sizes in the 10 to 50 nm range and as many as 50 graphitic layers surrounding a single particle. Carbide formation depends on the metal/carbon phase diagram, e.g. Co and Ni are poor carbide formers. C-encapsulated transition metals free of carbide phases have been synthesized by several groups [201,234]. These are particularly interesting because of their magnetic properties and the ability to form monodomain magnetic particles. Encapsulation of Fe, which is a good carbide

former, has been investigated with carbide nanoencapsulates often formed. In magnetic transition metal systems carbide formation is deleterious to the magnetic induction and therefore usually undesirable.

Among systems that have been investigated, and are of interest to the development of nanocrystalline soft magnetic materials, are the late transition

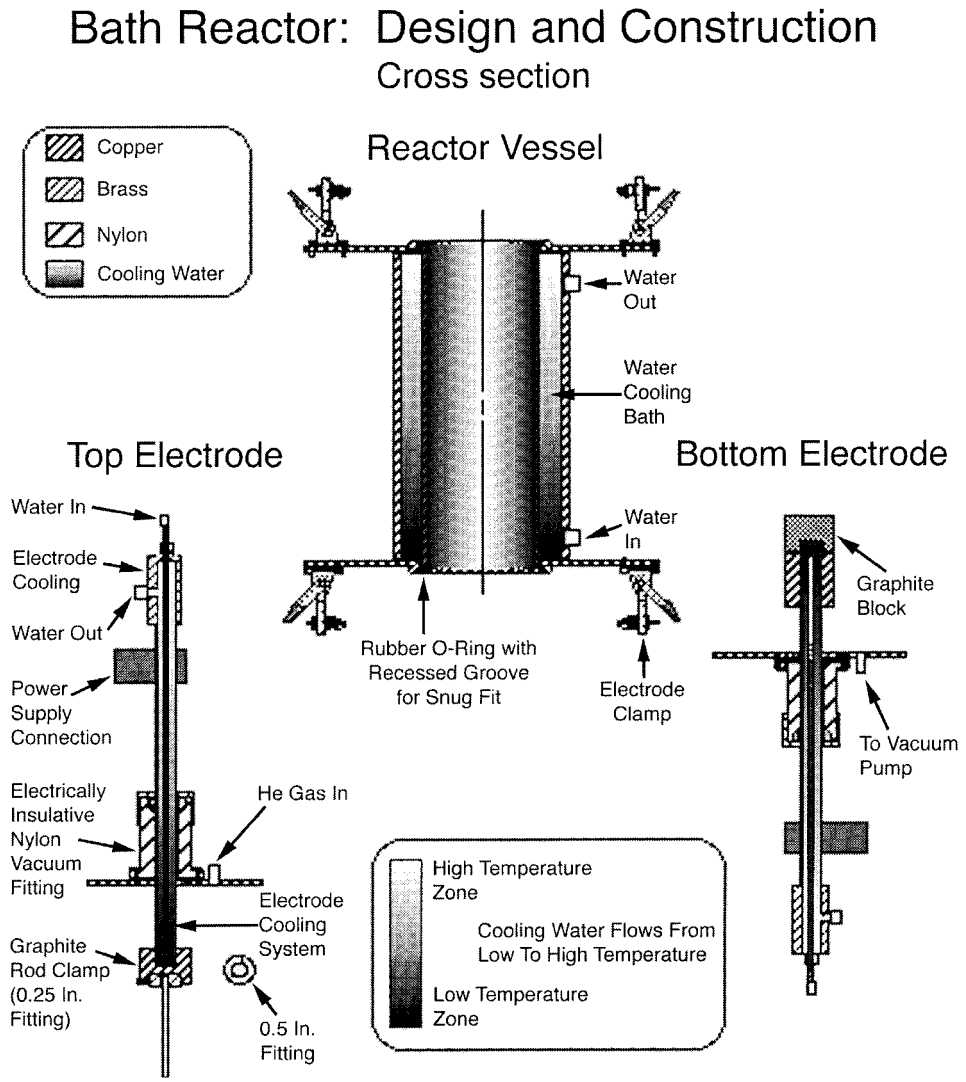

Fig. 11. Carbon arc reactor schematic (F. Johnson and S. Curtin, Carnegie Mellon University). A cylindrical chamber is evacuated and then a He flow is used. In the center, the two electrodes are placed with a small gap between them. A DC arc is struck, and the anode position is adjusted to maintain a constant gap as it is consumed. Both the electrodes and the reactor walls are water-cooled [202].

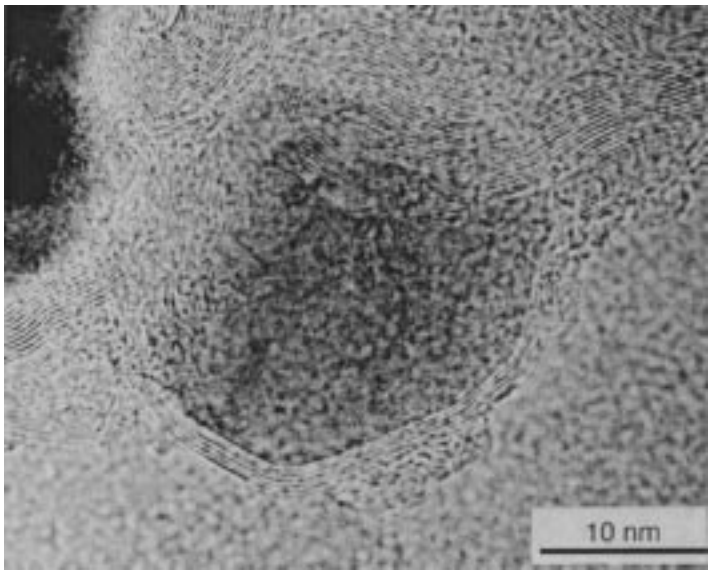

Fig. 12. Gd_2C_3 carbide nanocrystals encapsulated in curved graphitic shells particle sizes in the 10 to 50 nm range and as many as 50 graphitic layers surrounding a single particle [187].

metal alloys. McHenry et al. [202] and Gallagher et al. [60] have employed a Kratschmer–Huffman carbon arc method to synthesize carbon-coated transition metal alloy particles with nanocrystalline dimensions for the $Fe_{1-x}Co_x$[C] system (Fig. 13). The purpose of this work was to produce materials with larger inductions in alloys than in elemental Fe or Co nanoparticles. In particular, they have observed the FCC and BCC structures in the alloys, with no observation of carbides or hexagonal close packed (HCP) Co phase. Co nanoparticle containing soots have been produced with saturation magnetization (per g of soot) in excess of 100 emu/g, and FeCo containing soots with over 200 emu/g and this does not appear to be limiting. Note that pure Fe has a 220 emu/g saturation magnetization. Fe and Co have similar atomic sizes which have lead to the notable lack of chemical segregation in C-arc produced FeCo alloy nanoparticles [241].

A variant of C-arc synthesis produces carbon encapsulated metal nanocrystals using a tungsten arc over a carbon saturated metal pool [48,49]. A tungsten electric arc is used to co-evaporate metal and carbon from a liquid metal pool. In the technique described by Dravid et al. [48,49] an arc is struck between a 6.5 mm diameter W electrode and a 40 mm diameter metal anode (supported by a graphite crucible) in a He atmosphere. The arc between the liquid metal/carbon pool can be maintained for periods of hours with He provided at a small flow near the liquid metal surface. A mixture of uncoated and nanoencapsulated metal particles are collected on the reactor walls. This technique has the advantage of limiting the amount of carbonaceous debris that forms along with the

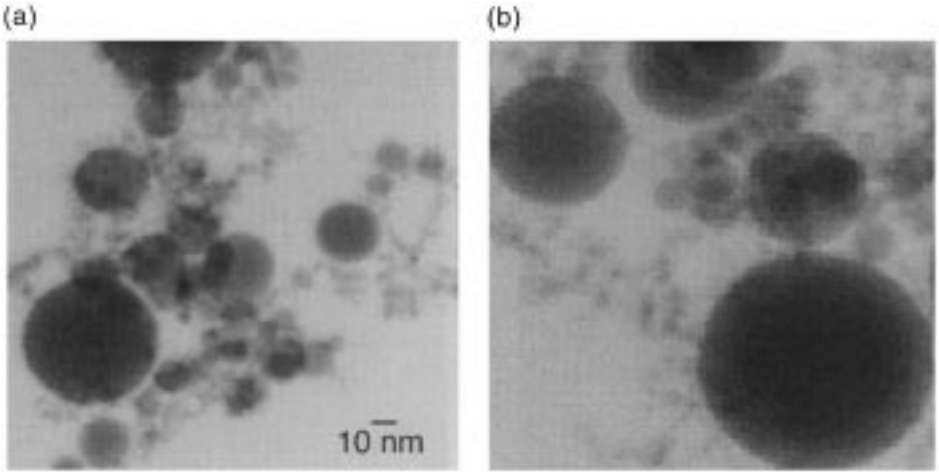

Fig. 13. Bright field TEM images of C-coated FeCo (courtesy of N. T. Nuhfer).

nanoencapsulates. Unencapsulated nanocrystals are easily removed using an acid bath yielding a final sample composed primarily of graphite encapsulated nanocrystals. Jiao et al. [135] have applied this technique to the synthesis of transition metal nanoencapsulates. Host et al. [119,120] have studied graphite encapsulated Ni and Co nanocrystals produced by the tungsten arc method. For more details on this and other techniques for forming C-coated nanocrystals (see Ref. [203]).

3.1.2. Plasma torch synthesis

Plasma synthesis is a recent development in synthetic routes for the production of magnetic nanoparticles [240]. This plasma technology is based around a radio frequency (RF) plasma torch. Thermal plasma synthesis has already proven its scalability to production of industrial quantities [26]. A wide variety of starting materials and reactant gases can be used as feedstocks and many classes of materials, including metals, alloys, carbides, and nitrides can be synthesized. It offers the significant advantage of providing a continuous method for the productions of C-coated nanoparticles. Typical plasma torch techniques are used to deposit low to intermediate melting temperature metals. In order to vaporize carbon to produce nanoencapsulates, etc. a much larger power density needs to be present in the plasma. For this more sophisticated hybrid plasma and RF plasma techniques have been used.

Radio frequency plasma torches (Fig. 14(a)) are electrodeless discharges that use magnetic induction to create eddy currents in a flowing gas stream, coupling radio frequency electrical energy in a copper coil into the plasma gas. Unlike direct current (DC) plasma torches, there are no electrodes to degrade over time and contaminate the products. The operator has control over many variables during thermal plasma synthesis, and the choice of operating conditions has a

pronounced effect on the quality of the product. The temperature, flow, and concentration fields in the induction plasma have been well-characterized through mathematical modeling and measurements [26]. The optimum RF frequency, f, and torch radius, r, are related to the coupling efficiency and torch stability. The skin depth, d_p, of the plasma is given by $d_p = [\pi\mu\sigma_0 f\,]^{1/2}$, where μ is the magnetic

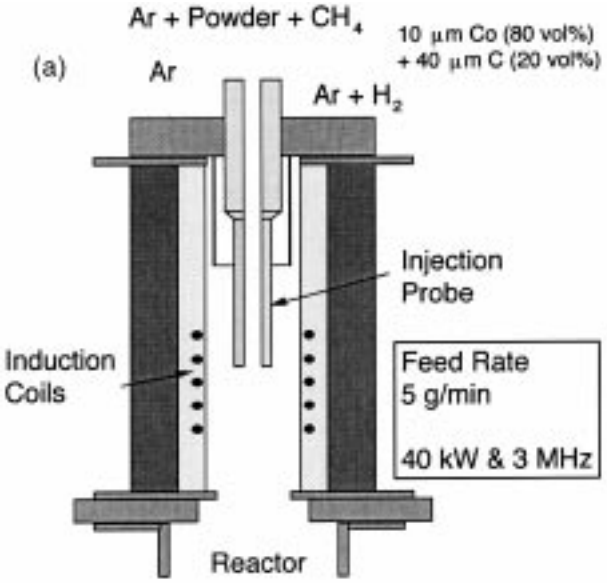

(b)

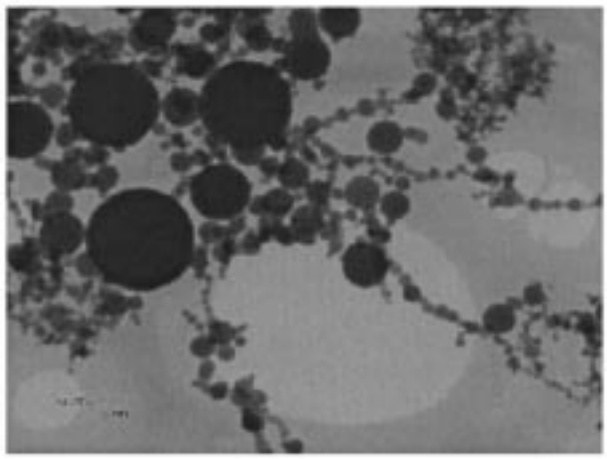

Fig. 14. (a) Schematic of an RF plasma torch reactor showing continuous (gas) feed injection probe, RF induction coil and plasma reaction chamber (courtesy S.A. Majetich) and (b) TEM image of typical plasma torch synthesized FeCo nanoparticles (courtesy J.H. Scott).

permeability of the plasma (approximately equal to μ_0), and σ is the electrical conductivity of the plasma. For an argon plasma at one atmosphere and an average temperature of 8000 K, $\sigma = 10^3\ W^{-1}m^{-1}$. With a frequency of 3 MHz the skin depth is ~9 mm. The optimum coupling of electrical energy into the plasma occurs when the ratio of the plasma radius to the skin depth, r/d_p, is between 1.5 and 2.5 [26,27]. Most of the energy is dissipated in the cylindrical outer shell of the plasma defined by the skin depth.

Turgut et al. [264,265] have employed plasma torch synthesis techniques to produce a variety of encapsulated and unencapsulated magnetic nanoparticles. C-coated Fe_xCo_{1-x} ($x = 0.50$, 0.45, 0.40, 0.35, 0.30, 0.25) nanoparticles were produced using an RF plasma torch where the only C source was acetylene used as a carrier gas. Structural determination by X-ray diffraction (XRD) indicated a single BCC α-FeCo phase along with graphitic C for all compositions. A Scherrer analysis of the peak widths revealed particles to have an average diameter of 50 nm. TEM indicated a log-normal size distribution. Energy dispersive X-ray analysis (EDX) indicated compositional fluctuations of a few atomic percent for individual particles of a nominal composition attributed to starting with elemental rather than alloy precursors.

Magnetic properties of nanoparticles with alloy compositions $Fe_{50}Co_{50}$, $Fe_{55}Co_{45}$, $Fe_{60}Co_{40}$, $Fe_{65}Co_{35}$, $Fe_{70}Co_{30}$ and $Fe_{75}Co_{25}$ have been measured within the temperature range 4–300 K. Temperature dependent magnetization measurements have revealed the effects of atomic ordering in the nanoparticles. The variation of the saturation magnetization discussed below with temperature showed variation near the bulk order–disorder ($\alpha \rightarrow \alpha'$) transformation temperature, as well as loss of magnetization at the $\alpha \rightarrow \gamma$ structural phase transition temperature. Other features of $M(T)$ near 500–550°C are consistent with prior observations of a '550°C structural anomaly' which has been observed in bulk alloys with less than perfect order.

Scott et al. [240,241] have examined the issue of chemical homogeneity in plasma torch synthesized FeCo alloy powders. To distinguish between inherent fluctuations and inhomogeneity introduced by poorly mixed starting material, $Fe_{50}Co_{50}$ nanoparticles were prepared using mixtures of elemental powders and a pre-alloyed $Fe_{50}Co_{50}$ starting material produced by ultrasonic gas atomization. The resulting thermal plasma product was examined with energy dispersive X-ray spectrometry, the nanoparticles produced from alloy precursor showed a smaller spread in Fe/Co ratio than nanoparticles produced from mixed elemental powders. An increased Fe/Co dispersion for the mixed element powders suggests that precursor homogeneity can persist through the plasma processing to impact the quality of the final nanoparticle powder.

3.1.3. Mechanical milling techniques

Mechanical alloying techniques [13] have been utilized to produce amorphous and nanocrystalline alloys as well as metal/non-metal composite materials. To produce amorphous or nanocrystalline alloy particles, elemental or compound powders are milled in an inert atmosphere as shown in Fig. 15. If the mechanical

milling imparts sufficient energy to the constituent powders a homogeneous alloy can be formed. Based on the energy of the milling process and thermodynamic properties of the constituents the alloy can be rendered amorphous by this processing. The empirical rules for producing amorphous powders by such a method are similar to those enumerated for bulk amorphous alloy synthesis though the process conditions are dramatically different.

Mechanical alloying is a non-equilibrium processing tool which can be used to produce metastable phases. Mechanical alloying has been reported as a means of synthesizing:

1. Amorphous alloys via solid state reaction (aided by mechanical work) of two crystalline elemental metals in multilayer systems with very fine interlayer thickness.
2. Metastable or disordered intermetallic phases [238].
3. Metastable intermetallic phases in configurations far from equilibrium [22].
4. Mechanically alloyed amorphous phases by ball milling, etc. [119,120,154,155].

Mechanical milling is typically achieved using SPEX (high energy shaker), planetary ball, or tumbler mills. The energy transferred to the powder from refractory or steel balls depends on the rotational (vibrational) speed, size and number of the balls, ratio of the ball to powder mass, the time of milling and the milling atmosphere. Milling in cryogenic liquids can greatly increase the brittleness of the powders influencing the fracture process. As with any process that produces fine particles, adequate steps to prevent oxidation is necessary. This requires that

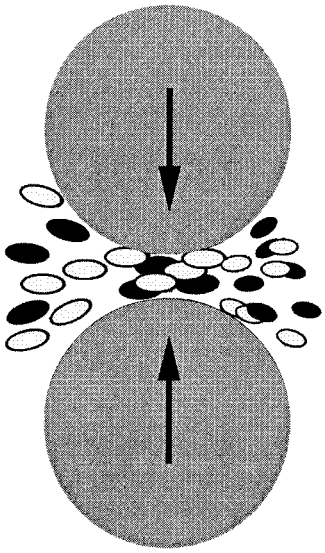

Fig. 15. Schematic representation of the principle of mechanical milling.

the milling take place in an inert atmosphere and that the powder particles be handled in an appropriate vacuum system or glove box.

A typical progression of microstructure during the milling process (for a metallic material) begins with (1) plastic deformation of the constituent particles, (2) followed by fracture and (3) then by a stage of particle welding. The eventual interplay between fracture and re-welding leads to homogenization of the chemistry, refinement of the particle size and disorder in the atomic structure (with eventual amorphization in alloys of appropriate chemistry). The particle size can be observed to reach steady state quite quickly while structural and phase evolution can continue over prolonged time periods.

The thermodynamic and kinetic principles for amorphization through solid state synthesis or mechanical alloying have been enumerated by Schwarz and Johnson [237] and Johnson [135]. Schwarz and Johnson [237] first demonstrated the formation of amorphous alloys by solid state reaction synthesis starting with multilayers of A and B constituents. For producing an amorphous A–B alloy from its constituents:

1. A large negative heat of mixing, ΔH_{mix}, between A an B is desired.
2. A large disparity (asymmetry) in the diffusion coefficients of one in the other is also desired (i.e. $D_{\mathrm{B}} \gg D_{\mathrm{A}}$).

These principles have been used to explain the elegant solid state amorphization reactions of Schwarz and Johnson [237]. Modifications of the theory behind solid state amorphization to include mechanical working terms have been made to explain the amorphization process which occurs in mechanical alloying.

Yavari and Desre [279] have discussed the thermodynamic and kinetic requirements for amorphization during mechanical alloying. Because of the additional influence of mechanical working the requirements are not as restrictive as with solid state reaction synthesis. Again considering A–B alloys (made from A and B starting constituents) they conclude that the requirement of a large negative heat of mixing, ΔH_{mix}, between A and B does in fact allow for amorphization over wider compositional ranges. On the other hand, for $\Delta H_{\mathrm{mix}} \sim 0$ amorphization can in fact occur if the interlayers are kept below a critical thickness. This distinction is attributed to the fact that the amorphous phase undergoes work softening and the crystalline phase work hardening during the course of mechanical alloying. This, in turn, leads to an evolution of the free energy which favors the amorphous phase even when $\Delta H_{\mathrm{mix}} \sim 0$ and $D_{\mathrm{B}} \sim D_{\mathrm{A}}$. Further, mixing kinetics are accelerated by the formation of volume defects and internal surfaces associated with the heavy deformation which occurs during mechanical alloying.

Schwarz [239] has modeled the amorphization process during mechanical alloying using a solid-state interdiffusion model in which disclocation pipe diffusion plays a significant role. Mechanical alloying is viewed as continuously producing fresh metal/metal surfaces with a high density of dislocations. In the mechanical alloying process, powder particles are subjected to stresses which exceed their mechanical strength for short times (on the order of a few microseconds). On the other hand, for times on the order of seconds the particles

are unstressed. During this longer time period solute atoms diffuse along the core of dislocations left behind from the short time deformation. The dislocations act as short-circuit diffusion paths which allow for large solute supersaturation. This so called 'dislocation solute pumping (DSP)' mechanism could in fact be operative for alloys in which $\Delta H_{\mathrm{mix}} > 0$ as long as the solute-dislocation core interaction exceeds the chemical barrier.

In the following we cite some examples of mechanical alloying as applied to interesting soft magnetic alloys:

Haruyama and Asahi [81] have prepared amorphous Ni–Zr alloys by mechanical alloying of elemental crystal powders. They used a high-speed vibratory ball mill in an argon atmosphere with WC and steel milling tools. Amorphous Ni_xZr_{100-x} ($x = 20$–70) alloy powders were obtained after 32 h using a 54 : 1 ball to powder mass ratio. Longer times for amorphization are required for the end compositions. This is explained in terms of the variation of the heat of mixing with x. The heat of mixing is negative and most negative for intermediate compositions. This trend is also apparent in the crystallization temperatures, T_{x1} with peaks at ~830 K for $x = 60$ at%.

Lee et al. [177] have studied phase transformations induced by ball milling in the Fe–Zr system. Structural changes and magnetic properties have been examined in mechanically alloyed $Fe_{1-x}Zr_x$ alloys with ($x = 0.1$, 0.25, 0.3 and 0.5). The alloys were prepared by mechanically alloying in a conventional ball mill starting with elemental powders. Stainless steel balls and a 20 : 1 ball to powder charge were employed. Mixed 10 nm α-Fe nanocrystals and an amorphous phase were observed during the early stages of crystallization. Further processing resulted in crystallization of the amorphous phase into α-Fe and Zr_2Fe crystalline phases. The solid state amorphization was attributed to interdiffusion between layers. TEM selected area diffraction (SAD) indicated two diffuse halo's suggesting phase separation into Fe-rich and Zr-rich amorphous regions.

Zhang et al. [292] have prepared $Fe_{80}Zr_8B_{11}Cu_1$ alloy powders by ball milling mixtures of Fe–Zr, Fe–B and elemental Fe and Cu powders. The ball milled powders in a planetary ball mill using a 40:1 ball to powder charge and a rotational speed of 160 rpm. Methanol was used to prevent excessive particle welding. They monitored crystallization using XRD, electron microscopy and Mössbauer spectroscopy. Annealing temperatures of 673–1173 K were employed. At 873 K a 61% volume of α-Fe was observed. At 1173 K the amorphous phase is completely converted to α-Fe + ZrB_2 suggesting a two or more step crystallization process.

3.1.4. Powder consolidation

It should be noted that many of the materials produced by the amorphous precursor nanocrystallization route described below have also been ground into powders. It is these materials that the most extensive powder consolidation has been performed. Kojima et al. [157,158] have described warm extrusion of $Fe_{84}Nb_7B_9$ and $Fe_{90}Zr_7B_3$ alloys, respectively. The first alloys ($Fe_{84}Nb_7B_9$) [157] were extruded at temperatures between 290 and 450°C using pressures between

824 and 1208 MPa. A second report in 1995 described extrusion of $Fe_{90}Zr_7B_3$ at temperatures between 400 and 425°C using pressures between 920 and 940 MPa. These consolidation routes took advantage of the fact that amorphous powders soften in the vicinity of the crystallization temperature. The consolidated materials achieved densities greater than 99% of those of the melt-spun ribbons. Grain sizes of 9–11 nm were observed for the $Fe_{84}Nb_7B_9$ alloy and 20–30 nm for the $Fe_{90}Zr_7B_3$ alloy after extrusion.

3.2. Rapid solidification processing

Amorphous alloys are of interest because they do not have any long-range atomic order. As a result these materials have high resistivities, low magnetocrystalline anisotropy and no microstructural inhomogeneities. As a result, these materials are observed to have small hysteretic and eddy current losses. Amorphous alloys are typically formed by rapid solidification processing routes, though more conventional solidification routes are possible for bulk amorphous alloys as discussed below.

The study of metallic glasses dates back to the pioneering work of Pol Duwez at Caltech in the 1950s. Duwez employed atomization [51] and gun techniques [52] prior to splat quenching (for a review, see Refs. [53,54]). Ferromagnetic amorphous alloys were first reported by Mader and Nowik [186]. Soon after, Tsuei and Duwez [263] reported splatquenched amorphous ferromagnets with interesting soft magnetic properties. Rapid solidification processing is reviewed only in a cursory manner here, citing techniques which have been employed to produce materials which are discussed in this article. The subject of rapid solidification processing is much broader and the subject of many good reviews [23,46,224].

Amorphous metallic alloys are synthesized by rapid solidification processing techniques in alloy systems where the liquid phase remains stable to low temperature and there are competing crystalline phases below the liquidus, i.e. systems with deep eutectics. These are typically metastable phases. Amorphous alloys can be produced by a variety of rapid solidification processing routes including splat quenching, melt spinning, gas atomization and condensation from the gas phase. These typically require cooling rates of greater than 10^4 K/s for binary alloys at a eutectic composition. Among the most common rapid solidification processing technique is melt spinning which yields amorphous metallic ribbons typically 20 μm in thickness and gas atomization techniques that yield several μm to submicron powders the smallest of which can be made amorphous. Fig. 16 shows a schematic of a melt-spinning apparatus used to produce amorphous metallic ribbons. Here a molten alloy is pushed through the orifice of a pressurized crucible onto a rotating copper wheel. Lim et al. [187,179] have examined the influence of melt temperature on the final magnetic properties of FINEMET alloys. The melt temperature influences the ribbon thickness and therefore the final nanocrystal size distribution throughout the transformed ribbon after nanocrystallization.

Massalski [197] has discussed the thermodynamic and kinetic considerations for the synthesis of amorphous metallic phases. Glass forming ability (GFA) involves suppressing crystallization by preventing nucleation and growth of the stable crystalline phase so as to maintain a metastable quenched liquid phase. The solidification of a eutectic liquid involves partitioning of the constituents so as to form the stable crystalline phase. Glass forming ability can be correlated with the reduced glass forming temperature, T_{rg}, which is defined as $T_{rg} = (T_L - T_g)/T_L$, where T_L and T_g are the liquidus and glass transition temperatures, respectively. Five criteria have been enumerated for promoting the partitionless (i.e. with no composition change) freezing of a liquid to form a metallic glass. These are:

1. *Quenching to below the* T_0 *curve*: The so-called T_0 curve represents the temperature below which there is no thermodynamic driving force for partitioning and the liquid freezes into a solid of the same composition.
2. *Morphological stability* depends on the comparison of imposed heat flow and the velocity of the interface between the amorphous solid and liquid phase.
3. *Heat flow*: The supercooling of the liquid phase must exceed L/C where L is the latent heat of solidification and C is the specific heat of the liquid, so as to prevent segregation.
4. *Kinetic criteria*: A critical cooling rate, R_c, for quenching in the liquid phase is empirically known to depend intimately on the reduced glass forming temperature, T_{rg}.
5. *Structural*: Different atomic size ratios typically with difference exceeding ~13% are desired to retard the diffusional motion necessary for partitioning.

A variety of thin film deposition techniques have also been utilized to produce amorphous metallic alloys. A detailed discussion of these deposition techniques is beyond the scope of this article. However, we do here summarize a few pertinent observations from the literature. Makino et al. [302] have studied sputtered Fe–Zr–B thin films in which 10–20 nm BCC Fe nanograins were obtained after annealing. Makino et al. [190,191] have also studied the microstructure of

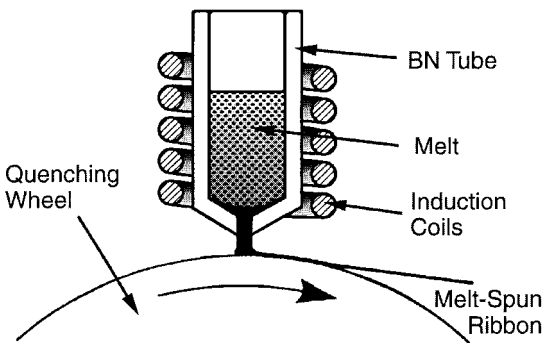

Fig. 16. Melt-spinning apparatus schematic used to produce amorphous metallic ribbons.

$Fe_{87.9}Hf_{9.8}B_{1.3}$ thin films produced by sputtering in both as-deposited and annealed states. The annealed film (1 h at 600°C) was observed by HRTEM to consist of nearly spherical 10–15 nm grains of a BCC phase and an amorphous Hf-rich phase (< 5 nm thick) surrounding the BCC phase.

For the sake of completeness it should be noted that by analogy to nanocrystalline materials the synthesis of so-called 'nanoglasses' has been proposed [67]. Rapid solidification in the gas phase (e.g. ultrasonic gas atomization) or upon splatting on a substrate can lead to the formation of structureless nanometer-sized glassy droplets as opposed to nanocrystals. Issues of compaction of nanoglass materials have not been explored.

3.3. Solidification processing of bulk amorphous alloys

Bulk amorphous alloys with large glass forming abilities have been found in a variety of alloy systems including Ln–Al–TM (Ln = lanthanide metal, TM = transition metal) systems [121]. These bulk amorphous alloys have been synthesized with diameters as large as 40 mm. using copper mold casting techniques [131]. The first of these alloys were not produced for potential magnetic applications. Recently, ferromagnetic bulk amorphous alloys with diameters as large as 2 mm, have been produced in the Fe–Al–Ga–P–C–B system with inductions as large as 1.1 T [130].

Bulk amorphous alloys are distinguished by their glass forming abilities which are quantified in terms of the width of the supercooled region, ΔT_x. ΔT_x is defined as the difference between the crystallization temperature, T_x, and the glass transition temperature, T_g. Differential scanning calorimetry (DSC) curves for a typical bulk amorphous alloy are shown in Fig. 17 along with a cross-sectional micrograph of a 1.5 mm cast $Fe_{73}Al_5Ga_2P_{11}C_5B_4$ bulk amorphous alloy. Bulk amorphous alloys have been synthesized by conventional single roller melt spinning and by more traditional copper mold casting. As a result of the large glass forming abilities, slower solidification rates and/or larger component size can be used while retaining the amorphous material.

3.4. Primary nanocrystallization of amorphous precursors

Amorphous alloys of appropriate chemical compositions, crystallized at temperatures above their primary crystallization temperature but below the secondary crystallization temperature, can yield nanocrystalline grains with an amorphous intergranular material. Crystallization parameters can be optimized so as to yield 10–50 nm α-FeSi, α-Fe, α- or α′-FeCo particles surrounded by a thin TL–TE–B–Cu intergranular phase. By and large the crystallization process is performed by inert gas furnace annealing. The resulting structure of many of these alloys is discussed in Section 4. This is the basis of the processing routes used to produce the interesting FINEMET, NANOPERM and HITPERM alloys. These materials differ in the nanocrystalline phase which forms and in the relative amounts of non-magnetic additions to the original amorphous phase. Greater Fe

concentrations and the effect of Co additions (as in the Slater-Pauling curve) impact on the inductions and Curie temperatures of each of these materials. Details of the various crystallization reactions and their kinetics are discussed in Section 4.

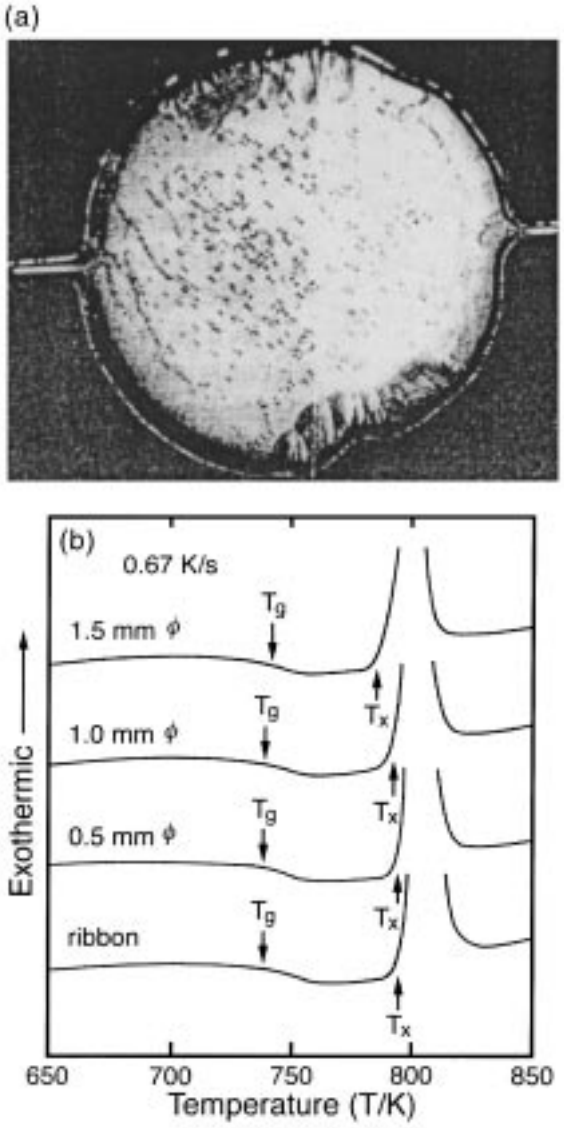

Fig. 17. (a) A cross-sectional optical micrograph of a 1.5 mm cast cylinder of an $Fe_{73}Al_5Ga_2P_{11}C_5B_4$ bulk amorphous alloy and (b) DSC curves for as-cast $Fe_{73}Al_5Ga_2P_{11}C_5B_4$ bulk amorphous alloy cylinders as compared with melt-spun glassy ribbons of the same composition [125].

Many variations on the amorphous precursor nanocrystallization route have been reported in the literature. For example, Lanotte and Ianotti [176] have examined nanocrystallization of FINEMET using laser annealing. They were able to produce ~15 nm nanocrystals of α-Fe(Si) and good soft magnetic properties by this route. This technique offers some potential flexibility as compared with conventional furnace annealing techniques. Kim et al. [142,143] have used flash annealing of a melt-spun (FINEMET) $Fe_{83}B_9Nb_7Cu_1$ alloy. Enhanced soft magnetic properties were attributed to a very fine nanocrystalline grain size achieved by this process.

Fe–Ta–C amorphous precursors have also been crystallized to form nanocrystalline magnetic alloys. The nanocrystalline structure of Fe–Ta–C materials differs from that of typical FINEMET and NANOPERM alloys (see Table 3). In the latter a continuous amorphous phase coats and couples the nanoparticles. Soft magnetic properties depend intimately on the nature of the nanocrystal-amorphous-nanocrystal coupling. In the former, a refractory carbide phase tends to form at grain boundary triple points (see Fig. 18). These carbides tend to pin grain boundaries with consequent prevention of coarsening. This type of nanocrystalline microstructure does not prohibit direct exchange between the magnetic nanoparticles.

4. Thermodynamic and transformation kinetic considerations for amorphous and nanocrystalline materials

Thermodynamic properties and transformation kinetics (for example for crystallization from an amorphous precursor) can be studied using a variety of techniques. Common among these are isothermal annealing followed by structural (microstructural) observations, DSC, DTA, and in magnetic materials, thermomagnetic analysis (TMA). These techniques have been used to study glass transformation and crystallization temperatures in amorphous and bulk amorphous alloys.

Crystallization kinetics have been studied by a variety of techniques including HRTEM, in situ XRD, extended X-ray absorption fine structure (EXAFS) measurements, resistance measurements, magnetic measurements, etc. These

Table 3
Attributes of nanocrystalline ferromagnetic materials produced by an amorphous precursor route (see Tables 8 and 9 for references)

Alloy name	Typical composition	Nanocrystalline phase	B_s(T)	T_c(°C)
FINEMET	$Fe_{73.5}Si_{13.5}B_9Nb_3Cu_1$	α-FeSi, $FeSi(DO_3)$	1.0–1.2	< 770
NANOPERM	$Fe_{88}Zr_7B_4Cu$	α-Fe(BCC)	1.5–1.8	770
HITPERM	$Fe_{44}Co_{44}Zr_7B_4Cu$	α-FeCo,(BCC) α′-FeCo(B2)	1.6–2.1	> 965

typically observe or relate the volume fraction transformed of the crystalline phase, X, to a physical parameter and then measure the evolution of that parameter over time. Johnson–Mehl–Avrami (JMA) kinetics has been commonly used to analyze the time evolution of the volume fraction transformed. The

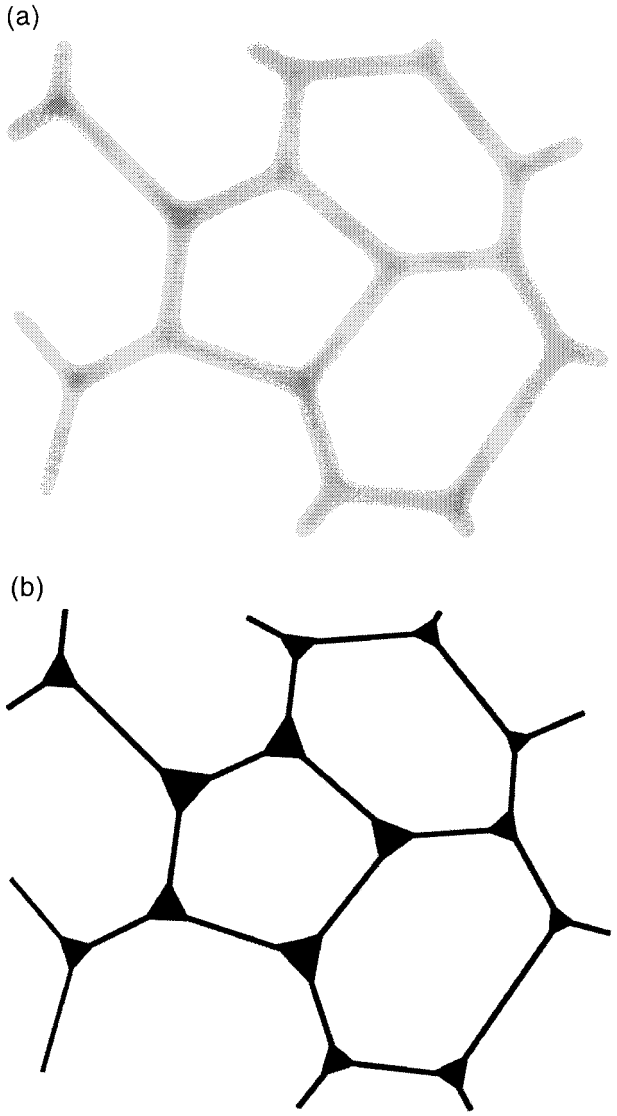

Fig. 18. Schematic of nanocrystalline alloys of two types. The first type (a) contains nanocrystalline ferromagnetic grains surrounded by a more weakly ferromagnetic grain boundary phase. The second type (b) contains nanocrystalline ferromagnetic grains whose grain boundaries are pinned by a refractory carbide phase [87,89].

fraction transformed in the JMA kinetics formalism exhibits a time dependence of the form:

$$X = 1 - \exp\left[-(kt)^n\right] \tag{19}$$

where n is a power law exponent that can be used to distinguish the dimensionality of the growth process, X is the volume fraction transformed, t is time, k is a thermally activated rate constant, which obeys an Arrhenius relationship of the form:

$$k = k_0 \exp\left[-E/k_B T\right] \tag{20}$$

where E represents the activation energy barrier to crystallization. At small times the general Eq. (19) reduces to:

$$X = (kt)^n \tag{21}$$

and $\mathrm{d}\ln X/\mathrm{d}\ln t$ gives the exponent n. Also from the early stage approximation it can be determined that: $\mathrm{d}X/\mathrm{d}t = nk^n t^{n-1}$ and for $n > 1$, $\mathrm{d}X/\mathrm{d}t = 0$, at $t = 0$. For $n = 1$, $\mathrm{d}X/\mathrm{d}t = k$, a non-zero constant at $t = 0$.

The fundamental importance of these empirical transformation kinetics lies in coupling them with a model for nucleation and growth, where the exponent n can be compared with model specific predictions of nucleation and growth kinetics (in which the particle geometry intimately determines the time exponent). For example, Avrami's analysis of the nucleation and growth process leads to a time exponent, $n = 3$ if all nuclei are present at $t = 0$ and the particles are spherical and grow at a constant rate. On the other hand, if all nuclei are present at $t = 0$ but the subsequent growth of spherical particles is parabolic (i.e. growth rate is proportional to $t^{-1/2}$), then a time exponent $n = 3/2$ is predicted. Johnson and Mehl treated the problem of growth of spherical particles after constant random nucleation in untransformed regions. With a constant growth rate, G, a time exponent $n = 4$ is arrived at. If growth is parabolic after constant random nucleation then a growth exponent of $n = 5/2$ is predicted. In general, the growth exponent for spherical particles can be expressed:

$$n = p_e + q_e \tag{22}$$

Where $p_e = 0$ for immediate nucleation, $p_e = 1$ for constant nucleation with time, $q_e = 3$ for linear growth and $q_e = 3/2$ for parabolic growth of spherical particles. Other values of n are possible, for example, if the growth is not of spherical particles. Fitting of these exponents is fraught with many experimental uncertainties and observations must be viewed cautiously.

4.1. Calorimetry and stability of bulk amorphous materials

A measure of the stability of bulk amorphous alloys is the width of the supercooled region, ΔT_x. ΔT_x is the difference between the crystallization

temperature, T_x, and the glass transition temperature, T_g. Alloys with large supercooled regions can be made amorphous with slower cooling rates or larger thickness than conventional glass forming alloys. The discovery of bulk amorphous alloys has evolved from the studies of ternary, quaternary, quinternary and larger multi-component glass forming systems. The state of affairs for stability in conventional amorphous alloys with up to ternary additions has been reviewed by Chen [33]. Chen has reported on the formation of amorphous phases in Fe–P–C, Fe–P–B, F–B–C, and Fe–Al–B systems. More recently, Inoue et al. [122] have investigated ternary alloy systems such as Fe–P–C and Fe–P–B where he considered the glass forming ability. In these ternary alloys they typically observed $\Delta T_x < 25$ K.

Studies of ternary alloys paved the way for studies of quaternary and larger multicomponent sytems. These alloys systems are guided by the so-called confusion principle and the three empirical rules (previously discussed in Section 2.6.):

1. multicomponent systems with three or more constituent elements,
2. different atomic size ratios typically with difference exceeding ~13% and
3. negative heats of mixing among the constituent alloying elements.

A variety of observations, for different bulk amorphous alloy systems with 4, 5 and 6 non-magnetic components added to ferromagnetic Fe, are summarized in Table 4. These include crystallization, T_x, and glass transition temperatures, T_g, the glass forming range, ΔT_x, the sample dimension, D, the heat of crystallization, ΔH_x, and the crystallization reaction. These alloys are of considerable interest because of their large glass-forming region coupled with ferromagnetism at room temperature.

Inoue et al. [125] have observed that the high thermal stability of the bulk amorphous alloys has been attributed to three separate contributions. These are:

1. More efficient dense random packing of constituents with significantly different atomic sizes, especially among P, C, and B.
2. Higher energy barriers for the precipitation of Fe–M compounds due to strong interactions between P, C, and/or B and Al.
3. Higher barriers to formation of Fe–B and Fe–C compounds due to Ga additions which are soluble in Fe but immiscible with B or C.

For Ge containing alloys they have also promoted the possible importance of Ge–B and Ge–C pairing [125].

Inoue and Gook [124] have investigated the effects of Nb, Mo, Cr and Co substitutions in $Fe_{72-x}Al_5Ga_2P_{11}C_6B_4M_x$ bulk amorphous alloys [M = Nb, $x = 2$; M = Mo, $x = 5$; M = Cr, $x = 4$; and M = Co, $x = 6$. All of these substitutions were found to extend the supercooled liquid region, ΔT_x. ΔT_x was determined to be 60 K for the parent alloy and increase to 66 K for M = Nb, 62 K for M = Mo, 61 K for M = Cr and M = Co. For these alloys a single crystallization reaction was observed of the form:

$$\text{Amorphous} \rightarrow \alpha\text{-Fe} + Fe_3P + Fe_3C + Fe_3B \quad (23)$$

On the other hand, for alloys with 2% Cu or 2% Ni additions, no glass transition occurs prior to crystallization. A two-stage crystallization process is observed with the reactions:

$$\text{Amorphous} \rightarrow \text{Amorphous}' + \alpha\text{-Fe}$$

$$\text{Amorphous}' + \alpha\text{-Fe} \rightarrow \alpha\text{-Fe} + Fe_3P + Fe_3C + Fe_3B \quad (24)$$

The authors interpreted this as evidence that a supercooled region corresponded to crystallization being suppressed by a barrier to the redistribution of

Table 4
Summary of experimental observations, for different bulk amorphous alloy systems with 4, 5 and 6 non-magnetic components added to ferromagnetic Fe[a]

Alloy	Reference	T_x (K)	T_g (K)	ΔT_x (K)	D (mm)	ΔH_x (kJ/mol)	RXN
$Fe_{72}Al_5Ga_2P_{11}C_6B_4$	[127]	798	738	60	0.02		(a)
$Fe_{70}Al_5Ga_2P_{11}C_6B_4Nb_2$	[127]			66	0.02		(a)
$Fe_{68}Al_5Ga_2P_{11}C_6B_4Mo_4$	[127]			62	0.02		(a)
$Fe_{68}Al_5Ga_2P_{11}C_6B_4Cr_4$	[127]			61	0.02		(a)
$Fe_{66}Al_5Ga_2P_{11}C_6B_4Co_6$	[127]	793	732	61	0.02		(a)
$Fe_{73}Al_5Ga_2P_{11}C_5B_4$	[130]				0.5–4		
$Fe_{72}Al_5Ga_2P_{11}C_5B_4Si_1$	[130]	785	732	53	0.5–4		
$Fe_{80}P_{12}B_4Si_4$	[128]	789	753	36	0.02		
$Fe_{76}Al_4P_{12}B_4Si_4$	[128]	780	738	46	0.02		
$Fe_{74}Al_4Ga_2P_{12}B_4Si_4$	[128]	786	737	49	0.02	3.76	
$Fe_{72}Al_5Ga_2P_{11}C_6B_4$	[123]	793	732	61			
$Fe_{74}Al_5P_{11}C_6B_4$	[124]			45			
$Fe_{72}Al_5P_{11}C_6B_4Ge_2$	[124]			60			(b)
$Fe_{72}Al_5P_{11}C_6B_4Ga_2$	[124]			60			
$Fe_{73}Al_5Ga_2P_{11}C_5B_4$	[125]	785	732	53	0.5, 1.0	3.76	
$Fe_{80}P_{11}C_5B_4$	[125]			24			
$Fe_{75}Al_5P_{11}C_5B_4$	[125]			36			
$Fe_{78}Ga_2P_{11}C_5B_4$	[125]			31			
$Fe_{56}Co_7Ni_7Zr_2Nb_8B_{20}$	[167]	873	817	56			(c)
$Fe_{56}Co_7Ni_7Zr_2Ta_8B_{20}$	[167]	874	811	63			(c)
$Fe_{56}Co_7Ni_7Zr_{10}B_{20}$	[132]	888	820	68			(d)
$Fe_{56}Co_7Ni_7Zr_{10}B_{20}$	[133]	887	814	73	2.0		
$Fe_{56}Co_7Ni_7Zr_8Nb_2B_{20}$	[133]	913	828	85	2.0		
$Fe_{60}Co_8Zr_{10}Mo_5W_2B_{20}$	[133]	962	898	64	6.0		
$Co_{56}Fe_{16}Zr_8B_{20}$	[133]	878	839	39			
$Fe_{70}Al_5Ga_2P_{12.65-x}C_{5.75}B_{4.6}Si_x$ ($x = 0$–4)	[205]			60	0.28		
$Fe_{77}Al_{2.14}Ga_{0.86}P_{11-x}C_5B_4Si_x$ ($x = 0$–1)	[205]						

[a] (a) Am → α-Fe + Fe_3P + Fe_3C + Fe_3B (b) Am → α-Fe + Fe_3P + Fe_3C + Fe_3B + Fe_2B (c) Am → Am′ + γ−Fe → γ−Fe + $Co_3Nb_2B_5$ + Ni_8Nb (d) Am → α−Fe + Fe_2Zr + Fe_3B.

constituents on a long-range scale, as would be necessary for the simultaneous crystallization of four components as described in Section 4.1.

In an exciting recent development, Koshiba et al. [167] have observed a wide supercooled region $\Delta T_x = 60$ K in the melt-spun alloys $Fe_{56}Co_7Ni_7Zr_2Nb_8B_{20}$ and $Fe_{56}Co_7Ni_7Zr_2Ta_8B_{20}$. These alloys have a single metalloid component with three magnetic TM and two TE species. In these alloys a two-stage crystallization is observed:

$$\text{Amorphous} \rightarrow \text{Amorphous}' + \alpha\text{-Fe}$$

$$\text{Amorphous}' + \alpha\text{Fe} \rightarrow \alpha\text{-Fe} + Co_3Nb_2B_5 + Ni_8Nb \tag{25}$$

Mizushima et al. [205] have investigated the effects of Si additions on thermal stability and soft magnetic properties of Fe–Al–Gr–P–C–B bulk amorphous alloys. They examined two alloy systems: $Fe_{70}Al_5Ga_2P_{12.65-x}C_{5.75}B_{4.6}Si_x (x = 0-4)$ and $Fe_{77}Al_{2.14}Ga_{0.86}P_{11-x}C_5B_4Si_x$ $(x = 0–1)$ alloys. In all cases T_x, ΔT_x and effective permeabilities are increased by Si substitution for P. ΔT_x reached 60 K and the maximum amorphous thickness, 280 μm for the first of these alloy systems. Even more recently, Inoue et al. [133] have reported $\Delta T_x = 85$ K in the melt-spun alloy $Fe_{56}Co_7Ni_7Zr_8Nb_2B_{20}$! This large ΔT_x is significant for its implications for glass forming ability and for the potential dimensions possible for the amorphous phase.

4.2. Primary and secondary crystallization events in nanocrystalline alloys

4.2.1. FINEMET alloys

Noh et al. [215] have studied microstructural changes and crystallization processes in Fe–Si–B, Fe–Cu–Si–B, Fe–Nb–Si–B and Fe–Cu–Nb–Si–B amorphous alloys in order to elucidate the roles of combined additions of Cu and Nb to Fe–Si–B alloys. This in turn was aimed at furthering the understanding of crystallization of FINEMET alloys. They annealed amorphous ribbons at various temperatures for 1 h and observed structure by XRD and crystallization by DTA and magnetic permeability. Noh et al. [216] have studied the influence of B substitutions for Si in FINEMET alloys, of composition $Fe_{73.5}Cu_1Nb_3(Si_xB_{1-x})_{22.5}$ $(x = 0.5–0.8)$. The B additions led to the development of two different ferromagnetic phases in the nanocrystalline alloys. The first was an α-Fe(Si) material with a high Curie temperature and the second an interfacial B-rich phase with a lower Curie temperature. In Si-rich alloys the second (intergranular) phase was not observed to develop. Efthimiadis [55] has examined the effect of Cu additions on crysallisation rates in Fe(Cu)SiB alloys.

Koster and Meinhardt [169] have studied primary crystallization of FINEMET and shown that a size dependent growth rate can be observed to the changing chemistry of the amorphous phase during the evolution of the microstructure. Microstructural control is achieved through the additions of slow diffusing species such as Nb while small Cu or Au additions increase the nucleation rate. Kulik et

al. [175] have also investigated B substitutions for Si in FINEMET-type ($Fe_{73.5}Cu$, $Nb_3Si_{22.5-x}B_x$ with $5 \leq x \leq 10$) alloys. The softest magnets corresponded to those in which primary crystallization of α-Fe(Si) and Fe_3Si occurred. Secondary crystallization of Fe_2B caused magnetic hardening of the nanocrystalline alloy. Mechanical hardening of the amorphous precursor was also observed in incipient primary crystallization and attributed to Cu nucleation (clustering).

Gonzalez et al. [69] have studied the influence of heating rate, up to the primary crystallization temperature, T_x, on the effective magnetic anisotropy in nanocrystalline FINEMET materials. They observed smaller K_{eff} and coercivities in samples that were slowly heated. This slow heating led to a larger extent of crystallization and enhancement of the intergranular coupling.

Zbroszcyk et al. [287–289] have examined the influence of small Co additions to a FINEMET alloy on microstructure and magnetic properties. They compared $Fe_{73.5}Cu_1Nb_3Si_{13.5}B_9$ and $Fe_{66.5}Co_7Cu_1Nb_3Si_{13.5}B_9$ alloys. It was found that Co enhanced the effective nuclear hyperfine field at the ^{57}Fe nucleus. Co additions are observed to lower the volume fraction of the amorphous phase for heat treatments at comparable times and temperatures. It was concluded that Co accelerated the crystallization process, though the nanocrystalline phase remains as the α-FeSi structure type. Generally improved magnetic properties were noted with Co additions.

Moya et al. [207] have also investigated structural evolution and properties of devitrified and crystallized $Fe_{73.5}Si_{22.5-x}B_xNb_3Cu$, FINEMET alloys, with $x = 6$, 8, 9, 10, and 12. Amorphous precursors were produced by melt-spinning. One hour heat treatments were performed between temperatures $T_a = 400$–$540°C$. Structural evolution was examined by X-ray diffraction and Mossbauer spectroscopy. They observed structural relaxation in the amorphous material at $T_a \sim 440°C$ and it's effect on magnetic softening and increasing of the elastic constants of the glass. These effects are reversed at $T_a = 480°C$ where it is proposed that Cu clustering occurs in the first stages of crystallization. At $T_a = 540°C$ the nanocrystalline phase is observed by XRD. B substitutions for Si, in general, are observed to degrade the soft magnetic properties.

Wang et al. [273] have also examined the influence of heating rate on the magnetic properties of FINEMET-related alloys, $Fe_{72.7}Cu_1Nb_2V_{1.8}Si_{13.5}B_9$ and $Fe_{73.5}Cu_1Nb_3Si_{13.5}B_9$ with contrary observations. They observed smaller nanocrystalline grains corresponding to faster heating rates, and consequently larger permeabilities. Hajko et al. [78] have studied the effects of 0–15 at% Cr additions for Fe in FINEMET alloys of composition $(Fe_xCr_{1-x})_{73.5}Cu_1Nb_3Si_{13.5}B_9$ ($x = 0.85$–1.0). Amorphous precursors were produced in the form of melt-spun ribbons. These were then nanocrystallized and studied by DTA and TEM. Cr additions were observed to increase the temperature of the first crystallization peak, T_{x1} while narrowing the interval between T_{x1} and T_{x2}. A third exothermic peak was observed and suggested to be due to crystallization of a chromium-boride. Cr additions were also observed to reduce the primary nanocrystallite grain size and to decrease the Curie temperature.

4.2.2. NANOPERM alloys

Suzuki et al. [253–255] have examined microstructure and magnetic properties after crystallization of an $Fe_{86}Zr_7B_6Cu_1$ amorphous alloy. The resulting nanocrystalline (NANOPERM) microstructure was characterized by a 10 nm BCC Fe phase. They observed the crystallization process to follow the sequence:

$$\text{Amorphous} \rightarrow \alpha\text{-Fe} + \text{amorphous}\ (687^\circ\text{C}) \rightarrow \alpha\text{-Fe} + Fe_3Zr + \text{X}\ (747^\circ\text{C}) \rightarrow \alpha\text{-Fe} + Fe_3Zr + Fe_2Zr + ZrB_2\ (877^\circ\text{C}) \quad (26)$$

Primary crystallization of BCC Fe at 687°C was followed by secondary crystallization of the Fe_3Zr phase and an unidentified phase, *X*, at 747°C. The refractory boride ZrB_2 phase crystallized at a higher (1150 K) temperature. Suzuki et al. [256] have investigated the effects of B additions on crystallization in $Fe_{92}Zr_8$ and $Fe_{91}Zr_7B_2$ amorphous alloys. Primary crystallization temperatures of 804 and 790°C, respectively were observed. B additions in the second alloy led to refinement of the α-Fe nanocrystal grain size due to suppression of coarsening.

Inoue et al. [126–130] have studied the possibility of addition of small amounts of Al and/or Si to $Fe_{91}Zr_7B_2$ and $Fe_{90}Zr_7B_3$ alloys. Amorphous single phases were formed over the entire composition range for $Fe_{91-x}Zr_7B_2Al_x$, $Fe_{90-x}Zr_7B_3Al_x$, $Fe_{91-x}Zr_7B_2Si_x$ and $Fe_{90-x}Zr_7B_3Si_x$ (x =0–15) alloys. Al additions increase the onset temperature for primary crystallization from 780 K for $Fe_{90}Zr_7B_3$ to 820 K for $Fe_{75}Zr_7B_3Al_{15}$ and 814 K for $Fe_{75}Zr_7B_3Si_{15}$. A two step crystallization process was observed for these alloys at all compositions. Importantly, with 2% Si and 1% Al additions, a zero crossing in the saturation magnetostriction of the α-Fe nanocrystalline phase is observed.

Zhang et al. [292] have studied crystallization in ball-milled $Fe_{80}Zr_8B_{11}Cu_1$ alloy crystallization using XRD, electron microscopy and Mössbauer spectroscopy. At a heat treating temperature of 1173 K the amorphous phase is completely converted to α-Fe + ZrB_2 suggesting a two or more step crystallization process. Slawska-Wanienska et al. [247] have studied the crystallization behavior of an as-quenched and heat treated $Fe_{89}Zr_7B_4$ alloy. The observed dendritic growth during low temperature heat treating and nucleation of regular nanocrystals at higher heat treating temperatures. The low temperature dendritic growth is postulated as contributing to larger shape and/or surface anisotropy in those materials. Zhang et al. [291] have studied the structural evolution in an $Fe_{90}Zr_7B_3$ and concluded that the initial crystallization step reported by Suzuki et al. [253–255] Eq. (26), proceeded by the expulsion of Zr from the α-Fe nanocrystals to a Zr and B rich intergranular amorphous phase.

Grabias and Kopcewicz [73] have studied the crystallization process in an $Fe_{81}Zr_7B_{12}$ alloy using conversion electron Mössbauer spectrocopy (CEMS). They have performed short time (15–120 s) heat treatment at 600°C and compared the structure with materials which were heat treated for one hour. Their results indicate that crystallization occurs first at metallic glass ribbon surfaces and then proceeds into the bulk. Issues of surface crystallization are discussed further in

Section 4.3. Bitoh et al. [21] have investigated the additions of Ti, V, Cr, and Mn, substituted for Fe in NANOPERM alloys. These additions were observed to increase the primary crystallization temperature in the order Mn, Cr, V and Ti, respectively.

4.2.3. HITPERM alloys

Willard et al. [284,285] have used DSC to determine the temperatures of crystallization for an $Fe_{44}Co_{44}Zr_7B_4Cu_1$ alloy, as shown previously in Fig. 10. A two-stage crystallization was observed:

$$\text{Amorphous} \rightarrow \text{Amorphous}' + \alpha'\text{-FeCo}$$

$$\text{Amorphous}' + \alpha'\text{-FeCo} \rightarrow \alpha'\text{-FeCo} + (\text{Fe,Co})_3\text{Zr} \tag{27}$$

The primary and secondary crystallization temperatures occur at $T_{x1} = 510^\circ C$ and $T_{x2} = 700^\circ C$, for α'-FeCo and $(Fe,Co)_3Zr$, respectively. By having two distinct crystallization temperatures, the ferromagnetic α'-FeCo phase is allowed to form without the crystallization of non-ferromagnetic phases which can be deleterious to the soft magnetic properties.

Iwanabe et al. [134], have used DSC and TEM observations to determine the crystallization events in an $(Fe,Co)_{88}Hf_7B_4Cu$ alloy to be:

$$\text{Amorphous} \rightarrow \text{Amorphous}' + \alpha'\text{-FeCo}$$

$$\text{Amorphous}' + \alpha'\text{-FeCo} \rightarrow \alpha'\text{-FeCo} + (\text{Fe,Co})_2\text{Hf}$$

$$\alpha'\text{-FeCo} + (\text{Fe,Co})_2\text{Hf} + (\text{Fe,Co})_{23}\text{Hf}_6 \tag{28}$$

This represents the first such observation of the 23:6 phase as a nanocrystallization product.

4.2.4. Other alloys

Al-Haj et al. [4] have studied crystallization of $Fe_{83.5}Nb_7B_{8.5}Al_1$ and $Fe_{83.5}Nb_4B_{8.5}Al_1$ amorphous alloys by DTA, XRD and TEM. For the first of these alloys, the formation of an α-Fe amorphous nanophase was preceded by a crystallization event in which an α-NbB_2 intermetallic was observed. The second alloy underwent primary crystallization to α-Fe and amorphous phase followed by secondary crystallization of an intermetallic phase.

4.3. Surface crystallization kinetics

Surface crystallization of metallic glasses have been the subject of many studies (see, for example, [99,100]). Ayers et al. [8] have studied the morphology of surface crystallites on $Fe_{87}Zr_7B_5Cu_1$ alloys. These surface crystallites exhibit (200) texture. Annealing at temperatures between 623 and 773 K result in

nanocrystallization of randomly oriented BCC α-Fe and coarsening of the surface crystallites. Random orientations of the nanocrystallites which grew after surface crystallization was inferred from a more rapid growth of the (110) diffraction peaks as compared with the (200) peaks characteristic of the surface texture. Growth of the surface crystallites was accompanied by pronounced faceting that was observed by atomic force microscopy (AFM). The rapid coarsening of the surface crystallites suggested depletion of the amorphous phase at the surface. Scanning Auger microprobe analysis gave evidence of surface oxidation that may have influenced the surface crystallization kinetics.

Kopewicz and Grabias [161] Kopcewicz et al. [162] have used conversion electron emmission and γ-transmission Mössbauer spectroscopy to study the differences in bulk and surface crystallization of amorphous $Fe_{81}Zr_7B_{12}$ alloy precursors after 430, 500, 550, 600 and 780°C anneals. Surface crystallization was observed to begin at lower annealing temperatures and was attributed to boron depletion at the surface. Crystallites of phases not observed in the bulk were observed in the surface Mössbauer spectra. Kopcewicz et al. [161,162] have studied surface and bulk crystallization of amorphous $Fe_{81}Zr_7B_{12}$ and $Fe_{79}Zr_7B_{12}Cu_2$ alloys, using conversion electron emmission (CEMS) and γ-transmission Mössbauer spectroscopy. Again enhanced surface crystallization was attributed to boron depletion at the surface.

4.4. Crystallization kinetics

Table 5 summarizes the results of several experiments aimed at elucidating the crystallization kinetics in a variety of precursors to nanocrystalline alloys. The details of these experiments are discussed in the sections below. These experiments involve following the time dependence of a physical parameter, such as resistance, thermoelectric power, magnetization, etc. and relating these parameters to the volume fraction transformed of the crystalline phase. These data are then analyzed within the framework of a JMA or other kinetic rate law and an activation energy for crystallization is extracted.

4.4.1. FINEMET alloys

Allia et al. [5] have followed the kinetics of the nanocrystallization process in FINEMET using isothermal measurements of the time-dependence of the resistance, $R(t)$. The volume fraction transformed, X, of the nanocrystalline material was shown to be proportional to the change in electrical resistance. X was shown to obey JMA kinetics with an exponent $n \sim 4$ during the early stages of nanocrystallization. This was taken as suggesting homogeneous nucleation and 3D grain growth. At longer times, however power law kinetics with $X \sim At^{\alpha}$ (where α was independent of T) were observed. This is taken as a signature of reduction in the grain growth velocity at longer times.

Bigot et al. [19] have studied nanocrystallization of FINEMET alloys and observed a two step crystallization process. A JMA exponent of 1.5–2.0 and an activation energy of 4.3 eV was determined for the primary crystallization process.

The Curie temperature of the intergranular amorphous phase was determine from DTA scans. It was observed that T_C^{am} increased with increasing annealing temperature in the range from 480 to 630°C. T_{x1} for the as-quenched amorphous material was observed to be ~560°C. T_{x1} was observed to increase for samples annealed above 500°C, presumably due to the changing concentration of the amorphous phase.

Yavari and Drbohlav [288] have considered thermodynamic and kinetic conditions for nanocrystallization of Fe-based amorphous precursors. They conclude that nanocrystallization does not require Nb, Zr or Cu additions. A duplex microstructure in Fe-base hypoeutectic alloys is possible as long as α-Fe nanoparticles expel a component that acts to raise the crystallization temperature of the remaining amorphous phase.

Gonzalez et al. [70] have studied the influence of heating rate up to the crystallization temperature on effective anisotropies in FINEMET materials. Slow heating rates were observed to lead to greater completion of the crystallization process and stronger intergranular coupling., These slower heating rates therefore led to smaller effective magnetic anisotropies and better soft magnetic properties.

Yavari and Negri [289] have modified models of the nanocrystallization process of soft magnetic Fe-based amorphous alloys to consider the influence of experimentally measured concentration gradients of elements that are insoluble in the primary crystalline phase. The authors consider nanocrysallization of BCC Fe particles from hypoeutectic Fe-rich amorphous alloys such as FINEMET and NANOPERM. They convincingly show that in a JMA analysis of

Table 5
Summary of crystallization kinetics experiments on precursors to nanocrystalline alloys

Alloy	Kinetic analysis[a]	Reference	Activation energy (eV/atom)	JMA exponent	Experiment
FINEMET	JMA	[275]	3.58–3.93		TEP
FINEMET	JMA		3.84–4.08		HV
FINEMET	KP		3.7–4.5		DSC
FINEMET	JMA	[174]	3.33		
FINEMET	JMA	[50]	3.9–4.1		
FINEMET		[5]		$n = 4$	$R(t)$
FINEMET	KP	[39]	3.8		DSC
FINEMET	GW–JMA	[39]	3.8	$n = 1.3$	DSC
FINEMET	GW–JMA	[39]	3.4	$n = 1.3$	TMG
FINEMET	JMA	[19]	4.3	$n = 1.5$–2.0	TMG
$Fe_{92}Zr_8$		[262]		$n = 1.8$–1.9	DTA
$Fe_{92}Zr_8$		[262]		$n = 2.2$–2.3	DTA
$(Fe,Co)_{81}Ta_9C_{10}$	JMA	[88]	3.4	$n = 3.2$	$M(t)$

[a] JMA = Johnson–Mehl–Avrami, TEP = Thermoelectric power, $M(t)$ = Magnetization, TMG = Thermomagnetic gravimetry, DSC = Differential Scanning Calorimetry, KP = Kisslinger plot [149], GW = Gao–Wang [62,63], HV = Vickers hardness, $R(t)$ = Resistance, DTA = Differential Thermal Analysis.

nanocrystallization transformed volume fractions need to be corrected for the dependence of the enthalpy of primary crystallization on the concentration of the remaining amorphous phase as the transformation proceeds. They argue that the nucleation rate of the primary phase decreases quickly with time due to a reduction in driving force due to concentration variations in the amorphous matrix. The concentration gradients used in their model are based on field ion microscopy (FIM)-atom probe chemistry profiled as determined by Hono [118] and discussed in Section 6.

4.4.2. NANOPERM alloys

Suzuki et al. [262] have investigated crystallization kinetics in $Fe_{92}Zr_8$ and $Fe_{91}Zr_7B_2$ amorphous alloys. JMA analysis of DTA data revealed a JMA exponent $n = 1.8$–9 for $Fe_{92}Zr_8$ and $n = 2.2$–2.3 for $Fe_{91}Zr_7B_2$. Exponents greater than those expected for diffusion controlled growth after immediate nucleation (viz. $n = 3/2$) were explained by a size and morphology dependent growth rate.

Dahlgren et al. [45] have observed that in an $Fe_{86}Zr_7Cu_1B_6$ alloy, the volume fraction crystallized after 1 h increased from 70 to 75% to 90 to 95% for annealing temperatures of 550, 600, 650, and 700°C, respectively. These volume fractions were inferred from Mössbauer spectra. These results were compared with results of Joule heating experiments of different durations performed (5–100 s) and at different current levels (2.0–4.0 A). The temperature dependence of the coercivity, $H_c(T)$, was significantly larger for annealed as compared to Joule heated samples.

Hsiao and Turgut (Hsiao and Turgut, [205]) have examined crystallization kinetics in an $Fe_{88}Zr_7Cu_1B_4$ NANOPERM alloy using time-dependent magnetization measurements at the crystallization temperature. Since the crystallization temperature of this alloy exceeded the Curie temperature of the amorphous phase, these alloys initially have zero magnetization when they are heated to their crystallization temperature. As the alloy crystallizes, the magnetization is directly proportional to the volume fraction of the BCC α-Fe nanocrystallites. Thus the time dependence of the magnetization is a direct probe of the crystallization kinetics. Fig. 19 shows $M(t)$ normalized by the value of magnetization after one hour for crystallization of an $Fe_{88}Zr_7Cu_1B_4$ NANOPERM alloy at temperatures of 490, 500, 520 and 550°C, respectively [205]. An analysis of the time exponent and activation energy for crystallization has yet to be reported in the literature.

4.4.3. HITPERM alloys

No observations of crystallization kinetics in HITPERM alloys have yet been reported in the literature.

4.4.4. Other alloys

Crystallization kinetics in $(Fe, Co)_{81}Ta_9C_{10}$ thin films have been measured by monitoring the magnetization as a function of time during the crystallization process. As the moment reducing Ta and C elements are expelled to a grain

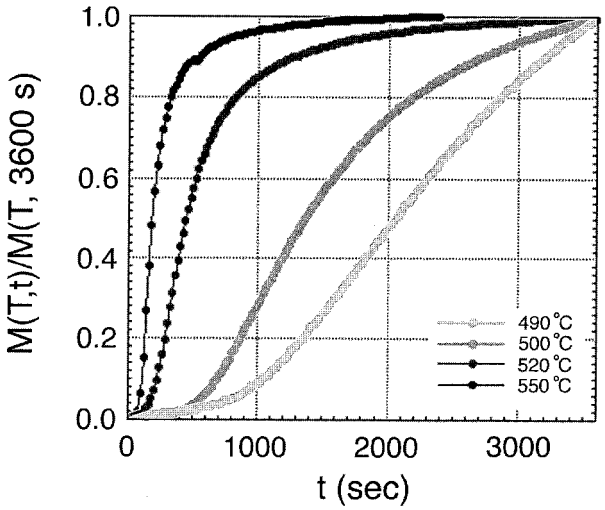

Fig. 19. Isothermal magnetization as a function of time (normalized by its value after 1 h) for the NANOPERM composition $Fe_{88}Zr_7B_4Cu$ at 490, 500, 520 and 550°C, respectively [205].

boundary phase during primary crystallization of α-Fe or α-FeCo the magnetization of the sample is observed to increase. The increase in magnetization can be taken as being proportional to the fraction of amorphous material that has crystallized. The fraction transformed has been shown to follow Johnson–Mehl–Avrami a (JMA) kinetics expression of the form of Eq. (19). Fits of $X(t)$ using a JMA kinetic equation with an exponent $n = 3.2$ were consistent with the data for Fe–Ta–C alloys. Analysis of the T-dependence of the rate constant yielded an activation energy for crystallization, Q_t, of 3.4 eV (see Fig. 20).

4.5. Ordering and structural phase transitions in nanocrystalline alloys

4.5.1. Nanoparticles and nanoencapsulates.

Fe–Co alloys undergo an order–disorder transformation at a maximum temperature of 730°C at the composition $Fe_{50}Co_{50}$, with a change in structure from the disordered α-BCC to the ordered β-CsCl-type structure (Fig. 21(a)). This order–disorder tranformation has been observed in C-coated Fe_xCo_{1-x} ($x = 0.50$, 0.45, 0.40, 0.35, 0.30, 0.25) nanoparticles produced using an RF plasma torch by Turgut et al. [271]. Structural determination by X-ray diffraction indicated a single disordered BCC α-FeCo phase along with graphitic C for all compositions. DTA and the temperature dependence of the magnetization revealed the effects of atomic ordering.

Fig. 21(b) illustrates $M(T)$, at $H = 500$ Oe, for equiatomic FeCo nanocrystalline powders measured on a second heating cycle after initial heating to 920°C. The influence of ordering is observed prominently in features that are quite similar to the thermomagnetic observations for bulk $Fe_{49}Co_{49}V_2$ alloys. These features

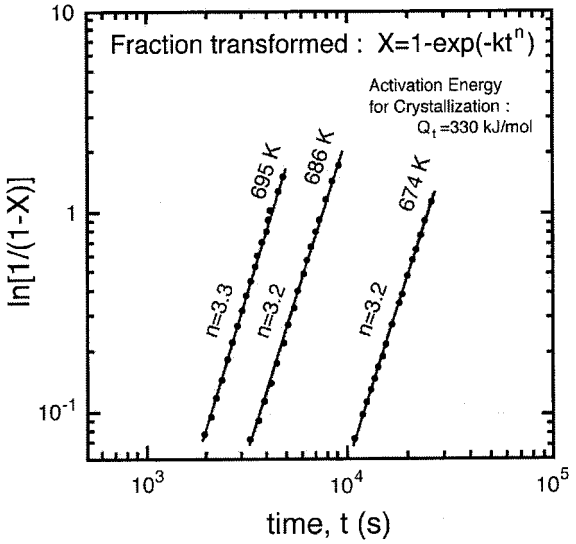

Fig. 20. JMA plots of crystallization of amorphous $Fe_{81.4}Ta_{8.3}C_{10.3}$ thin films. The activation energy was obtained from an Arrhenius plot of the time to 50% crystallization (reproduced with permission from Hasegawa et al. [88]).

include an increase in $M(T)$ at ~600°C (due to chemical ordering) and a return to the extrapolated low temperature branch of the curve at the disordering temperature of ~730°C. Also of note is that at ~950°C, we observe an abrupt drop in the magnetization that corresponds to the $\alpha \rightarrow \gamma$ structural phase transformation. A prominent Curie tail is observed above this transformation temperature indicating paramagnetic response. It can be concluded from the abruptness in the drop of $M(T)$ that the $Fe_{0.5}Co_{0.5}$ alloy has a Curie temperature that exceeds the $\alpha \rightarrow \gamma$ phase transformation temperature. Thus a true Curie temperature is not observed, instead it is concluded that (ferro)magnetic α-$Fe_{0.5}Co_{0.5}$ transforms to non(para)-magnetic γ-$Fe_{0.5}Co_{0.5}$. This is corroborated in the DTA data, where the order–disorder and $\alpha \rightarrow \gamma$ phase transformations have also been clearly observed as illustrated in Fig. 22. This DTA data shows the (a) $\alpha \rightarrow \gamma$ and (b) order–disorder phase transitions.

Fig. 23(a) shows thermomagnetic data (4°C/min) at $H = 500$ Oe for Fe_xCo_{1-x}[C] alloy nanoparticles. DTA results in the work of Turgut et al. [271] demonstrated that the peak in the heating branch corresponds to reordering. The contribution of reordering to an increase in magnetization was inferred. Fig. 23(b) shows high field thermomagnetic data for Fe_xCo_{1-x}[C] alloy nanocrystals ($H = 10$ kOe, 2°C/min). No compositional dependence of the reordering temperature was observed for the saturation magnetization. A '550°C anomaly' was observed that occurs as a decrease in saturation magnetization with increasing temperatures up to 510°C.

The $Fe_{70}Co_{30}$ composition exhibits only a very small anomaly in agreement with the data of Velisek et al. [277]. They showed that while the $Fe_{50}Co_{50}$

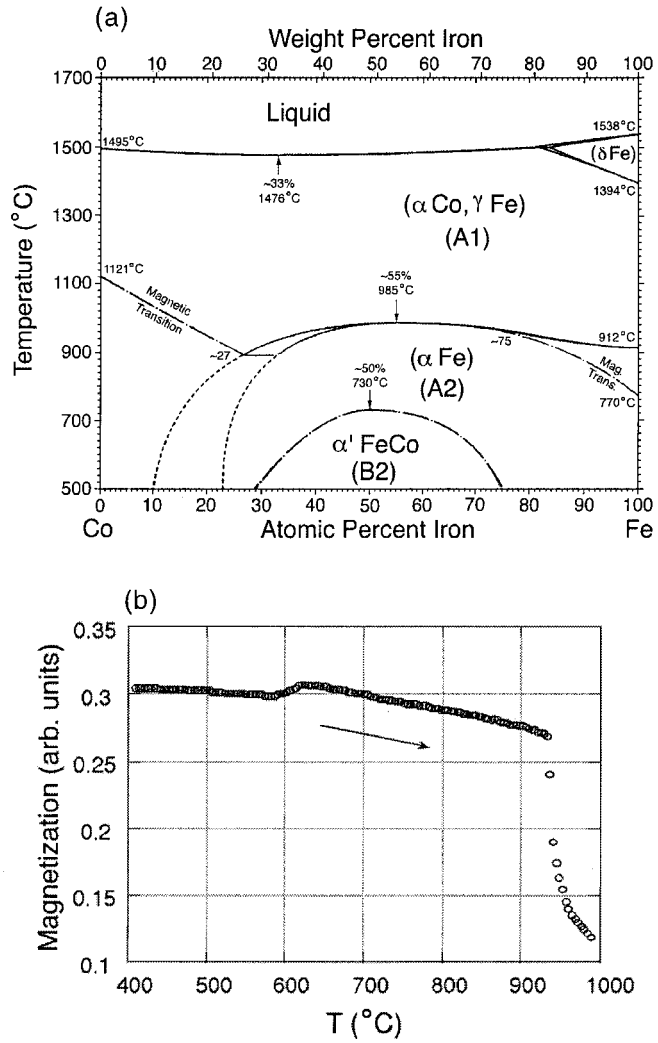

Fig. 21. (a) Fe–Co phase diagram [197] and (b) $M(T)$ data for C-arc synthesized equiatomic Fe–Co nanoparticles measured using a Lakeshore model 7300 VSM and oven assembly at 500 Oe measured on a second heating cycle to 995°C after initial heating to 920°C.

composition shows the 550°C anomaly accompanied with a change in specific heat, an Fe_3Co composition showed only a small anomaly. In nanocrystalline materials the anomaly occurs at temperatures well below 550°C which has been attributed to the high diffusivity in these particles which aids reordering.

4.5.2. FINEMET alloys

Müller et al. [210] studied the structure and the magnetic properties of

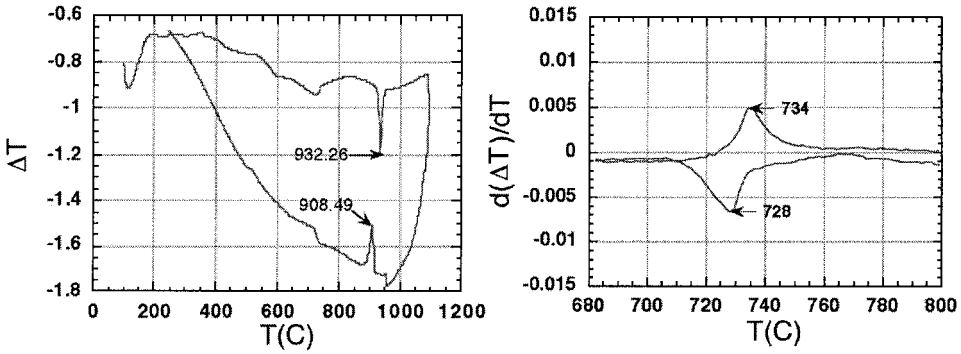

Fig. 22. DTA analysis of the same material descibed in Fig. 21 showing (a) $\alpha \rightarrow \gamma$ and (b) order–disorder phase transitions [271].

amorphous FeSiBCuNb (FINEMET) alloys. Annealing at ~500°C lead to nanocrystallization of an Fe(Si) phase. In alloys with a Si content < 12 at% an Fe–Si solid solution in BCC Fe was observed. Alloys with Si > 12 at% crystallized in the ordered $D0_3$ superstructure.

Zhang et al. [301] have studied ordering phenomena in nanocrystalline α-Fe(Si) particles which were the products of crystallizing FINEMET amorphous precursors by XRD. They observed that for materials heated for 1 h at 490°C, α-Fe(Si) nanocrystals contained disordered regions and ordered regions with the $D0_3$ crystal structure consistent with a first order thermodynamic transition (BCC $\rightarrow$ $D0_3$). For treatments between 490–590°C the degree of order increased progressively. Nearly all of the particles were completely of the $D0_3$ crystal structure for treatments of 590°C. With increasing annealing temperature the shape of the $D0_3$ regions changed from spheroidal to spherical.

Zhu et al. [305] have used neutron diffraction to study nanocrystallization process of $Fe_{73.5}Si_{22.5-x}B_xCu_1Nb_3$ ($x = 5$, 9, and 12) alloys. The amount of ordering in the $D0_3$ Fe(Si) crystals was observed to increase with the Si concentration. Results for the volume fraction of the $D0_3$ phase were analyzed in terms of a time temperature transformation (TTT) curve for ordering.

4.5.3. NANOPERM alloys

The nanocrystallization process of NANOPERM alloys results in BCC α-Fe nanocrystals result. No ordering phenomena are expected for these nanocrystalline phases.

4.5.4. HITPERM alloys

The synchrotron X-ray diffraction data of Willard et al. [284] described in Section 5.2.3, with a radiation wavelength chosen to take advantage of anomalous scattering, unambiguously identifies the atomically ordered α′-FeCo phase in a $Fe_{44}Co_{44}Zr_7B_4Cu_1$ HITPERM alloy. No analysis has yet been published which

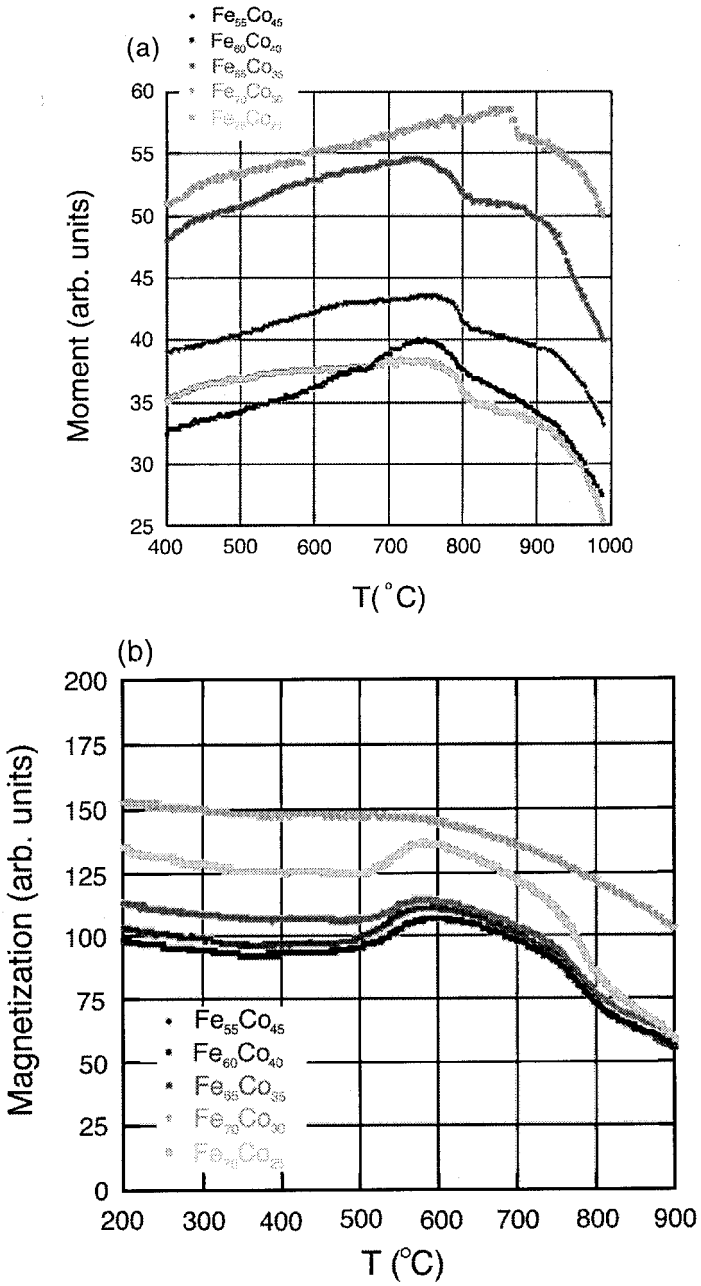

Fig. 23. (a) Magnetization versus temperature data, showing ordering anomalies, taken at 500 Oe and 4°C/min. heating rate for various Fe_xCo_{1-x}[C] nanoparticles. (b) Same response taken at 1 T and 2°C/min heating rate [271].

determines the relative fraction of ordered and disordered (α- and α′-FeCo) in these materials.

5. Structure and microstructure of amorphous and nanocrystalline alloys

An amorphous solid is one in which the atomic positions do not have crystalline periodic (or quasicrystalline) order. The amorphous structure is postulated to be that of the frozen liquid. The local structure in amorphous metallic materials is distinct from that of window glass, for example, which is described in terms of random covalent networks of SiO_4 tetrahedra. Instead amorphous metals are often described as being nearly topologically close packed or possessing coordination polyhedra similar to those of the stable crystalline phases of similar composition. Models of the short range correlations in amorphous alloys include the dense random packing of hard spheres (DRPHS) models [14,15] the microcrystalline and local icosahedral short range order models as well as models of chemical short range order in amorphous alloys.

Nanocrystalline alloys possess crystalline structure but finite size effects will alter the scattering of X-rays from the crystallites, giving rise to Scherrer broadening of the XRD peaks. In many of the nanocrystalline alloys that are discussed here a two-phase microstructure is apparent. The structure and chemistry of the two-phase and interfacial structure are important in determining properties. When classifying amorphous and nanocrystalline alloys, we might consider looking at the short-range order, long-range order, and the length scales over which we expect to find these types of ordering (see Table 6). These classifications are borrowed in part from O'Handley [220].

5.1. Background information

5.1.1. Amorphous alloys

Since periodically spaced parallel planes of atoms do not exist in amorphous alloys, X-ray diffraction is not possible. On the other hand, if one performs an X-ray scattering experiment on an amorphous material, one does observe one or more broad peaks in the scattered intensity (Fig. 24) at angles similar to those where one or more diffraction peaks would occur in a crystalline alloy of the same composition. The *d*-spacing which would be calculated for this peak (naively employing a Bragg's law) would correspond to the closest spacing of planes in a touching atomic sphere model (e.g. like the dense random packing of hard spheres (DRPHS) model discussed below). This can be shown [77] to be $d \sim 0.815D$, where d is the calculated spacing and D is the atomic diameter (in a single component system). If one also naively used a Scherrer analysis of the breadth of the X-ray scattering peak(s) one would conclude that the 'crystallite size' was on the order of atomic dimensions. This is a good argument for only short-range atomic correlations being present in amorphous metals. Analysis of such scattering peaks offers a powerful tool for probing short-range order in amorphous solids.

Scattering experiments on amorphous alloys can be used to determine the so-called *radial distribution function* that is derived from an appropriate Fourier transform of a normalized scattered intensity expressed as a function of scattering angle (or k). Much of the structural information as to atomic configurations in amorphous solids comes from determination of the radial distribution function or a species specific radial distribution function as can be obtained from an EXAFS measurement. This information can then be used to test the validity of structural models of the short-range correlations in amorphous alloys. These scattering experiments provide unique challenges and have been aided by the development of high intensity X-ray sources now available, for example, at synchrotron reactors.

The atoms in an amorphous solid are not periodically arranged and therefore the concept of a lattice is not appropriate for describing their positions. Thus in an amorphous solid there is not an equivalent concept to that of a lattice and a basis we must resign ourselves to describe atomic positions in a more probabilistic sense using the concept of a pair correlation function, $g(r)$. The pair correlation function is defined as the probability that two atoms in the structure are separated by a distance, r. To define $g(r)$ further we begin by considering N atoms in a volume, Ω, letting $R_1, R_2, \ldots, R_N$ denote the positions of the N atoms with respect to an arbitrary origin. The distance r denotes the magnitude of the vector connecting two atoms i and j, i.e. $r = R_i - R_j$. Two additional atomic distribution functions related to the pair correlation function are the spatially dependent atomic density, $\rho(r)$, that is defined as: $\rho(r) = Ng(r)/\Omega$ and the radial distribution function, RDF(r), which is defined in terms of the pair correlation function as: $\mathrm{RDF}(r) = 4\pi r^2 \rho(r)$

We can learn about radial distribution functions and consequently pair correlation functions through scattering experiments, where the wavelength of the scattered radiation is on the order of nearest neighbor atomic distances. We will consider X-ray scattering from amorphous solids in the next section. Fig. 24 illustrates schematically the distinction between the pair correlation functions for a completely disordered, a (crystalline) completely ordered and an (amorphous) short range ordered material. A completely disordered material, like a gas has a uniform unit probability of finding neighboring atoms at all possible distances which leads to a uniform, featureless $g(r)$. On the other hand, a crystalline solid

Table 6
Classification of materials by range and type of atomic order [220]

SRO	Range of SRO	LRO	Range of LRO	Material classification
Crystalline	> 10 μm	Crystalline	> 10 μm	Macrocrystal
Crystalline	> 100 nm < 10 μm	Crystalline	> 100 nm	Microcrystal
Crystalline	< 100 nm	Crystalline	< 100 nm	Nanocrystalline
Near crystalline	~ 1 nm	No LRO		Amorphous I
Non crystalline	~ 1 nm	No LRO		Amorphous II
Non crystalline		Quasiperiodic	~ 1 μm	Quasicrystal

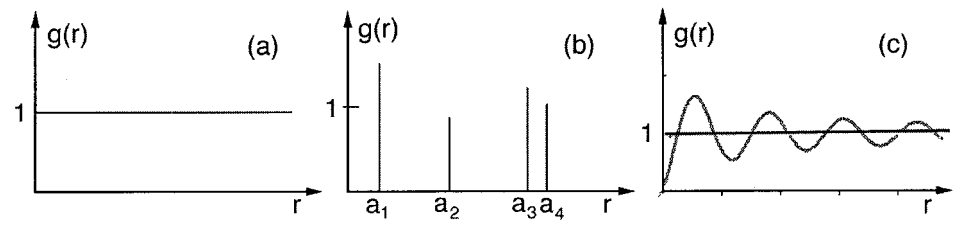

Fig. 24. Typical pair correlation functions for a completely disordered (a), a (crystalline) completely ordered (b) and an (amorphous) short-range ordered (c) material.

has a set of discrete distances between atomic positions and therefore the pair correlation function is a set of discrete δ-like functions, the amplitude of which reflects the particular coordination number for nearest neighbor, next nearest neighbor,... etc. pairs of atoms. This is consistent with Bragg scattering (diffraction). In amorphous alloys $g(r)$ is neither discrete or featureless, instead broad peaks reflect the short-range order in these materials

5.1.2. Nanocrystalline phases

Nanocrystalline alloys are above all crystalline and because of their crystallinity exhibit Bragg scattering peaks in X-ray diffraction experiments. However, due to their small size, significant fine particle broadening is observed in the Bragg peaks. The condition for constructive reinforcement of X-ray scattering from a crystalline solid is given by Bragg's Law:

$$n\lambda = 2d \sin\theta \tag{29}$$

This equates the path difference of X-rays scattered from parallel crystalline planes spaced $d = d_{hkl}$ apart to an integral (n) number of X-ray wavelengths λ. Here θ is the X-ray angle of incidence (and of diffraction) measured with respect to the crystalline planes. For an infinite crystal Bragg scattering occurs at discrete values of 2θ satisfying the Bragg condition, i.e. Bragg peaks are δ- functions. For finite sized crystals (Fig. 25) the peaks are broadened over a range of angles.

To better understand the phenomenon of fine particle broadening (following the arguments of Cullity [44]) we consider a finite crystal of thickness, $t = md$, where m is an integer, and d is the distance between crystalline planes, i.e., there are m planes in t. Considering Fig. 25, if the broadened Bragg peak begins at an angle $2\theta_2$ and ends at $2\theta_1$, the breadth of the peak (or full width at half maximum) is given as:

$$B_\Theta = \frac{1}{2}(2\theta_1 - 2\theta_2) = \theta_1 - \theta_2 \tag{30}$$

Now consider the path differences for each of the two angles θ_1 and θ_2, for X-rays travelling the full thickness of the crystal:

$$(m+1)\lambda = 2t \sin\theta_1 \tag{31}$$

$$(m-1)\lambda = 2t \sin\theta_2 \tag{32}$$

and by subtraction:

$$t(\sin\theta_1 - \sin\theta_2) = \lambda$$

$$= 2t\cos\left(\frac{\theta_1+\theta_2}{2}\right)\sin\left(\frac{\theta_1-\theta_2}{2}\right) \tag{33}$$

Now $\theta_1 + \theta_2 \sim 2\theta_B$ and $\sin((\theta_1-\theta_2)/2) \sim (\theta_1-\theta_2)/2$ so that:

$$t = \frac{\lambda}{B_\Theta \cos\theta_B} \tag{34}$$

A more exact empirical treatment yields:

$$t = \frac{0.9\lambda}{B_\Theta \cos\theta_B} \tag{35}$$

which is known as the Scherrer formula. It states that for a crystal of thickness, t, we should expect a particle broadening of B of the Bragg peak at $2\theta_B$. For 50 nm particles an $\sim 0.20^\circ$ broadening is expected which is easily measured.

5.1.3. Microstructural characterization and spectroscopic analysis (amorphous and nanocrystalline alloys)

State of the art microstructural characterization techniques have been used to understand the relationship between structure and properties in free standing

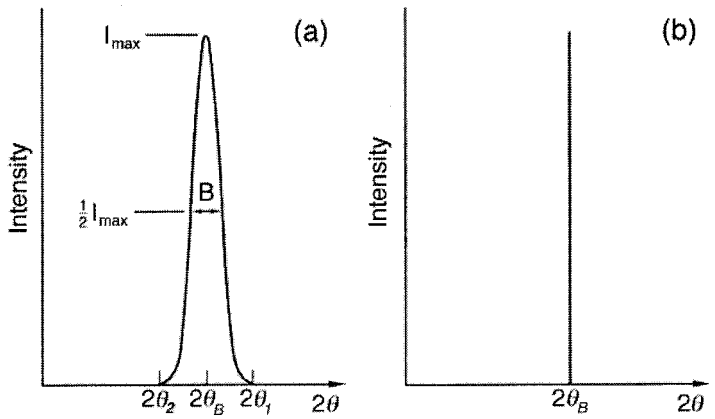

Fig. 25. Illustration of the effect of fine particle broadening in XRD (a) fine particles and (b) perfect crystal. [adapted from Cullity [44].

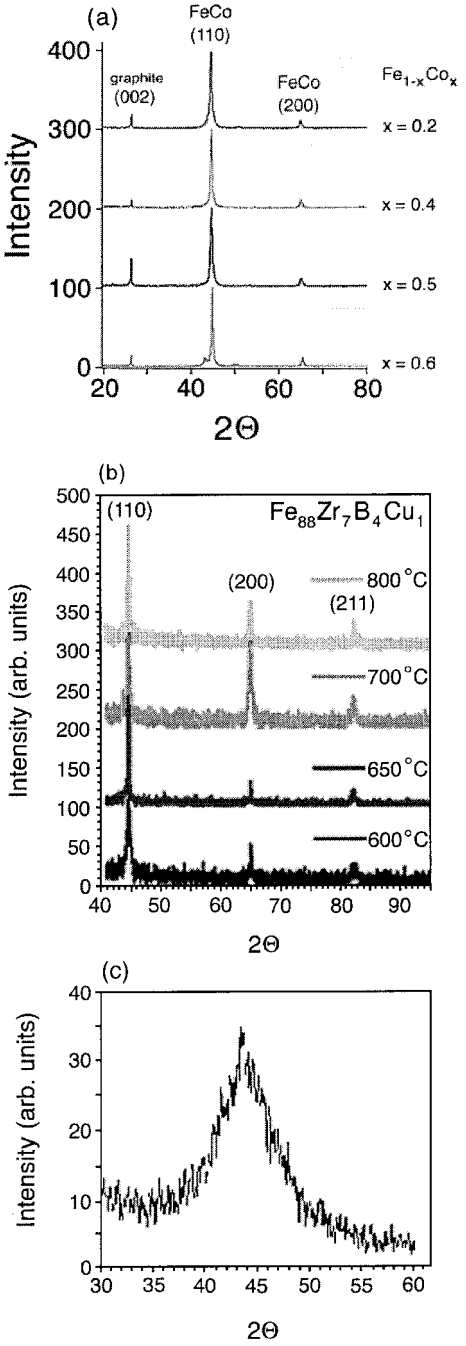

Fig. 26. X-ray diffraction determination of structure of nanocrystalline solids (a) C-coated FeCo nanoparticles [60], (b) Fe nanocrystalline ribbon [284] crystallized from (c) an FeZrBCu amorphous phase.

(powder) magnetic nanocrystals and nanocrystalline compacts. In particular, TEM is used to characterize the coating, size, and size distribution, and electron diffraction (ED) to determine the phases present in the powder sample. Energy Dispersive X-ray Fluorescence Spectroscopy (EDS) can be used to ascertain the distribution of elements.

Of particular importance is the issue of chemical homogeneity in alloy nanoparticles. Here energy filtered microscopy (EFM), scanning transmission electron microscopy (STEM), and parallel electron energy loss spectroscopy (PEELS) enable probes of chemistry on a nanometer size scale. PEELS complements the elemental mapping capability of EFM. PEELS enables quantitative analysis on a 1–2 nm scale that is critical to phase identification in complex alloy systems. Energy resolution of STEM based PEELS is superior to the EFM (0.1 vs. 5 eV energy resolution, respectively). The fine structure of the core shell transitions can reveal the type of bonding of Fe atoms at the grain boundaries, for example. Combination of high brightness with a field emission source and reduced sample drift improves signal to noise ratios and make it possible to study the spatial distribution of low abundance and light mass elements (e.g. B). Lorentz microscopy is a particularly useful technique in magnetic domain imaging. Atom probe field ion microscopy (APFIM) has been used, primarily by Hono, in the study of the chemistry of nanocrystalline materials with high spatial resolution [116–118].

Scanning tunneling (STM) and atomic force (AFM) microscopies are used to probe microstructure with atomic resolution. Magnetic force microscopy (MFM) allows for the study of magnetic domains with similar resolution. A variety of other optical techniques are useful in domain imaging. These include Nomarski filtered microscopy, light microscopy of ferrofluid decorated samples, magneto-optic Kerr effect (MOKE), etc.

The Mössbauer effect refers to the recoil free gamma ray resonance absorption. This is the basis for Mössbauer spectroscopy which is commonly used as a probe of local environments and magnetic structure in solids. The Mössbauer effect involves the decay of a nucleus from an excited state to its ground state with the emission of a γ-ray. In a solid the whole lattice takes up the recoil energy required for momentum conservation. The large mass of the lattice means that the recoil energy ($p^2/2m$) is negligible and the γ-ray energy is precisely the difference in energy between the excited and ground states of the emitting nuclei. An emitted γ-ray can in turn be absorbed to pump a nuclei into it's exited state; where after a mean lifetime τ it will fall back into the ground state re-emitting the γ-ray isotropically. This γ-ray resonance fluorescence is used as a spectroscopic tool when the emitted γ-ray energy is modulated by a Doppler shift associated with the harmonic motion (relative velocity) of the γ-ray source and the emitting nuclei. This Doppler energy shift is given by $E = (v/c)E_\gamma$, where v is the source velocity, c is the speed of light and E_γ is the γ-ray energy.

A Mössbauer spectra [91] consists of the γ-ray intensity measured at a γ-ray detector and collected as a function of the source/absorber relative velocity (and therefore modulation energy, E). A resonance occurs for $E = \Gamma = h/2\pi\tau$, where τ

is again the mean life time of the excited state. For example, for an ^{57}Fe (Mössbauer active) nucleus Γ is 4.6×10^{-12} keV. Fig. 27(a) shows a typical unsplit Mössbauer resonance line characterized by a position, δ, a line width, Γ, and area $A = c\varepsilon\Gamma$. Mössbauer spectra are useful in obtaining chemical and field signatures because of their splittings in the same. A Mössbauer active nuclei in a non-cubic environment is subject to a quadrupole splitting, Δ, which is proportional to the electric field gradient at the nucleus resulting from the chemical environment of the nuclei (Fig. 27(b)). For a magnetic environment the hyperfine field, H_0, will also split the Mössbauer signal into a hextet (Fig. 27(c)).

In Mössbauer spectroscopy the local environment of the target ions is probed by γ-rays emitted from a Mössbauer source. The quadrupole splitting of the eventual reemission by the target ions of these γ-rays is determined by the symmetry of the electric field gradient at the nucleus. Because the electric field gradient transforms like a vector quantity, Mössbauer spectroscopy can distinguish asymmetries with respect to the $\ell = 1$ basis functions x, y and z. The experimental variable which describes the symmetry is the quadrupole splitting Δ which describes the extent to which a single Mössbauer peak splits as a result of an asymmetric electric field gradient. Because of the fact that this gradient transforms like a vector it is impossible to distinguish between symmetries in which the x, y, and z basis functions remain degenerate. Thus, a single unsplit Mössbauer line, is indicative of a high symmetry but cannot distinguish between tetrahedral, octahedral, and icosahedral symmetries.

Recently, RF Mössbauer techniques have been used to probe magnetic anisotropy in amorphous and nanocrystalline materials. The RF collapse of Mössbauer sidebands as a function of superimposed RF field amplitude is becoming a powerful tool for probing local anisotopies. This technique is discussed in further detail below.

5.2. Experimental observations: X-ray scattering and EXAFS

A key tool in both the routine characterization and the in depth study of nanocrystalline materials has been X-ray diffraction techniques. Several examples

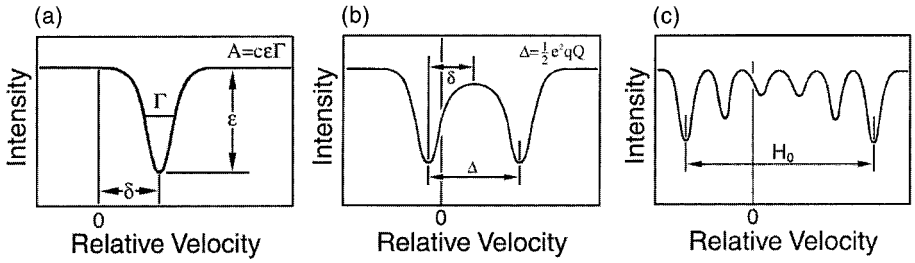

Fig. 27. Mössbauer spectroscopy resonance phenomena including (a) resonance peak, (b) quadrupole splitting of the resonance peak and (c) hyperfine field splitting of the resonance peak.

of the utility of this technique are illustrated in Fig. 26. In particular, XRD is used to identify crystalline phases in nanocrystalline materials. Fig. 26(a) shows XRD identification of the BCC FeCo phase, and C in C-arc synthesized FeCo nanoparticles. Scherrer analysis of the width of diffraction peaks is a useful tool for estimating particle sizes as discussed above. Fig. 26(b) shows the a single broad peak characteristic of the X-ray scattering intensity in an amorphous $Fe_{88}Zr_7B_4Cu$ alloy produced by melt spinning and the BCC peaks of α-Fe after the alloy has been crystallized at various temperatures.

Small-angle X-ray scattering experiments (SAXS) can also provide microstructural information in amorphous and nanocrystalline materials (Fig. 28). For example, Kopcewicz et al. [161] collected scattered intensity for a range of scattering vectors between $q = 0.1$ and 6 nm^{-1}. This range of q's allow for the detection of electron density fluctuations within a range of 30 to 1 nm in size and thus can probe the microstructural fluctuations in many nanocrystalline alloys. As illustrated in Fig. 28 [161–164] annealing of an initially amorphous NANOPERM composition results in structure in the SAXS intensity at low momentum transfer, q (typically with a A/q^3 form) which is related to electron density fluctuations on a greater than 20 nm scale. Additional structure near $q = 2$ nm^{-1} is seen to develop with increased annealing temperature and Cu content in these alloys. Shoulders in the data are attributed to interparticle interference effects in the precipitating alloy.

Extended X-ray absorption fine structure (EXAFS) is an advanced X-ray scattering technique that uses the fine structure associated with an X-ray absorption event to learn about the type, number and coordination of atoms

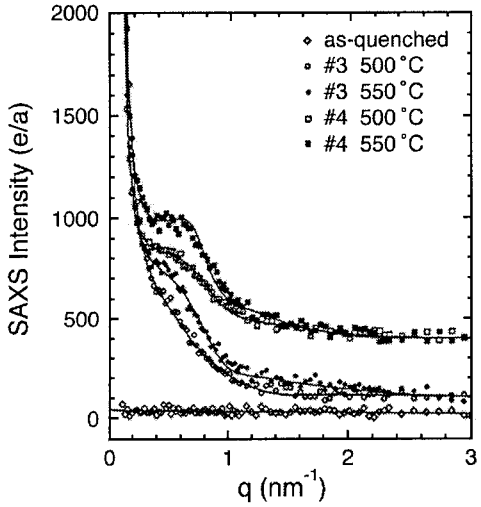

Fig. 28. SAXS data for as-quenched and annealed NANOPERM samples of composition $Fe_{85}Zr_7B_8$ and $Fe_{83}Zr_7B_8Cu_2$ [161,162].

about the atomic site(s) responsible for the absorbtion event. The typical cause of absorption of X-radiation in solids is the X-ray photoelectric effect in which the X-ray is responsible for an electronic excitation on the absorber atom (Fig. 29). Absorption processes lead to loss in X-ray intensity. This loss of intensity can be written in terms of Beer's law:

$$\frac{I}{I_0} = \exp\left[-(\mu_x/\rho)z\right] \tag{36}$$

where I and I_0 are the transmitted (through a thickness, z) and the incident intensity of the X-rays and μ_x/ρ is a mass absorption coefficient for X-rays (ρ is density).

The sequence of events that lead to the observed fine structure in the absorption spectrum are as follows:

1. X-rays of appropriate energy are absorbed at an atomic site, A, giving rise to a core level transition, e.g. a K_α transition. The energy for which this transition can be excited is atom species specific.
2. The excited photoelectron leaves a site A as a spherical wavefront. By the time it reaches site B, however, to good approximation it can be treated as a plane wave.
3. The photoelectron plane wave is backscattered from the nearest neighbor B sites and travels back to the original A site.
4. The outgoing photoelectron wavefront and the backscattered wavefront will have constructive and destructive interference effects that will modulate the transition probability of the absorption event. This electron wavefront carries information as to the local (typically first few coordination shells) environment around the absorbing atom.

As a result of the interference effects between the forward scattered and back-scattered waves, the amount of X-radiation absorbed will be modulated. This manifests itself in an oscillation in the X-ray intensity as a function of the X-ray

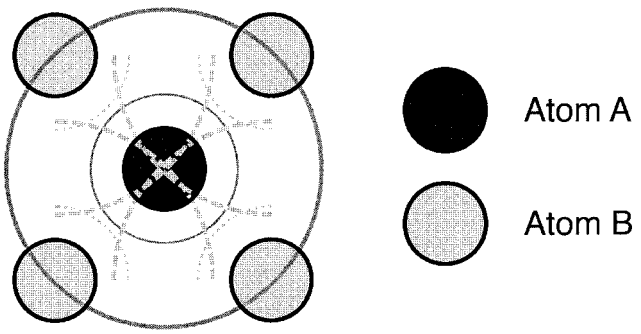

Fig. 29. EXAFS single scattering approximation geometry.

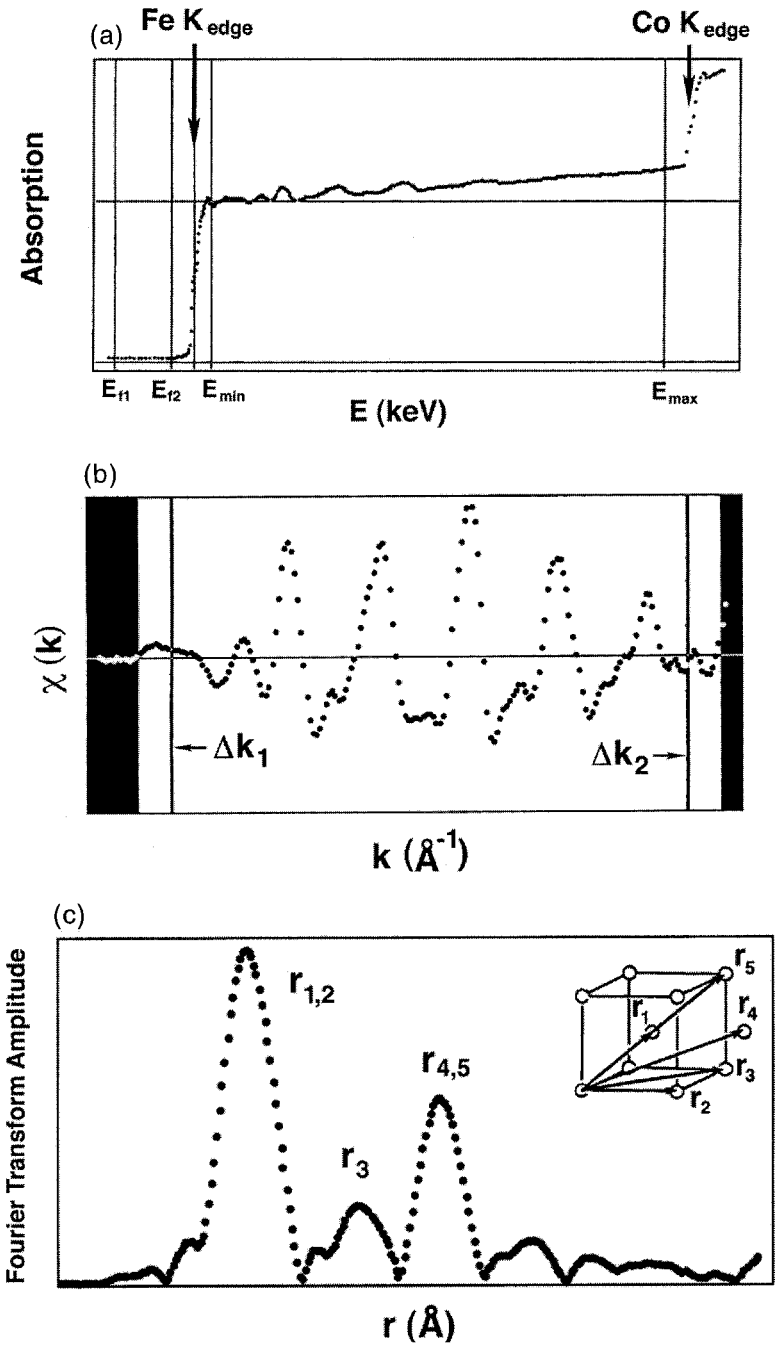

Fig. 30. An example of EXAFS data and it's reduction (Willard and Harris [309]) showing (a) the fine structure near the Fe K edge, (b) the function $\chi(k)$ and (c) the radial distribution function, about the Fe site for a nanocrystalline HITPERM material. The radial distribution function is consistent with a BCC-like crystalline environment in this nanocrystalline material.

energy for energies exceeding the absorption threshold. Analysis of the fine structure to reveal structural information is accomplished in several steps:

1. The absorption coefficient, $\mu(k)$, is determined as a function of the magnitude of the wavevector, k.
2. The monotonically decreasing absorption coefficient background is subtracted to yield only the oscillatory part that carries the information as to the type, number and distance of nearest neighbor scatterers. The function $\chi(k) = (\mu(k) - \mu_0(k))$, is constructed where $\mu_0(k)$ is the non-oscillatory part of the absorption coefficient.
3. The Fourier transform of the function $k\chi(k)$ results in a (site-specific) radial distribution function about the absorbing atom site.

This RDF is used within the *EXAFS single scattering approximation* to determine structural information. An example of EXAFS data and its reduction are shown in Fig. 30 (Willard et al., [309]) showing the fine structure near the Fe K edge for nanocrystalline HITPERM material. A radial distribution function, about the Fe site, is consistent with a BCC-like crystalline environment in this nanocrystalline material.

5.2.1. FINEMET alloys

The EXAFS technique has been successfully used to support the role of Cu as nucleation sites in the nanocrystallization process in FINEMET alloys. Early papers by Yoshizawa et al. [290,291,294] cited the reduction of the crystallization temperature of the α-FeSi phase due to the Cu addition, but failed to show direct evidence of their hypothesis that the Cu provided heterogeneous nucleation sites. Later, Hono et al. [116] showed by atom probe field ion microscopy that Cu clusters formed in these alloys at very short annealing times (as discussed below), and concluded that the Fe-based nanocrystals formed in the regions away from the Cu-rich clusters. Although this technique started to show the early development of the nanocrystalline microstructure, the probe of the local short-range order of the Cu-rich nanoparticles was only possible with the EXAFS technique.

EXAFS was first used by Kim et al. [145] to discover that the Cu-rich particles were FCC and formed at temperatures much lower than the crystallization of the α-FeSi phase. Another effort by Ayers et al. [9] showed the formation of the Cu-rich phase during the early stages of the heat treatment and evidence of FCC Cu formation in the as spun alloy. These studies were followed by a set of experiments performed by Ayers et al. [10] that led to the development of a model for the formation of the nanocrystalline microstructure in the FINEMET alloys.

This work by Ayers showed that even in the as cast material, the formation of Cu clusters of the size of a single FCC unit cell formed. As the samples were annealed, the growth of the Cu clusters and the formation of new clusters happened in the early stages of annealing (less than 8 min). When compared to an alloy without Nb ($Fe_{76.5}Si_{13.5}B_9Cu_1$), the FINEMET alloy formed considerably

smaller clusters. The $Fe_{76.5}Si_{13.5}B_9Cu_1$ alloy was seen to have no FCC Cu formation in the as cast state, but rapid formation of large Cu clusters.

These EXAFS data were used to form a model of the crystallization reaction for formation of the optimum FINEMET microstructure. From the melt spinning process, an amorphous alloy with tiny copper clustering is produced. In the early stages of annealing at an optimum temperature, new Cu-rich clusters are formed, as well as the growth of existing copper clusters, and the growth of α-FeSi using the FCC Cu-rich nanograins as heterogeneous nucleation sites. The concept of heterogeneous nucleation of α-FeSi on the Cu-rich clusters is based on the minimization of the interfacial energy [234]. Finally, the growth of α-FeSi continues and Cu clusters not used as nucleation sites grow to larger sizes (~5 nm).

Matsuura et al. [200] have used EXAFS at the Ga and Nb K-edges to examine the structure of $Fe_{73}Ga_4Nb_3Si_{11}B_9$ alloys after annealing to investigate the roles of Nb and Ga in the nanocrystallization process. Unlike Cu, in the $Fe_{73.5}Cu_1NB_3Si_{13.5}B_9$ FINEMET alloy, preferential Ga segregation could be inferred. EXAFS for alloys heat treated above the primary crystallization temperature, T_{x1} revealed Ga substitution on BCC Fe sites.

5.2.2. NANOPERM alloys

Kopcewicz et al. [163,164] have determined α-Fe nanocrystal sizes in $Fe_{93-x-y}Zr_7B_xCu_y$ ($x = 4$, 6, 8, 12, and $y = 0$ or 2) alloys nanocrystalized between 500 and 650°C, using conventional XRD and SAXS. Conventional XRD revealed a nanocrystal size of 5–14 nm as determined by Scherrer analysis. SAXS analysis revealed grain sizes of 3–7 nm, consistently a factor of 2 smaller than that determined by XRD. Since SAXS probes the entire sample volume and XRD the near surface regions it was inferred that the surface grains are significantly larger than the bulk. Features of the SAXS data are described above.

5.2.3. HITPERM alloys

The ambiguity in the determination of the α-FeCo or α′-FeCo phases above T_{x1} in conventional X-ray analysis, is due to the similarity of the atomic scattering factors of Fe and Co. This makes the observation of superlattice reflections in conventional XRD difficult, since the structure factor for superlattice reflections is related to the differences of the two atomic scattering factors. However, by using the intense beam of the synchrotron X-ray source and choosing the radiation wavelength to take advantage of anomalous scattering, Willard et al. [265,266] increased the difference in atomic scattering factors allowing for observation of superlattice reflections.

Synchrotron X-ray diffraction experiments, performed at the National Synchrotron Light Source on a nanocrystalline (HITPERM) $Fe_{44}Co_{44}Zr_7B_4Cu_1$ alloy by Willard et al. [284] have been used to identify the superlattice reflections which are signatures of the ordered α′-FeCo phase. X-rays with energies of 7112 eV or equivalently a wavelength of 1.748 Å were chosen to take advantage of the anomalous scattering between the Co and Fe K_α edges. Synchrotron X-ray

diffraction data has allowed for the distinction between HITPERM, with the B2 structure for the nanocrystallites, in contrast with nanocrystals in FINEMET, with the DO_3 structure, and NANOPERM, with the A2 structure. In Fig. 31, the synchrotron XRD pattern shows that the atomically ordered α'-FeCo phase has indeed been formed by the presence of the (100) superlattice reflection. This sample was heated at 550°C, that is below the temperature of the bulk orderdisorder phase transformation, so that in equilibrium the ordered phase is expected.

5.3. Experimental observations: neutron scattering

5.3.1. Nanoparticle powders

Neutron powder diffraction was used by Scott et al. [246] to study the order–disorder transformation in carbon-coated Fe_xCo_{1-x} nanoparticles produced using a RF plasma torch. Bulk equiatomic FeCo undergoes the same order–disorder transformation near 1000 K, passing from an ordered B2 (CsCl) structure to a disordered BCC solid solution on heating [251]. Apparently the high cooling rates in the plasma ($10^4 \rightarrow 10^6$ K/s) allow retention of the metastable disordered state. Analytical electron microscopy was used to characterize the morphology, composition, and chemical heterogeneity of the nanoparticles. High-resolution neutron powder diffraction was used to study their structure, crystallinity, and degree of order. Rietveld refinement of neutron powder patterns at 300, 673, 773, 983, 1013, and 1073 K allowed for the extraction of quantitative information about the order–disorder transformation in the nanoparticles. On heating, the nanoparticles were observed relax to their equilibrium ordered state above 773 K,

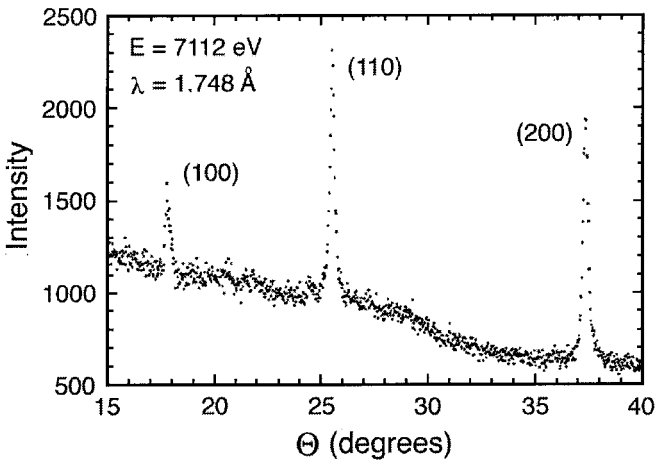

Fig. 31. Synchrotron XRD data for HITPERM alloys showing superlattice ordering peak for FeCo [284,285].

then disorder again above the 1000 K bulk transition temperature, in agreement with previous magnetic evidence of Turgut et al. [272].

5.3.2. Nanocrystalline materials

Small angle neutron scattering (SANS) has been used as a technique for evaluating the size of nanocrystallites. It has been used in combination with TEM to study BCC α-Fe nanocrystals embedded in larger boride crystals in the products of crystallization of an $Fe_{80}B_{20}$ metallic glass [47]. It has also been used to study nanocrystals in FINEMET alloys [156,222]. This technique gives complementary information to that of the SAXS technique described above.

Zhu et al. [305] have used neutron diffraction to study nanocrystallization process of $Fe_{73.5}Si_{22.5-x}B_xCu_1Nb_3$ ($x = 5$, 9, and 12) amorphous alloys. In situ experiments were performed in which a comparison of the radial distribution function peak areas with those predicted for the BCC and DO_3 structures was made. It was concluded that the amount of ordering in the DO_3 Fe(Si) crystals increases with the silicon concentration.

5.4. Experimental observations: microscopy

5.4.1. Nanoparticle powders

McHenry et al. [202] and Gallagher et al. [60] have employed a carbon arc method to synthesize C-coated transition metal elemental and alloy particles with nanocrystalline dimensions for the $Fe_{1-x}Co_x$[C] system. Fe and Co have similar sizes which have lead to the notable lack of chemical segregation (Fig. 32) in C-arc produced FeCo alloy nanoparticles [60]. Energy filtered transmission electron microsopy (EFTEM) has become a tool for characterizing the chemistry of these materials with extraordinary spatial resolution. State of the art analytical TEM facilities (EFTEM [188], STEM, PEELS) have allowed probing of the chemistry on a nanometer size scale.

Scott et al. [244,245] have examined chemical homogeneity in plasma torch synthesized FeCo alloy powders. Nanoparticles were prepared from elemental powders and a prealloyed $Fe_{50}Co_{50}$ starting material produced by ultrasonic gas atomization. The resulting thermal plasma product was examined with energy-dispersive X-ray spectrometry. Nanoparticles produced from alloy precursor showed a smaller spread in Fe/Co ratio than nanoparticles produced from elemental powders. Fig. 33 compares the compositional spread of the two runs in a scatter plot of Co abundance (as estimated from the Co X-ray fraction) for several particles sampled from each powder. The increased Fe/Co dispersion for the mixed element powders suggests that precursor homogeneity can impact the quality of the final nanoparticle powder.

The $Fe_{1-x}Co_x$[C] system has also been the subject of the plasma torch synthesis efforts of Turgut et al. [272] as described in Section 3. Recently, Turgut et al. [273] have examined equiatomic FeCo nanoparticles with a protective oxide coating (Fig. 34). Air mixed with the plasma gas is responsible for the oxidation. Structural characterization by conventional and synchrotron X-ray diffraction

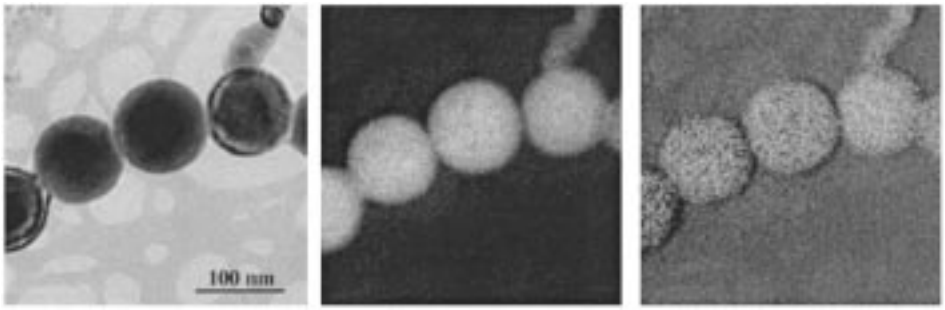

Fig. 32. Bright field image of FeCo nanoparticles and EFTEM of Fe and Co in the same (courtesy of J.H. Scott, reproduced from Gallagher et al. [60]).

indicated a disordered BCC α-FeCo phase. High resolution transmission electron microscopy (HRTEM) revealed spherical particles with several-monolayer-thick protective oxide coatings (Fig. 34) and a broad log normal size distribution. Fig. 34(a) shows a HRTEM image of as produced particles. Spherical particles with a several atomic layer thick protective $CoFe_2O_4$ were observed. Elemental mapping by EDX indicated homogeneous alloying by plasma torch synthesis and a continuous protective oxide layer formation. Thermomagnetic measurements were carried out using a SQUID magnetometer and a VSM at temperatures between 5

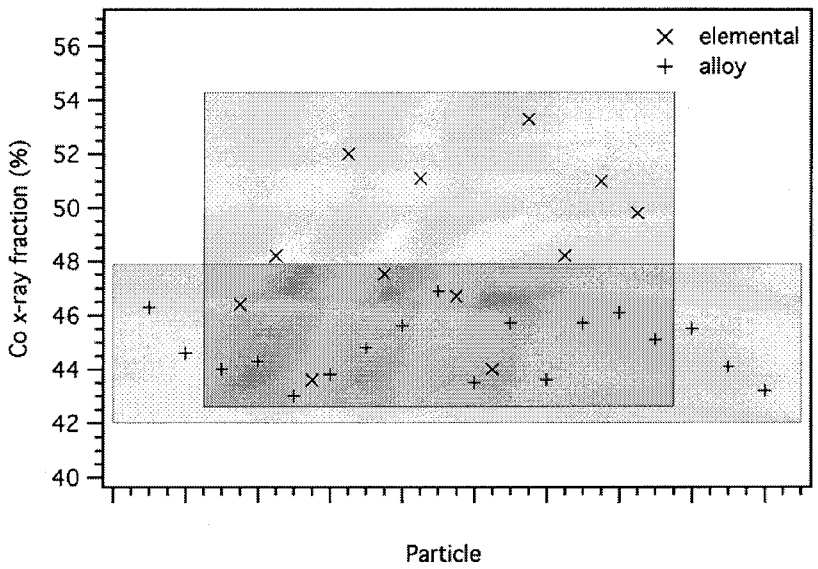

Fig. 33. Scatter plot showing composition variation in nanoparticles produced from elemental and pre-alloyed precursors. Shaded boxes roughly delineate the compositional range of each particle population (courtesy J.H. Scott, reproduced from Scott et al. [245,246]).

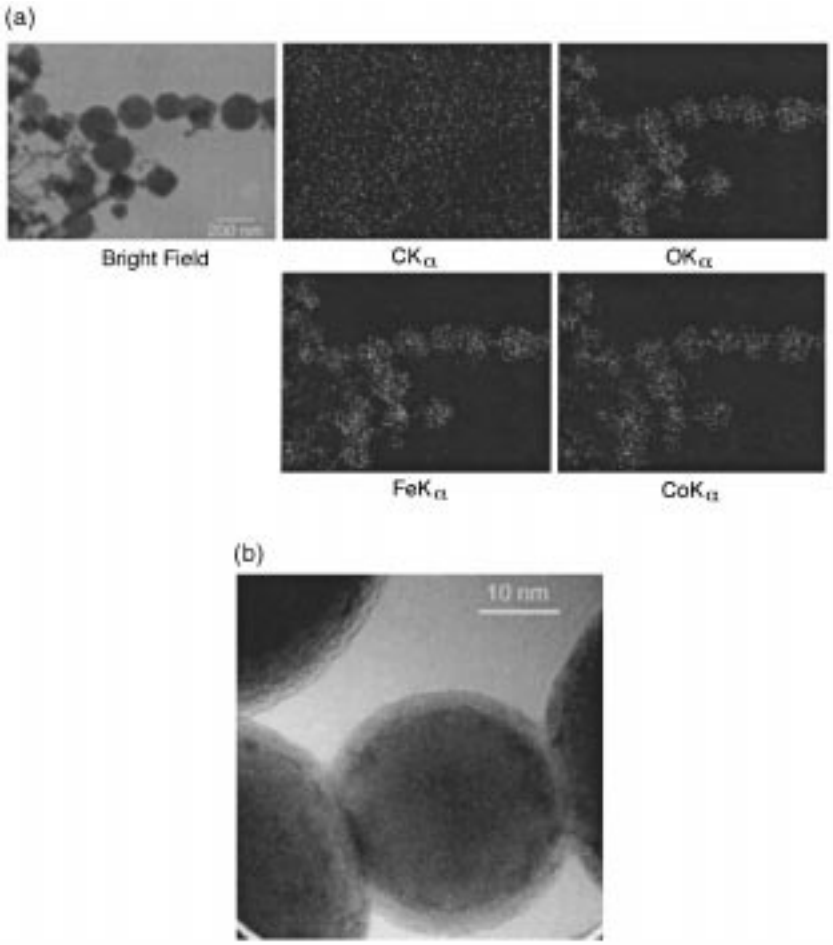

Fig. 34. Elemental mapping [courtesy of Nuhfer, reproduced from Turgut et al. [273] (a) and bright field image of as produced particles showing protective ferrite coating around them (b).

and 1050 K. Exchange bias coupling was observed due to the presence of the oxide layer.

5.4.2. FINEMET alloys

FINEMET alloys were first reported on by Yoshizawa et al. [290] followed by reports by Yoshizawa et al. [291], Yoshizawa and Yamauchi [292,293]. Yoshizawa and Yamauchi [294] reported on $Fe_{76.5-x}Si_{13.5}B_9M_xCu_1$ alloys in which the grain size was reduced most by Nb = Ta > Mo = W > V > Cr, with similar ordering for the best soft magnetic properties. Optimum magnetic properties were found for an alloy of composition $Fe_{73.5}Si_{13.5}B_9Nb_3Cu_1$ (FINEMET).

Schafer et al. [239] have examined magnetic domains in FINEMET using

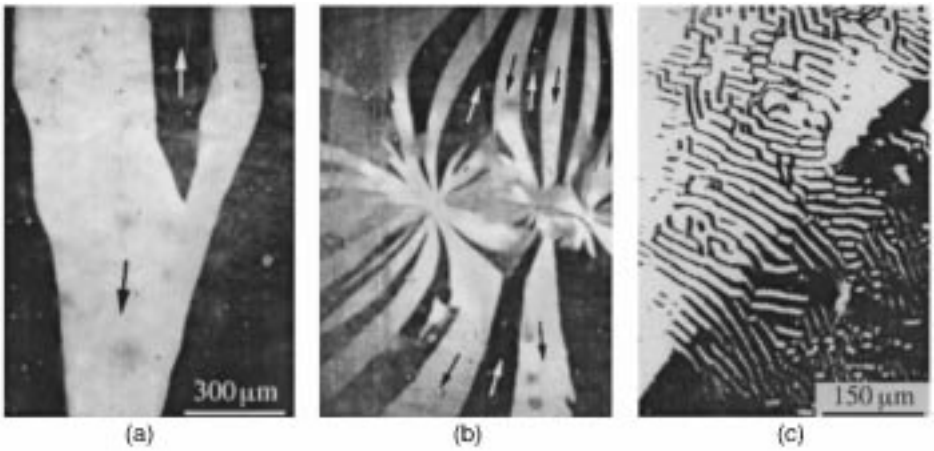

Fig. 35. Typical domains observed at low resolution in an optimally annealed sample of Fe $Fe_{73.5}Si_{13.5}B_9Nb_3Cu_1$ showing regular wide domains (a), rare stress domains around boride inclusions (b) and rare zones under compressive stress (c). (reproduced with permission from Schafer et al. [239]).

digitally enhance magneto-optic Kerr effect microscopy. The domain patterns resembled those of metallic glasses. Wide in-plane domains (several 100 μm) were observed along with characteristic stress patterns. Irregular domain patterns were

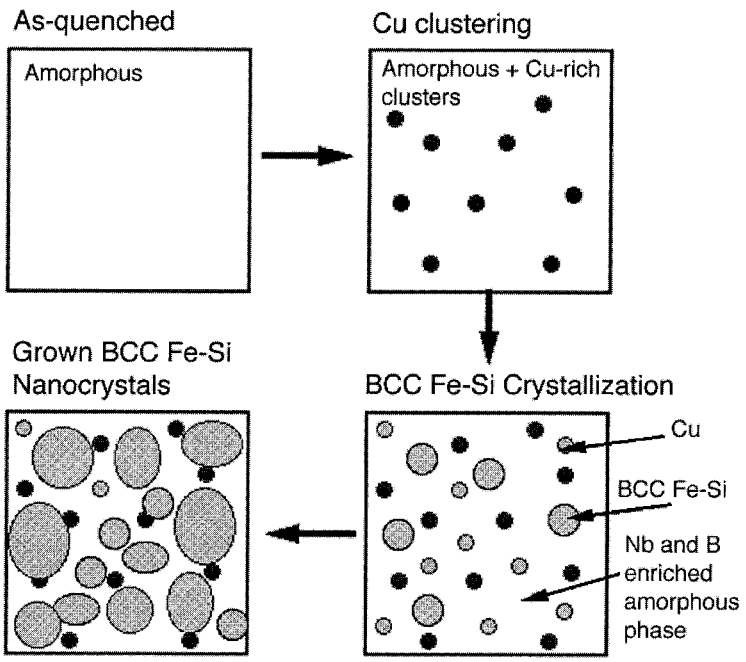

Fig. 36. Proposed sequence of events in the nanocrystallization of FINEMET alloys (after Hono [117]).

observed for samples that were over-annealed as well as for optimally annealed samples at temperatures above the Curie temperature of the intergranular amorphous phase (~320°C). Fig. 35 illustrates typical domains observed at low resolution in an optimally annealed sample.

Hono et al. [116] have investigated the microstructure of FINEMET, $Fe_{73.5}Si_{13.5}B_9Nb_3Cu_1$ using atom probe microscopy. While the five alloy components were found to be homogeneously distributed in the amorphous precursor to FINEMET after nanocrystallization it was found that two phases could be identified, an α-Fe–Si solid solution as the nanocrystalline phase and a B- and Nb-enriched and Si-depleted intergranular region. The results were not conclusive as to the distribution of Cu in these two phases. These observations suggested that primary crysallization is of the α-Fe–Si solid solution with exclusion of Nb and B to intergranular amorphous region. Secondary crystallization is from this intergranular material. It was observed that since Cu is virtually insoluble in Fe, exclusion of Cu from the amorphous matrix would occur at an incipient stage of crystallization and would act as nucleation sites for crystallization of α-FeSi. Hono et al. [117] made further atom probe field ion microscopy (APFIM) and HRTEM observations of the microstructural evolution in the nanocrystallization of $Fe_{73.5}Si_{13.5}B_9Nb_3Cu_1$. In the process of nanocrystallization at 550°C the following sequence of events was observed:

1. The initial precursor material is fully amorphous.
2. At the initial stages of crystallization, Cu enriched clusters of a few nm in size were observed to form.
3. α-FeSi nucleate, presumably at the site of incipient Cu clustering.

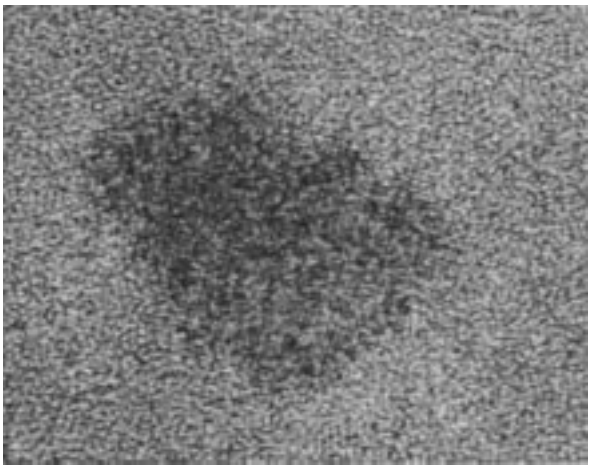

Fig. 37. HRTEM picture of an α-FeSi nanoparticle embedded in an amorphous matrix (courtesy of Hono, NEDO Web site: http://inaba.nrim.go.jp/apfim/NEDO.html).

4. α-FeSi nanocrystals grow while expelling Nb and B to the intergranular amorphous phase.

After nanocrystallization to the point of optimal microstructure there were three phases present. These were a (~20 at% Si) BCC solid solution, a residual amorphous phase with ~5 at% Si and 10–15 at% Nb and B and a third phase with ~60% Cu, < 5 at% of Si, B and Nb and ~30 at% Fe. These observations suggest that Cu cluster formation promotes chemical segregation and nucleation of the primary phase. Nb and B, which have low solubility in Fe, are expelled from the BCC Fe–Si crystals. A Nb- and B-rich residual amorphous phase surround the nanocrystals. The sequences illustrated in Fig. 36. Fig. 37 shows HRTEM picture of an α-FeSi nanoparticle embedded in an amorphous matrix of a crystallized FINEMET alloy (courtesy of K. Hono, NEDO Web site: http://inaba.nrim.go.jp/apfim/NEDO.html).

Koster et al. [168] studied nanocrystallization of metal–metalloid glasses, by electron microscopy and in situ time-resolved X-ray diffraction. In a $Fe_{66}Ni_{10}B_{24}$ glass the finest microstructure was obtained by annealing at temperatures significantly below the nose in a time temperature transformation (TTT) curve. This microstructure consisted of ~100 nm grains. For FINEMET materials, the significantly smaller ~10 nm grains were attributed to a reduced growth of Fe–Si rate as a result of dissolved Nb and with progressive expulsion of Cu an increased nucleation rate of primary crystallites. The fast nucleation, but slow growth gives rise to the extremely fine microstructure.

Müller et al. [209] studied the structure and the magnetic properties of amorphous FeSiBCuNb (FINEMET) alloys. Annealing at ~500°C lead to nanocrystallization of an Fe(Si) phase. In alloys with a Si content < 12 at% an Fe–Si solid solution in BCC Fe was observed. Alloys with Si > 12 at% crystallized in the ordered DO_3 superstructure. A mean grain size between 5 and 12 nm was observed depending on annealing temperature and composition. Müller et al. [210] studied the influence of Cu/Nb content and annealing conditions on the microstructure and the magnetic properties of FINEMET alloys. Grain size, phase composition and transition temperatures were observed to depend on the Cu/Nb content. The magnetic properties are strongly correlated to the microstructural features.

5.4.3. NANOPERM alloys

TEM observations [293] and and XRD [215] on NANOPERM materials have shown that the nanocrystalline magnetic phase was a BCC Fe solid solution. HRTEM, Mossbauer and atom probe microscopy [116] have all provided evidence for materials with optimum magnetic properties having two phases, amorphous and the BCC phases. Kim et al. [146] investigated the operative microstructural mechanism behind increased effective permeabilities in $Fe_{93-x}Z_7B_4$ ($x = 2, 4, 6, 8$) alloys with B additions. Here nanocrystalline α-Fe were responsible for the high permeabilities. For $x = 2, 4$ and an intergranular boride phase was said to develop from a spinodal-type decomposition. For higher B contents ($x = 6, 8$)

inhomogeneous grain distributions were observed with correspondingly lower permeabilities.

Makino et al. [190,191] observed 10–20 nm α-Fe nanocrystals in Fe–Zr–B, Fe–Hf–B and Fe–Nb–B alloys which were melt-spun to produce amorphous precursors and annealed for one hour at temperatures between 500 and 650°C. These materials had permeabilities up to 3.2×10^5, core losses of 0.066 W/kg at 1 T and 50 Hz, inductions up to 1.63 T and magnetostrictions as low as -1×10^{-6}. Small grain sizes and low magnetostriction were cited as being responsible for the good soft magnetic properties. Suppression of grain growth was attributed to large solute concentrations in the intergranular phase.

Zhang et al. [298] have studied the partioning of Si in the nanocrystallization process of an amorphous precursor to form a NANOPERM-related material. Unlike the observations for FINEMET alloys, where an α-FeSi solid solution is observed for the nanocrystals formed by primary crystallization in this NANOPERM related phase Si is expelled from the α-Fe matrix into the residual amorphous phase. This is explained by comparing the enthalpy of mixing ΔH_{mix} for ZrSi (~18.5 kcal/mol) and FeSi (−9.423 kcal/mol). This suggests a stronger Zr–Si interaction as compared with Fe–Si and thus a preference for Si in the Zr-rich amorphous phase. The larger early transition metal (TE = Zr) concentrations in NANOPERM as compared with FINEMET (TE = Nb) also seems to favor this partitioning.

Zhang et al. [299] have studied the structural evolution in an $Fe_{90}Zr_7B_3$ alloy by APFIM and HRTEM and concluded that primary crystallization proceeded by the explusion of Zr from the α-Fe nanocrystals to a Zr- and B-rich intergranular amorphous phase. Whereas the Fe, Zr and B concentrations were homogeneous in the as-quenched amorphous materials, HRTEM indicates that domains of medium range order (MRO) may be present. During nucleation and growth of the nanocrystalline phase MRO was observed prior to nucleation. It is suggested that

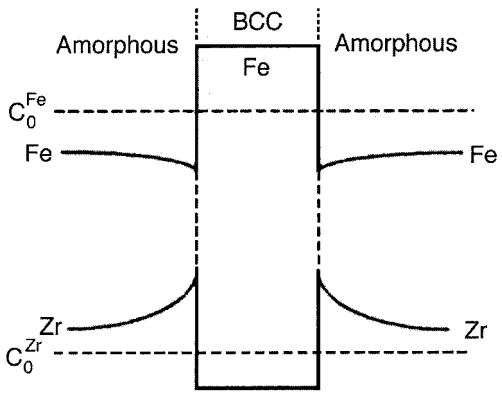

Fig. 38. Schematic representation of the concentration profile of Fe and Zr near an α-Fe nanocrystal for an $Fe_{90}Zr_7B_3$ alloy annealed for 1 h at 723 K (adapted from Zhang et al. [299].

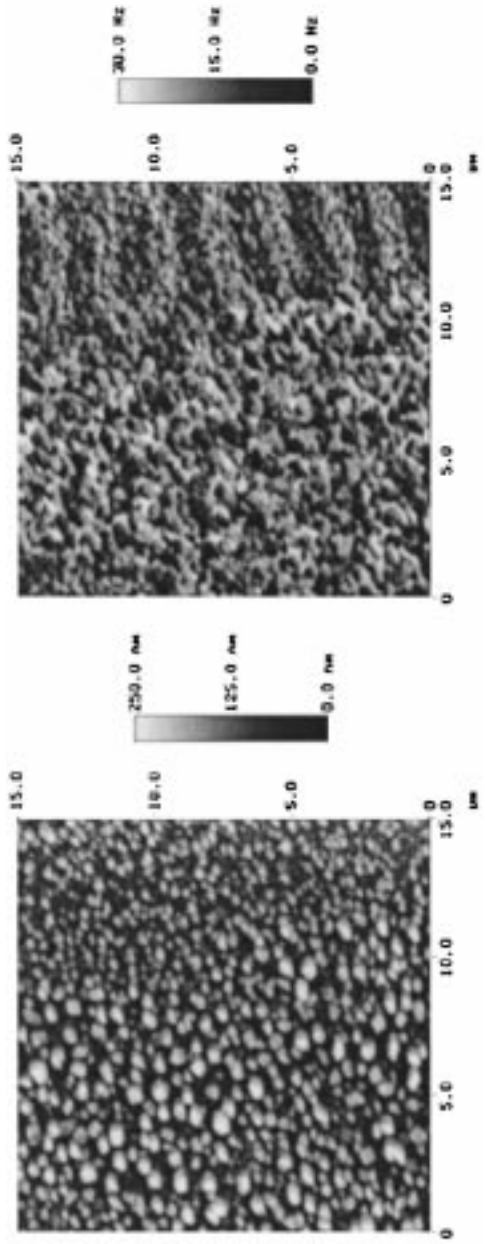

Fig. 39. Microstructure and magnetic domains as imaged by MFM in HITPERM magnets [310].

regions of MRO act as nucleation sites for the α-Fe nanocrystals. Growth is thought to be controlled by Zr diffusion, i.e. its expulsion to the grain boundaries. TEM and APFIM evidence for a Zr concentration gradient in front of the α-Fe nanocrystal interface was presented (Fig. 38). For materials with the optimum magnetic properties the Zr concentration gradient disappears suggesting that primary crystallization has been completed and a metastable partitioning of Zr and B between the amorphous and nanocrystalline phases has been achieved. In this non-Cu containing alloy, no evidence for decomposition prior to crystallization was found.

Hasegawa et al. [90] have examined the magnetic domain structure of Fe-(Zr,Nb)-B nanocrystalline alloys using Lorentz electron microscopy. The domain structure was shown to depend on the mean grain size as well as the structural inhomogeneities and the strength of the intergranular coupling. For materials annealed so as to achieve the largest permeability, large domains (3–4 μm) with straight domain walls and little magnetization ripple were observed. For less than optimum annealing larger magnetization ripple and more wandering domain walls were observed.

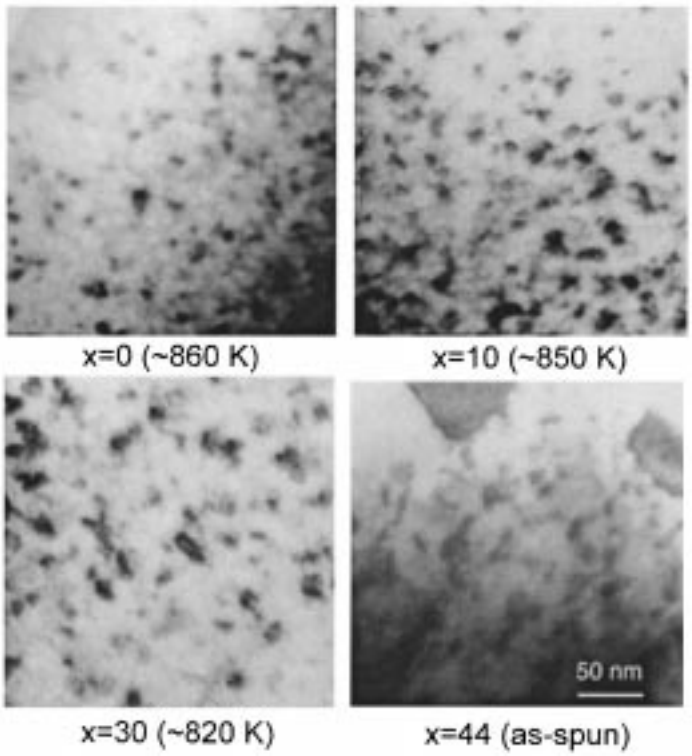

Fig. 40. TEM micrographs for annealed $(Fe_{1-x}Co_x)_{88}Hf_7B_4Cu$ HITPERM magnet ribbons (a) $x = 0$, (b) $x = 10$, (c) $x = 20$ and (d) $x = 44$ (as cast) [134].

Stress-induced magnetic domains, orthogonal to the surface of Si-steels are known to cause low frequency power losses. Shear bands in bent amorphous FeBSi ribbons have been studied by Brown et al. [29] using magnetic force microscopy (MFM). These studies point to the usefulness of MFM in mapping magnetic domains in soft magnetic materials. Recently, Hawley [310] has observed nanocrystalline microstructural features in nanocrystalline HITPERM ribbons by scanning tunneling microscopy (STM) and corresponding domains using MFM. Variations with of the nanocrystal size with position in the ribbon and corresponding changes in the domain structure with nanocrystal size are evident in Fig. 39. This technique is likely to help answer some of the still open questions as to intergranular coupling, domain walls and pinning in nanocrystalline soft magnetic materials.

5.4.4. HITPERM alloys

Nanocrystalline $(Fe,Co)_{88}Hf_7B_4Cu$ (HITPERM) alloys have been investigated by Iwanabe et al. [134] as candidates for soft magnetic materials for high temperature applications. Nanocrystalline alloys were obtained by crystallization of melt-spun amorphous precursors. To examine the thermal stability, AC magnetic properties were measured at room temperature for the 30% Co alloy annealed at 823 K for times of 20 and 100 h. The microstructures were observed with the conventional TEM and the high HRTEM. The amorphous phase in as-spun ribbons (Cu wheel) were confirmed by broad XRD peaks (and the absence of crystalline peaks) and crystallization peaks in the DTA experiments. The XRD

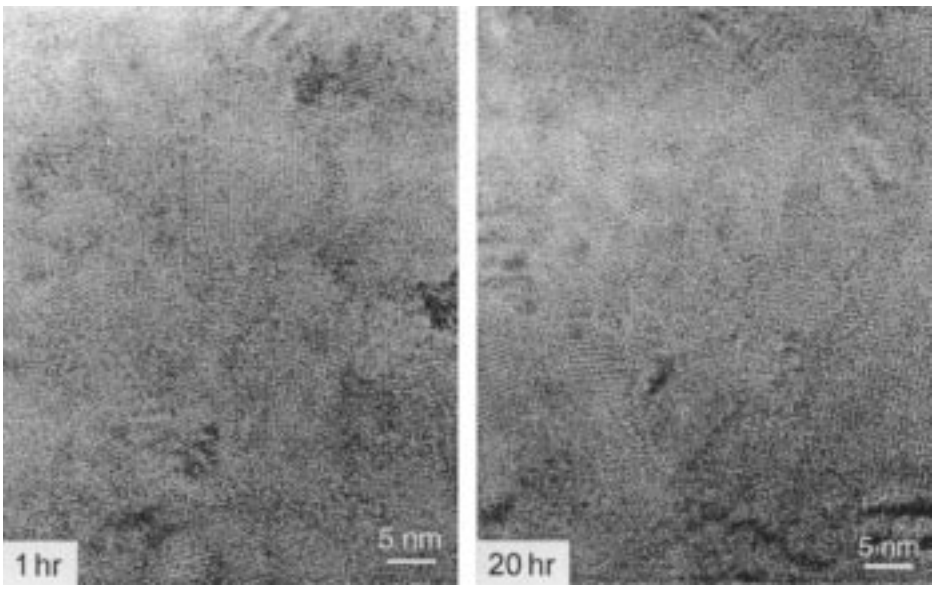

Fig. 41. High resolution TEM (HRTEM) micrograph of $(Fe_{0.7}Co_{0.3})_{88}Hf_7B_4Cu$ HITPERM magnet samples annealed at 600°C for 1 and 20 h [134].

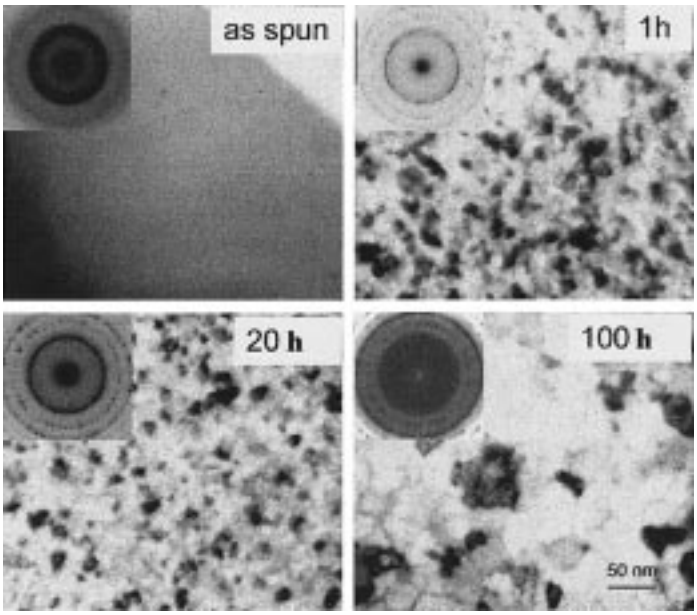

Fig. 42. TEM micrographs for annealed $(Fe_{0.7}Co_{0.3})_{88}Hf_7B_4Cu$ HITPERM magnet ribbon annealed at 600°C for (a) as-spun. (b) 1 h, (c) 20 h, and (d) 100 h [134].

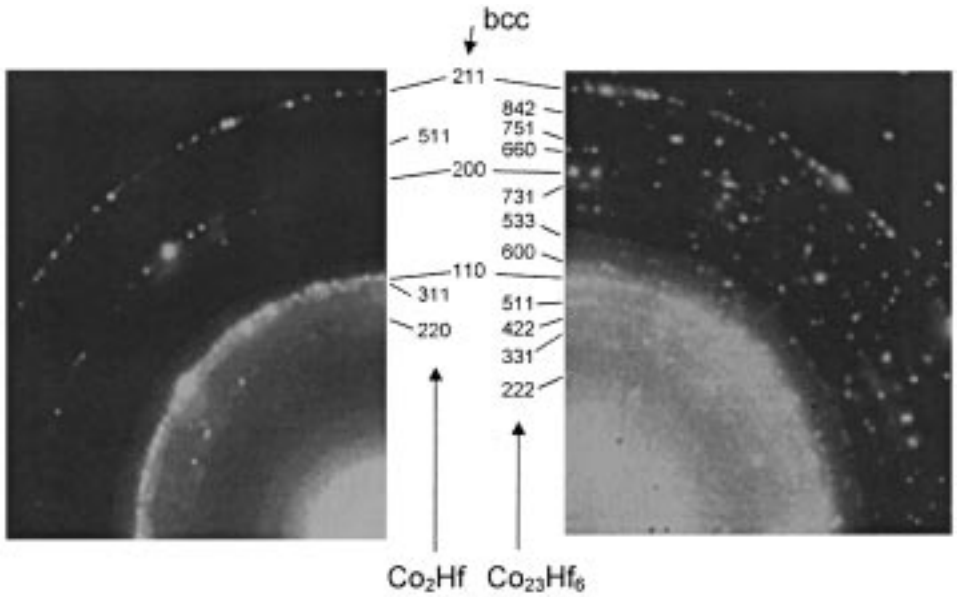

Fig. 43. Electron diffraction patterns of $(Fe_{0.7}Co_{0.3})_{88}Hf_7B_4Cu$ HITPERM magnet samples annealed at 600°C for 500 and 1000 h [134].

results for nanocrystallized samples in DSC and the as spun 44% Co ribbon showed clear BCC peaks (with significant Scherrer broadening) without any strong peaks from other phases. Fig. 40 shows TEM micrographs of these crystalline ribbons for four different compositions. Fig. 41 shows HRTEM micrographs of a $(Fe_{0.7}Co_{0.3})_{88}Hf_7B_4Cu$ HITPERM nanocrystalline magnet samples annealed at 600°C for 1 and 20 h [134].

Further studies focused on the thermal stability of the 30% Co alloy that has the highest magnetization among the four compositions. The alloy was relatively stable up to 20 h, with the grain size remaining ap10 nm as illustrated in Fig. 42(b) and (c). Between 20 and 100 h anneals, grain growth was observed and the core losses increased (which may be due to the crystallization of the remaining amorphous phase). In the 500 h annealed sample (Fig. 43), electron diffraction rings of the paramagnetic $Co(Fe)_2Hf$ phase were observed. The diffraction rings corresponding to $Co(Fe)_2Hf$ disappeared, being replaced by rings of the $Co(Fe)_{23}Hf_6$ phase for the 1000 h annealed sample. High resolution TEM (HRTEM) work was also helpful in understanding coarsening and precipitation of second phases in this alloy.

5.4.5. Other alloys

The nanocrystalline structure of Fe–Ta–C materials differs from that of typical FINEMET, NANOPERM and HITPERM alloys. In the latter a continuous amorphous phase coats and couples the nanoparticles. Soft magnetic properties depend intimately on the nature of the nanocrystal–amorphous–nanocrystal coupling. In the former a refractory carbide phase tends to form at grain boundary triple points. These carbides tend to pin grain boundaries with consequent prevention of coarsening. This type of nanocrystalline microstructure does not prohibit direct exchange between the magnetic nanoparticles.

Fujii et al. [58] have investigated the nanocrystallization process in bulk amorphous-like $Fe_{78}P_{18-x}Cu_{0.5}Ge_3Si_{0.5}$ ($x = 8$, 9, 10, 11, 12, 13, 16 and 18) and $Fe_{79.5}P_{12}C_6Cu_{0.5}Mo_{0.5}Si_{1.5}$ alloys. Amorphous precursors were prepared by single roller melt spinning. They observed primary crystallization of BCC Fe. A two-phase microstructure with 16–80 nm Fe nanocrystals and an amorphous matrix were observed. Surprisingly the volume fraction of Fe nanocrystals did not exceed ~30%. Coercivities as low as 0.02 Oe were observed in these materials with the finest grains with the coercivity observed to grow to >2 Oe in the largest grained materials. Liu et al. [180] have studied the nanocrystallization of an $Fe_{81.5}P_{12}C_3Cu_{0.5}Mo_{0.5}Si_{2.5}$ alloy. The observed primary crystallization to produce ~20 nm grains of α-Fe(Si) in a residual amorphous matrix. 2–5 at% Si was dissolved in the FeSi crystallites with nearly zero ordering.

Quintana et al. [312] have studied the nanocrystallization process of amorphous Co-based, $Co_{66}Fe_4Mo_2S_{16}B_{12}$, alloys (starting with Vitrovac^R 6025) metallic alloys. Samples were annealed at temperatures between 403–443°C (below a T_{x1} of 558°C) for 10–90 min intervals. Permeabilities of 10^5 were observed in annealed samples. For samples annealed less than 60 minutes a grain size of <30 nm was observed by TEM.

Kras et al. [172] have examined microstructure and magnetic properties of amorphous and nanocrystalline $Co_{21}Fe_{64-x}Nb_xB_{15}$ ($x = 3$, 5 and 7) alloys. They report BCC Fe–Co grains embedded in a residual amorphous matrix for nanocrystallized samples. A one hour anneal at 600°C resulted in 12 nm BCC grains for the $x = 7$ alloy. Primary crystallization was observed to increase induction and reduce the magnetostriction. Saturation inductions of 1.42 T and magnetostriction coefficients of 21.4×10^{-6} were reported for the nanocrystalline alloys.

5.5. Experimental observations: Mössbauer spectcroscopy

5.5.1. FINEMET alloys

Mössbauer spectroscopy has been used to identify the phases formed in annealing of FINEMET FeCuNbSiB alloys [79,229,302]. Rixecker et al. [231,232] studied $Fe_{1-x}Si_x$ alloys ($13 < x < 27$) using Mössbauer spectroscopy to shed light on the spectra observed in FINEMET alloys. Non-stoichiometric alloys showed Mossbauer spectra with many subspectra of the various Fe present in the $D0_3$ structure.

Pradell et al. [228] have used transmission Mössbauer spectroscopy to study the nanocrystallization process in $Fe_{73.5}Si_{17.5}B_5Cu_1Nb_3$ during isothermal annealing at 490°C. Two distinct stages in the nanocrystallization process were observed: (1) stage one consisted of changes in the short-range order parameters of the amorphous phase, and (2) followed by nanocrystallization of $D0_3$ Fe–Si. The silicon content in the nanocrystals was observed to decrease with annealing time. The nanocrystalline phase formed in the second stage showed a preferential magnetic orientation parallel to the ribbon surface. The observation of two stages was taken to suggest that nanocrystallization is driven by nucleation and growth.

An RF Mössbauer sideband collapse technique has been employed to study FINEMET alloys. [74,75] the details of this technique are discussed below, in the context of observations on NANOPERM materials.

5.5.2. NANOPERM alloys

Mössbauer spectroscopy has also been used to identify the phases formed in annealing of NANOPERM Fe–M–B alloys e.g. [42], Kopcewicz et al. [163,164] have examined $Fe_{93-x-y}Zr_7B_xCu_y$ ($x = 4$, 6, 8, 12, and $y = 0$ or 2) alloys using Mössbauer spectroscopy to follow the formation of nanocrystalline BCC-Fe at anneal temperatures between 430 and 600°C.

Brzozka et al. [30] reported a bimodal hyperfine distribution with an additional low field component in the Mössbauer spectra of FeZrB(Cu) amorphous alloys. The bimodal distribution is interpreted in terms of Fe atoms with nearly full coordination and others partially coordinated by Zr and B atoms. The distribution of Fe–Fe pairs is used to postulate the existence of both ferromagnetic and antiferromagnetic exchange interactions. Magnetic exchange frustration resulting from this distribution of exchange interactions gives rise to

the re-entrant spin glass behavior in this alloy. A strong compositional (B-content) dependence of the Mössbauer spectra was observed.

Kopcewicz [159] has modeled the frequency modulation of the RF sideband effect and predicted such a RF field amplitude growth of the side bands. The observation of the sidebands in this alloy suggests that these measurements are made at a temperature (room temperature) exceeding, T_C^{am}, the transition temperature of the amorphous phase. Preliminary results of the RF sideband technique to studies of NANOPERM alloys are reported by Kopcewicz [161,162]. In nanocrystalline materials the RF-sideband technique allows for the distinction between signals from magnetically soft nanocrystaline BCC α-Fe and the harder microcrystalline α-Fe. Kopcewicz et al. [160–166] have employed a radio-frequency-Mössbauer technique to study nanocrystalline soft magnetic materials.

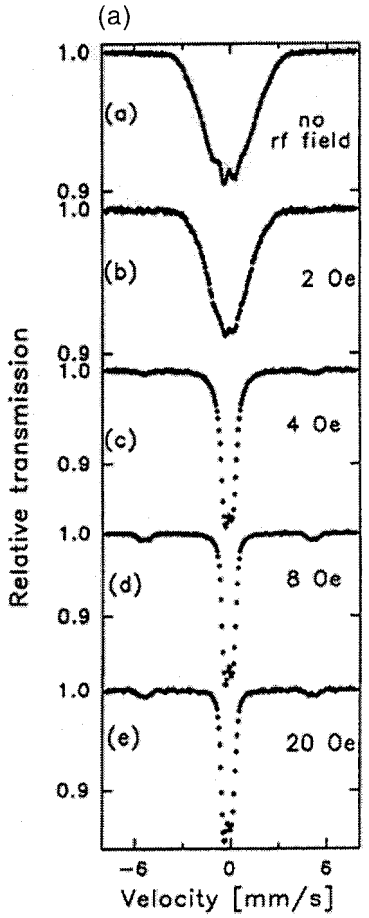

Fig. 44. (a) RF collapse of Mössbauer sidebands in an amorphous $Fe_{73.5}Nb_{4.5}Cr_5B_{16}Cu_1$ alloy [164,165] and (b) for a nanocrystalline $Fe_{79}Zr_7B_{12}Cu_2$ alloy [163,164].

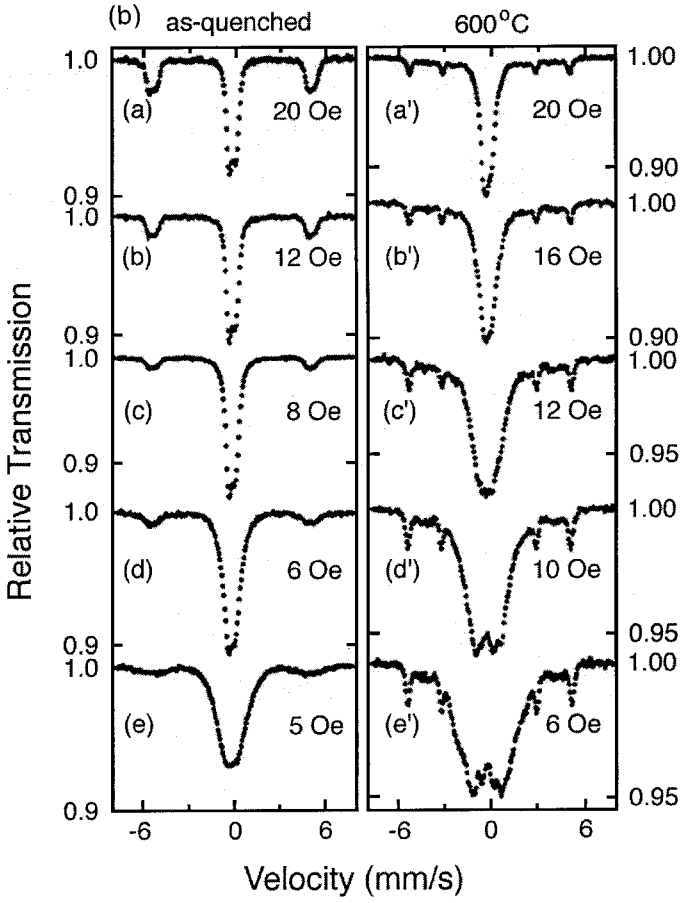

Fig. 44 (*continued*)

In this technique a RF induced collapse of the M1ssbauer spectra is employed to study the structure of amorphous and nanocrystalline FINEMET and NANOPERM related alloys. Radio frequency induced effects (i.e. RF collapse and RF side bands) allow for the distinction between nanocrystalline BCC α-Fe and the magnetically harder microcrystalline α-Fe.

Fig. 44(a) shows the RF collapsed spectra as a function of RF field intensity for an as quenched amorphous $Fe_{73.5}Nb_{4.5}Cr_5Cu_1B_{16}$ alloy. The RF side-bands are seen clearly to grow with the RF field amplitude. The side bands are associated with magnetostrictively induced modulation of the M1ssbauer γ-radiation of ^{57}Fe atoms contained in the amorphous alloy.

Kopcewicz et al. [163,164] have used the magnetic radio frequency collapse and radio frequency sidebands to study microstructure and magnetic anisotropy in $Fe_{93-x-y}Zr_7B_xCu_y$ ($x = 6,\ 8,\ 12;\ y = 0,\ 2$) nanocrystalline alloys formed through

annealing between 500 and 600°C. RF collapse was observed in the amorphous and nanocrystalline phases and was suppressed in materials where (larger) microcrystalline α-Fe was observed to form. The disappearance of RF sidebands after nanocrystallization is taken as evidence for vanishing magnetostricton. Distributions of anisotropy fields were determined from the field amplitude dependence of the Mössbauer intensity. Fig. 44(b) shows Mössbauer spectra as a function of RF field intensity for an as-quenched and annealed (550°C) $Fe_{79}Zr_7B_{12}Cu_2$ alloy.

Kemeny et al. [139] have studied the magnetic coupling between BCC magnetic nanocrystals in BCC Fe–Zr–B–Cu alloys. Using Mössbauer (^{57}Fe) spectroscopy,

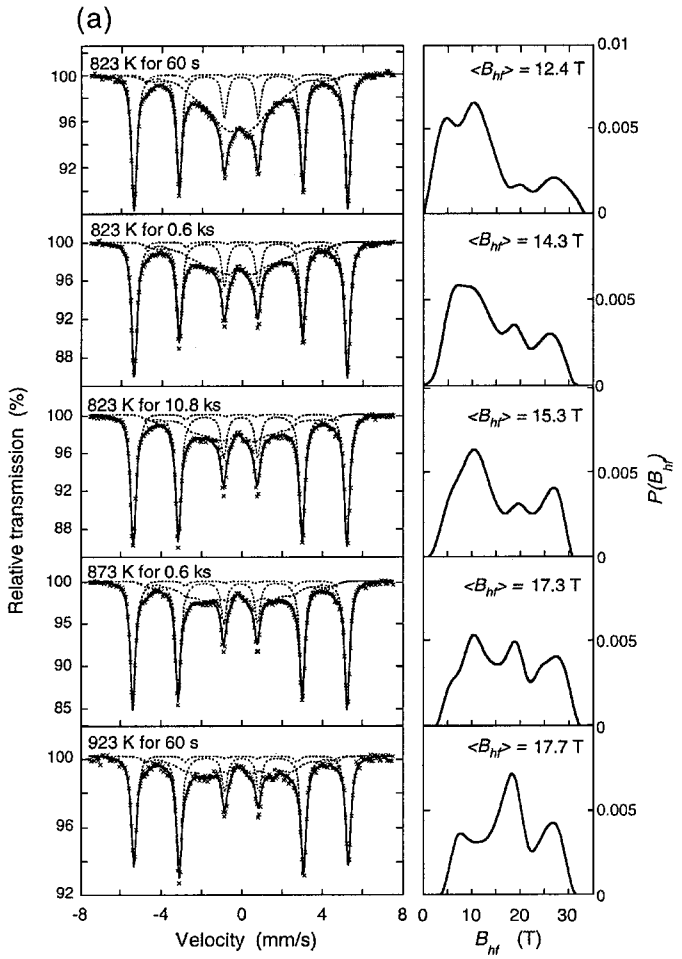

Fig. 45. (a) Mössbauer spectra and hyperfine distribution for nanocrystalline $Fe_{91}Zr_7B_2$ and (b) dependence of the coercivity on the square of the mean hyperfine field [267].

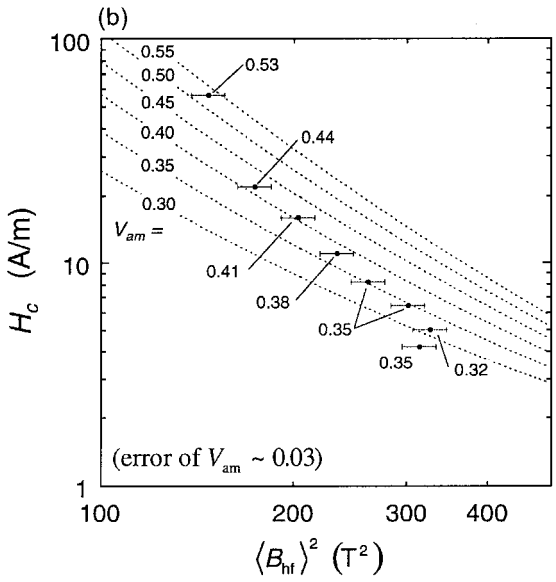

Fig. 45 (*continued*)

they found a formerly unidentified component of the Mössbauer spectra which appeared above the Curie temperature of the residual amorphous phase. Using the relative atomic fraction attributable to this signal, they concluded that it arose from an approximately two atomic layer Zr-rich component at the surface of the BCC Fe grains. They observe that the T-dependence of the α-Fe nanocrystal coupling is substantially manifest in the temperature dependence of the Mössbauer signal from this surface layer.

Kopcewicz et al. [163,164] have studied the magnetic properties of an $Fe_{80}Ti_7B_{12}Cu_1$ alloy by exploiting RF collapse and side band effects in the ^{57}Fe Mössbauer spectrum. Conventional Mössbauer spectroscopy allows for the identification of crystalline phases formed from annealing of amorphous precursors and for determination of their relative abundance. From the field dependent collapse of the sideband in RF-Mössbauer experiment the magnetic anisotropy fields in each phase can be determined. In the study of $Fe_{80}Ti_7B_{12}Cu_1$, changes in magnetostrictive coefficients with nanocrystallization we are determined as being responsible for changes in anisotropy.

Suzuki and Cadogan [267] have carefully studied the relationship between the mean hyperfine field of ^{57}Fe in the residual intergranular amorphous phase, $\langle B_{HF} \rangle$, and the coercivity, H_c, of the nanocrystalline soft magnetic samples. $\langle B_{HF} \rangle$ was varied by annealing $Fe_{91}Zr_7B_2$ amorphous precursors for times between 60 and 10,800 s at temperatures of 550–700°C, so as to vary the volume fraction of the nanocrystalline and residual amorphous phases. $\langle B_{HF} \rangle$ was observed to increase with decreasing volume fraction of the residual amorphous phase with consequent

decreases in H_c. The influence of the residual amorphous phase volume fraction on soft magnetic properties were discussed within the framework of Suzuki's extended two-phase random anisotropy model (as discussed in Section 6).

Fig. 45(a) shows a typical Mössbauer spectrum acquired for nanocrystalline $Fe_{91}Zr_7B_2$ along with the hyperfine field distribution, $P(B_{HF})$, of the amorphous phase. The total Mössbauer spectrum was fit using three spectral components, two sextets for α-Fe nanocrystallites and a broad sub-spectrum for the residual amorphous phase. Fig. 45(b) shows experimental and simulated relationships between the coercivity and $\langle B_{HF}\rangle^2$. The simulated relationships are based on the extended two-phase random anisotropy model using the assumption that the exchange stiffness in the amorphous phase A_{am} could be taken as being proportional to the square of the amorphous phase magnetization, $(M_s^{am})^2$.

5.5.3. HITPERM alloys

No Mössbauer experiments have yet been reported on for HITPERM alloys.

6. Intrinsic magnetic properties

6.1. Magnetic dipole moments

6.1.1. Amorphous alloys

The most important changes in the magnetic dipole moments in amorphous alloys depend more strongly on alloy chemistry rather than positional disorder. The issue of the influence of alloy chemistry on magnetic dipole moments and magnetization, previously illustrated in the Slater–Pauling curve, are also addressed in a more quantitative manner in a variety of empirical models. The Friedel model for transition metal alloys offers an insightful description of the density of states for d-electrons in transition metals, $g(\varepsilon)$. In the Friedel model, the density of states for *d*-electron bands is approximated by a constant over a band width, W. This is equivalent to smoothing the more complicated density of states and parameterizing it in terms of the constant $g(\varepsilon)$ and the band width, W. Alloy moment data are qualitatively well described in the Friedel model. Weak solutes, as defined by a valence difference $\Delta Z \leq 1$, are explained by a rigid band model while a virtual bound state model is employed when the solute perturbing potential is strong, $\Delta Z \geq 2$.

In dilute alloy solutions with solute atoms which are considered to be only weakly perturbing (i.e. they have a valence difference $\Delta Z \leq 1$) a rigid band model can be employed to explain alloying effects on magnetic moment. Rigid band theory (Fig. 46) assumes that d-band shape does not change in alloying. In this model, the magnetic moment of the solvent matrix is independent of concentration. At the site of a solute atom a moment reduction of $\Delta Z \mu_B$ is to be expected. The resulting average magnetic moment per solvent atom is then just the concentration weighted average of that of the matrix and that of the solute:

$$\mu_{av} = \mu_{matrix} - \Delta Z C \mu_B \tag{37}$$

Where C is solute concentration, ΔZ is valence difference between solute and solvent atoms. This relationship is the basis for explaining the Slater–Pauling curve (for $\Delta Z = 1$).

For transition metal impurities that introduce a strongly perturbing and highly localized potential, Freidel has proposed a virtual bound state (VBS) model to explain departure from the simple relationship given by Eq. (37). Friedel suggests that when the perturbation due to alloying is strong enough, a bound state will be subtracted from the full d-band majority spin band and moved to higher energies (for $\Delta Z > 2$). As the VBS moves above the Fermi level a dramatic change in the magnetic moment is predicted to take place as electrons in the VBS empty into the conduction band, i.e., into previously empty minority spin states. At this point for every additional solute atom added, a five fold degenerate majority spin 3d VBS will empty into five unoccupied minority spin 3d states. Thus the change in average magnetic moment is predicted to be:

$$\mu_{av} = \mu_{matrix} - (\Delta Z + 10) C \mu_B \tag{38}$$

Magnetic moment suppression is given by the VBS as:

$$\frac{d\mu_{av}}{dC} = -(10 + \Delta Z)\mu_B \tag{39}$$

The VBS model would predict a moment reduction of $-6\mu_B$ for V or Nb additions to Co, for example.

More recent models for moment reduction as a function of chemistry are based on coordination bonding [40,41] and on magnetic valence ideas of Malozemoff et al. [198]. The magnetic valence approach considers alloying effects on the average dipole moment in strong ferromagnets, i.e. one in which the Fermi energy, E_F, lies in either the minority spin band or the majority spin band or both. This leads to

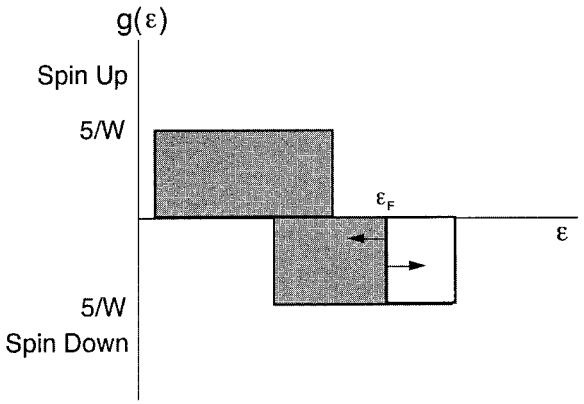

Fig. 46. Rigid band depiction of (un)filling of solvent d-bands as a result of alloying.

simplification in the discussion of moment enhancement or reduction due to alloying effects. In the magnetic valence model [283] an alloy chemical valence, Z, is simply define as the sum of the spin-up and spin-down electrons in the alloy:

$$Z = N\Uparrow + N\Downarrow \tag{40}$$

The alloy magnetic dipole moment. μ_{av}, is simply defined as:

$$\mu_{av} = N\Uparrow - N\Downarrow = 2N\Uparrow - Z \tag{41}$$

in units of Bohr magnetons. Now for transition metals the spins can be partioned into those of *d*- and *s*-electrons, respectively so that $N\Uparrow = N_d\Uparrow + N_s\Uparrow$. For strong ferromagnets with full majority bands $N_d\Uparrow = 5$ (e.g. Co and Ni). The magnetic valence due to polarization of the d-electrons is simply:

$$Z_M = 2N_d\Uparrow - Z \tag{42}$$

and the magnetic moment m_M for such strong ferromagnets is given by:

$$\mu_{av} = Z_M + 2N_s\Uparrow \tag{43}$$

indicating that the alloying effects on the magnetic dipole moment can be determined by changes in the number of sp electrons.

Another important model for alloy moment reduction that was been applied first to model moment reduction in transition metal (TM)–Metalloid (M) systems is the so-called coordination bonding model. In this model the moment reduction is viewed in terms of a polarizable d-state being robbed from the transition metal manifold for each TM–M bond which is formed (i.e. a p–d bond). In this model the average alloy dipole moment is given by:

$$\mu_{av} = \mu^0_{TM} - \left[1 - x\left(1 + \frac{Z_M}{5}\right)\right] \tag{44}$$

where M refers to the metalloid species, TM is the magnetic transition metal species, x is the composition of a $TM_{1-x}M_x$ alloy and Z_M is the coordination of M by TM atoms in the structure. Z_M can be measured (e.g. by EXAFS) or inferred from coordination in crystalline alloys of similar composition.

While the above mentioned empirical models are attractive because of their appeal to intuitive models of moment reduction, the improvement in accuracy of state-of-the art ab initio band structure calculations makes these among the most reliable means of predicting alloying effects on moments. Fig. 47 illustrates the predictive power of modern band structure techniques in predicting the effective moment of transition metal additions to elemental Fe as determined from band structure calculations. Alloying effects, of course are of great concern in understanding the intrinsic magnetic properties of amorphous alloys because of the relatively large amounts of non-magnetic species which must be added as glass formers, etc. In the case of early transition metal (TE) alloys, it is indeed fortuitous that the TE species that offer eutectic compositions closest to pure Fe

or Co also have a smaller moment reducing effect than other TM species in the middle of the transition metal series.

6.1.2. Nanocrystalline alloys

One of the goals of early studies of the magnetic properties of nanoencapsulates was the determination of the extent to which the specific magnetization could be increased as a result of control of the M:C ratios in carbon coated ferromagnetic nanoparticles and control of the alloy chemistry in carbon coated alloy ferromagnetic nanoparticles. McHenry et al. [307] have demonstrated that they could encapsulate up to 66 wt% Co in nanoparticles. The largest specific magnetization achieved in this system was 110 emu/g.

Gallagher et al. [60] have produced Fe_xCo_{1-x}[C] ($x = 0.0$, 0.2, 0.4, 0.5, 0.6, and 0.8, nominally) nanoparticles by a Kratschmer–Huffman carbon arc method. X-ray diffraction indicated a single BCC FeCo phase (along with graphitic coating), for all but the $x = 0.2$ composition for which some FCC Co was observed. Particles had an average diameter of 50 nm from Scherrer analysis of the peak widths, and a broad size distribution based on TEM. Gatan imaging energy-filtered microscopy (GIF) showed Fe and Co to be uniformly distributed in the nanoparticles. A compositional dependence of the $M(H = 1\ \mathrm{T})$ magnetization was similar to that observed in the bulk alloy Slater–Pauling curve (Fig. 48). $Fe_{0.5}Co_{0.5}$[C] exhibited the largest magnetizations observed in similarly produced nanoparticles. The $M(H)$ curves did not saturate, presumably due to some fraction of superparamagnetic particles.

Kuhrt and Schultz [173] have measured the saturation magnetization as a

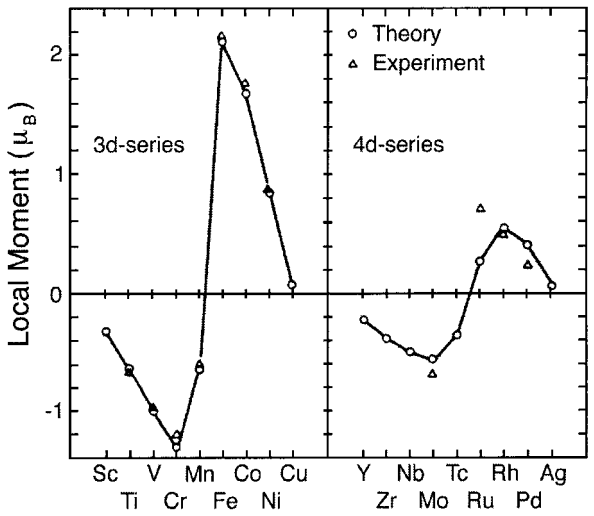

Fig. 47. Effective moment of transition metal additions to elemental Fe as determined from band structure calculations [1,76].

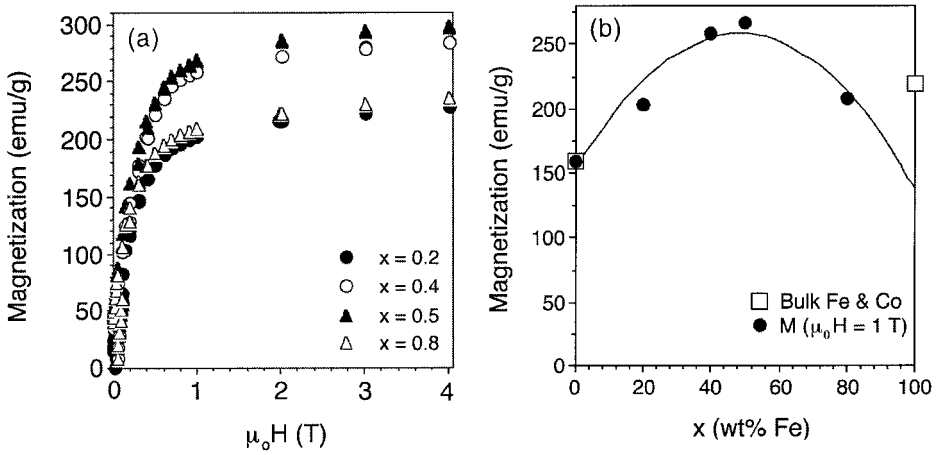

Fig. 48. (a) 5 K $M(H)$ of Fe_xCo_{1-x}[C] nanoparticles ($x = 0.2$, 0.4, 0.5, 0.6, 100 wt%) and (b) M(1 T) vs. x (wt%) and (b) $M(H = 1$ T) vs. x for nanoparticles including data for bulk Fe and Co for comparison. Parabola is a guide to the eye.

function of composition in mechanically alloyed $Fe_{100-x}Co_x$ powders and compared them with the unmilled elemental mixture as shown in Fig. 49. The mechanically alloyed samples were milled in a planetary ball mill using steel containers and balls. They show that the similarity in the compositional dependence of the saturation magnetization and that of the Slater–Pauling curve

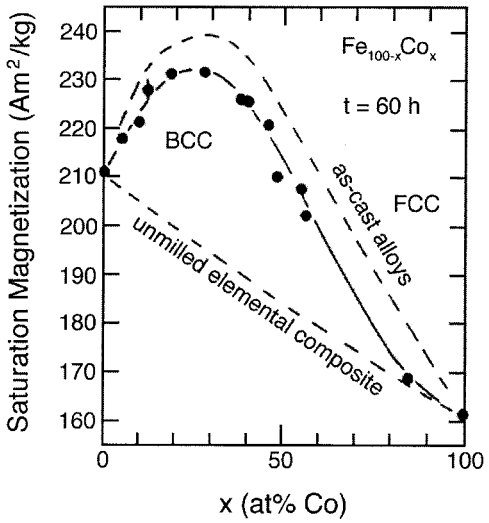

Fig. 49. Saturation magnetization as a function of Co content for MA $Fe_{100-x}Co_x$ powders as compared with the unmilled elemental mixture [173].

offers convincing evidence of alloy phase formation by mechanical alloying of the elemental powders. Their bulk magnetizations are observed to be several percent smaller than those of bulk as-cast alloys and attributed to incomplete reaction and to small amounts of non-magnetic wear debris. The peak moment occurred between 20 and 30 at% Co, again in excellent agreement with the bulk Slater–Pauling curve.

Vojtanik et al. [278,279] have investigated the influence of Ni substitution for Fe on the intrinsic magnetic properties in FINEMET alloys. $Fe_{73.5-x}Ni_xNb_3Cu_1Si_{13.5}B_9$ ($x = 0$, 5, 10, 15, 20 and 25 at%) amorphous and nanocrystalline alloys were studied by X-ray diffraction, Mössbauer spectroscopy and thermomagnetic analysis. Small additions of Ni were shown to increase the Curie temperature and the room temperature saturation magnetization of amorphous samples. Ni caused a suppression of the secondary crystallization temperature, T_{x2}. A nanocrystalline structure was observed after crystallizing the $x = 0$, 5, 10 and 15 alloys but not for the $x = 20$ and 25 at% alloys. The 5 at% Ni addition increases the room temperature B_s from 1.19 to 1.39 T and T_C of the amorphous phase from 332 to 337°C. Both quantities decrease for higher Ni concentrations.

6.2. Magnetic exchange interactions and T-Dependent ferromagnetic response

6.2.1. Amorphous alloys

Because of large deviations in interatomic spacings in amorphous alloys as compared with bulk crystalline materials amorphous alloys typically have reduced Curie temperatures (due to alloying with glass forming elements [231] as well as distributed exchange interactions which alter the mean field description of the temperature dependence of the magnetization, $M(T)$). A mean field theory for the temperature dependence of the magnetization in amorphous alloys has been proposed by Handrich and Kobe [80,152,153]. In this Handrich–Kobe theory was proposed an expression for the reduced magnetization $m(T) = M(T)/M$ (0 K) which consisted of a modified Brillouin function where a single exchange parameter was replaced by an exchange parameter reflecting the distribution of nearest neighbor positions in the amorphous phase [136]. This reduced magnetization is expressed as:

$$m(T) = \frac{1}{2}\left(B_s\left[(1+\delta_{ex})x\right] + B_s\left[(1-\delta_{ex})x\right]\right) \tag{45}$$

where

$$x = \frac{3S}{S+1}\frac{m}{t} \quad \text{and} \quad t = \frac{T}{T_C} \tag{46}$$

are the arguments of a conventional (spin-only) Brillouin function B_s. Further the exchange fluctuation parameter [34] is defined:

$$\delta_{ex} = \sqrt{\frac{\langle \Delta J^2 \rangle}{\langle J \rangle^2}} \tag{47}$$

This parameterizes the root mean square (rms) fluctuation in the exchange interaction. The root mean square exchange fluctuation has been suggested to have a T-dependence of the form [18]: $\delta_{ex} = \delta_{0\,ex}(1 - t^2)$. Fig. 50(a) compares mean field results for $M(T)$ in the classical, spin only, and total angular momentum representations. Fig. 50(b) shows mean field results for $M(T)$ taking into account the disorder induced fluctuations in the exchange parameter in hypothetical amorphous alloys. This construction then predicts a quite remarkable change in the mean field theory thermomagnetic response for amorphous magnets.

Recently, the temperature dependence of the magnetization for $Fe_{88}Zr_7B_4Cu_1$ amorphous alloy has been measured by Gallagher et al. [61]. A two-parameter exchange fluctuation mean field theory is shown to give significantly better fits than the single parameter Handrich–Kobe model to $M(T)$ for these amorphous alloys. The deviation in atomic nearest neighbor (NN) distances in an $Fe_{88-x}Co_xZr_7B_4Cu_1$ amorphous alloy was estimated from X-ray scattering data. The Bethe–Slater curve was used to estimate fluctuations in the exchange interaction. An explanation for the relative invariance of $M(T)$ in disordered Co-based alloys as compared with Fe-based alloys was proposed and good qualitative agreement of the model and experimental data was demonstrated. The modification made to the Handrich–Kobe equation allowed for two δ-parameter, δ_+ and δ_-. The new equation being:

$$m(T) = \frac{1}{2}\Big(B_S\big[(1 + \delta_+ x)\big] + B_S\big[(1 - \delta_-)x\big]\Big), \tag{48}$$

where δ_+ and δ_- are not necessarily the same and therefore can act as a first order fit to an asymmetric distribution function.

Fig. 51(a) illustrates typical synchrotron X-ray data for one of the $Fe_{88-x}Co_xZr_7B_4Cu_1$ amorphous alloys and raw $M(T)$ data. The average deviation in atomic nearest neighbor distances in amorphous alloys has been estimated from X-ray scattering data. The Fe–Fe average nearest neighbor distance was estimated to be: $D_{Fe-Fe} = (1.23\lambda)/(2\sin\theta)$ where θ is taken to be the angle at the center of the amorphous peak, and the factor 1.23 is a geometric factor which rationalizes the nearest neighbor distance with the spacing between 'pseudo-close packed planes' [77]. The fluctuations in the Fe–Fe average nearest neighbor distance were estimated and the analysis reveals $D = 2.53$ Å and $\Delta D_+ = 0.17$ Å and $\Delta D_- = 0.13$ Å. The Bethe–Slater curve was then used to estimate fluctuations in the exchange interaction (see Fig. 5). The average atomic separation, based on the position of the center of the amorphous scattering peak, is divided by the appropriate diameter of the Fe 3d orbital for estimating J_{ex} from the Bethe–Slater curve. The fluctuation in the interatomic spacing allows us to estimate the resulting fluctuation in J_{ex}. This is a zeroth order approach, but sufficient for illustration. A more rigorous quantitative analysis would use the scattering peak to determine the

radial distribution function and then use the radial distribution function to arrive at the distribution function [84,86] for the exchange energies. However, given the uncertainty in the exact functional form of the Bethe–Slater curve this extra level of detail seems unjustified.

The improvement of fits to $M(T)$ in the literature using a temperature

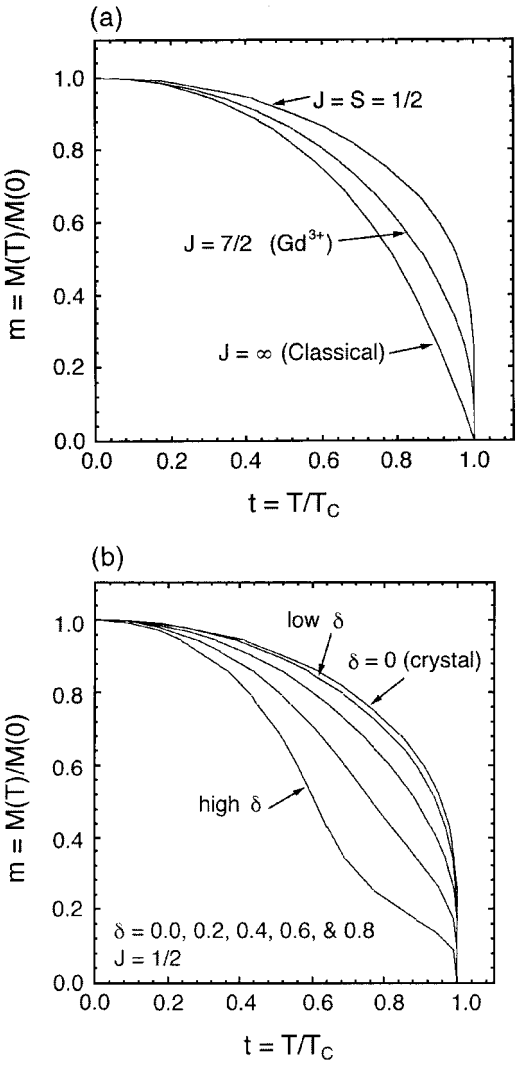

Fig. 50. Comparison of magnetization as a function of reduced temperature, t (a) in a spin only ferromagnet (using a $J = 1/2$ Brillouin function), for $J = 7/2$ and for the classical limit $J = \infty$ and (b) in an amorphous magnet with $J = 7/2$ and different values of the exchange fluctuation parameter δ [figures courtesy of Hiro Iwanabe, Carnegie Mellon University and Japan Energy Corporation].

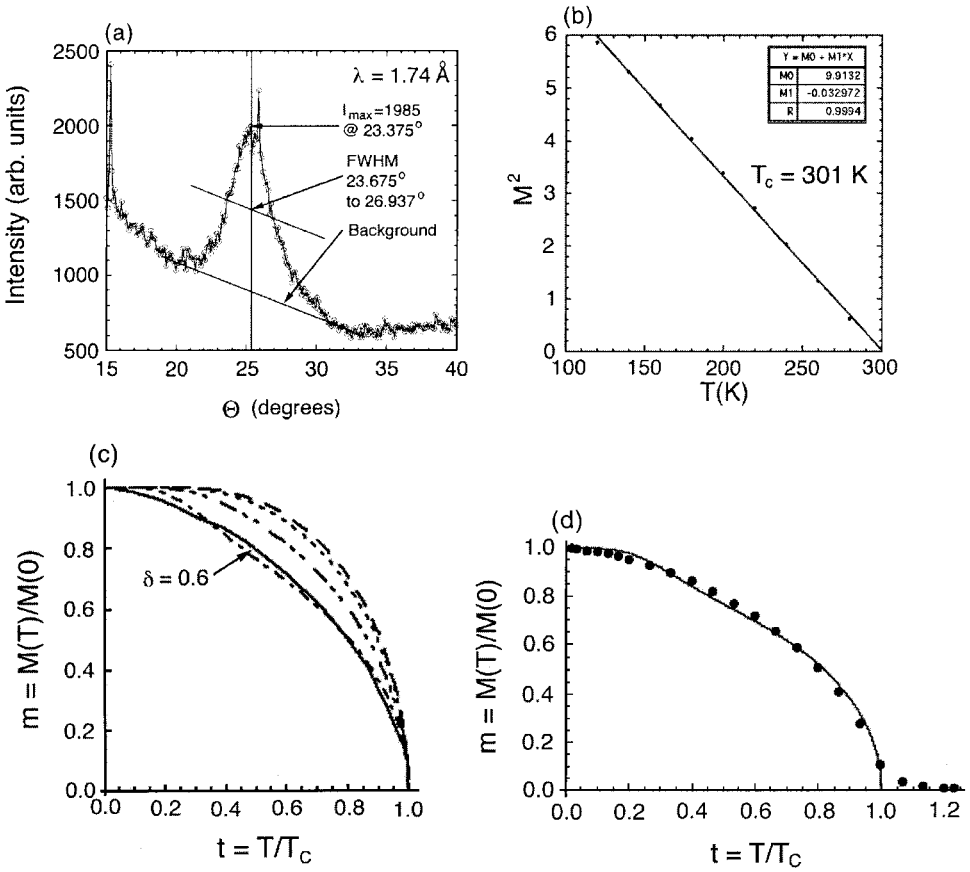

Fig. 51. (a) Synchroton X-ray diffraction data for an amorphous $Fe_8Co_{80}Zr_7B_4Cu_1$ alloy showing broad amorphous scattering peak, peak center and method for determination of full width at half maximum (FWHM). (b) Plot of M^2 vs. T ($H = 1$T used to determine the Curie temperature, T_C. (c) Reduced magnetization, **m**, as a function of reduced temperature, τ_r, an amorphous $Fe_{88}Zr_7B_4Cu_1$ alloy fit with a single δ (data solid line, dashed lines are fits with $\delta = 0{,}0.2$, 0.4, and 0.6, respectively). (d) The same data (solid line) fit with two asymmetric exchange fluctuation parameters, δ_+ and δ_-.

dependent exchange fluctuation term and our improved fits using an asymmetric dependent exchange fluctuation term leads us to conclude that in different alloys systems positional and chemical disorder can have a different relative importance (Fig. 51(c) and (d) [18]). It could then be suggested that a more appropriate parameterization of the exchange fluctuation may consider both asymmetry and temperature dependence of the form:

$$\delta_+ = \delta_+^0 + \delta_+^1\left(1 - \tau_r^2\right)$$

$$\delta_- = \delta_-^0 + \delta_-^1\left(1 - \tau_r^2\right), \tag{49}$$

where the first term reflects chemical and positional disorder and the second thermal disorder. This hypothesis remains to be tested on a variety of amorphous alloys. A more rigorous quantitative analysis would use the scattering peak to determine the radial distribution function and then use the radial distribution function to arrive at the distribution function for the exchange energies. A more quantative analysis of the low temperature magnetization in amorphous Fe-based alloys, based on spin-wave theory, has been reported by Hasegawa [84]. The exchange interactions in amorphous alloys have been determined to be quite short-range so that an analysis of using the radial distribution function should be possible [20,21,85].

6.2.2. Nanocrystalline alloys

In general, the mean field theory used to describe Curie temperatures for nanoparticles is not thought to strongly deviate from that of the bulk materials. This may not be the case in very small nanoparticles where the fraction of surface atomic sites is large. Here the reduced coordination of surface atoms should in fact alter the Curie temperature. For most observations in the literature, however, the T_C does not deviate strongly from that of the bulk materials. An example of $M(T)$ for C-arc produced nanocrystalline Ni is shown in Fig. 52. The T_C of 360°C, for Ni[C] nanocrystals is in excellent agreement with that of bulk Ni [202]. $M(T)$ for Fe nanoencapsulates has also been reported by Hihara et al. [109]. Here, $M(T)$ is complicated by the existence of iron carbides (notably cementite, Fe_3C) and small amounts typically a very small amount of the γ-phase. The γ-phase is non-magnetic and the α-phase and Fe_3C phases have Curie temperatures of 1040 K and ~480 K, respectively. Host et al. [119] have inferred a T_C of 1366 K for Co[C] nanoparticles, from fits of $M(T)$ data, in good agreement with the 1388 K value for bulk Co.

It is noted that in nanocrystalline materials with two phase microstructures the Curie temperature of the nanocrystalline phase and that of the intergranular phase are both important parameters in describing the magnetic response. The intergranular phase which is typically richer in non-magnetic species can have a suppressed magnetic order parameter and lower Curie of γ-Fe. It is typical for α-Fe to be the prominent phase, along with second phase carbides and temperature than the nanocrystals. This is especially important in describing the temperature dependence of a variety of extrinsic magnetic properties as will be discussed in Section 7.

Yoshizawa [290,291] original work on FINEMET alloys reported B_s values of 1.0–1.2 T, which increased with respect to the parent amorphous phase. This increase in induction can be understood in terms of the segregation of moment suppressing early transition metal (e.g. Nb) and some Si to the grain boundaries during the primary crystallization of the α-FeSi phase. This preferential segregation of non-magnetic species to the grain boundary phase can also have deleterious effects if not optimized. As discussed below the nature of the coupling

in nanoparticle–amorphous phase–nanoparticle couples is of paramount importance to the ultimate soft magnetic properties. This coupling is reduced or destroyed above the Curie temperature of the amorphous phase, T_C^{am}. As non-magnetic segregants undoubtedly suppress T_C^{am} careful compositional control is important.

Gorria et al. [71] have studied the temperature dependent magnetization of amorphous and nanocrystalline $Fe_{86}Zr_7Cu_1B_6$ alloys. Fig. 53 illustrates $M(T)$ curves of asquenched and annealed samples as compared with the magnetic response of pure α-Fe. $M(T)$ is particularly useful in identifying the changes in the magnetic response which accompany changes in structure due to the crystallization process. A Curie temperature of 333 ± 5 K is observed for the as-quenched amorphous phase. After crystallization a composite $M(T)$ reflects contributions from α-Fe nanocrystallites, with a Curie temperature approximately that of pure bulk Fe and the intergranular amorphous phase with a substantially lower Curie temperature. The alloy dipole moment increases slightly with

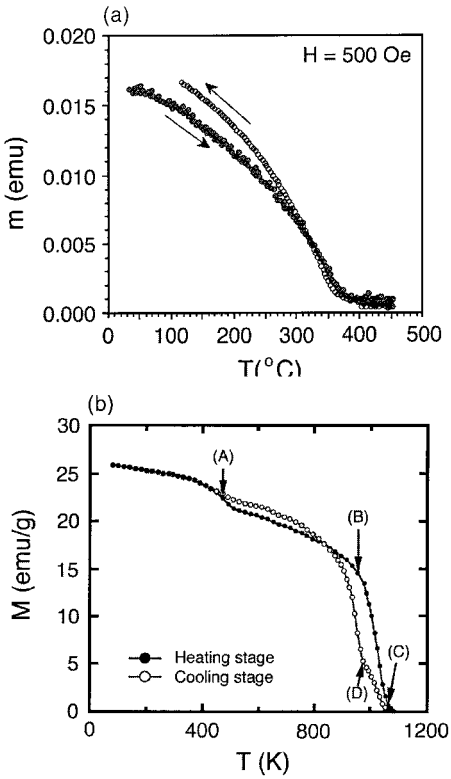

Fig. 52. Magnetic moment vs. T for Ni[C] nanocrystals produced by C-arc synthesis [202] and for Fe-containing nanoencapsulates [109] showing T_C of Fe_3C (A) and α-Fe (C) (B is $\alpha \rightarrow \gamma$ and C is $\gamma \rightarrow \alpha$ phase transition.

crystallization due to the partitioning of the moment reduction from B and Zr to the intergranular phase. The observed Curie temperature of the intergranular amorphous phase to remain relatively invariant during the crystallization process. This amorphous phase Curie temperature is however only ~340°C.

Slawska-Waniewska and Zuberek [254] have measured the temperature dependence of the magnetization for $Fe_{93-x}Zr_7B_x$ and $Fe_{93-x}Zr_7B_xCu_2$ ($x = 4$–14) alloys. These alloys showed clear departures from a simple Brillouin function with a single exchange parameter. This temperature dependence is illustrated in Fig. 54 is quite similar to that observed for Fe–Ni crystalline Invar alloys. This $M(T)$ behavior was attributed to large fluctuations in the Fe–Fe exchange interaction in both of these structurally disordered alloy systems. In crystalline Fe–Ni the distributed exchange results from distributed Fe–Fe interactions resulting from randomly substituted Ni atoms. In the amorphous Fe–Zr–B (Cu) alloys both chemical and positional disorder contribute to the random exchange.

Vojtanik et al. [278,279] have measured intrinsic magnetic properties and magnetic after-effects in Fe–Ni–Zr–Cu–B amorphous alloys. They investigated $Fe_{86-x}Ni_xZr_2Cu_1B_6$ alloys with ($x = 0$–86) Ni additions caused an increase in the Curie temperature from 71 to 373°C at the $x = 43$ compositions with a subsequent decrease for $x > 43$. The $Ni_{86}Zr_7Cu_1B_6$ alloy exhibited paramagnetic response at room temperature.

Fig. 55 shows observations of magnetization as a function of temperature [284]

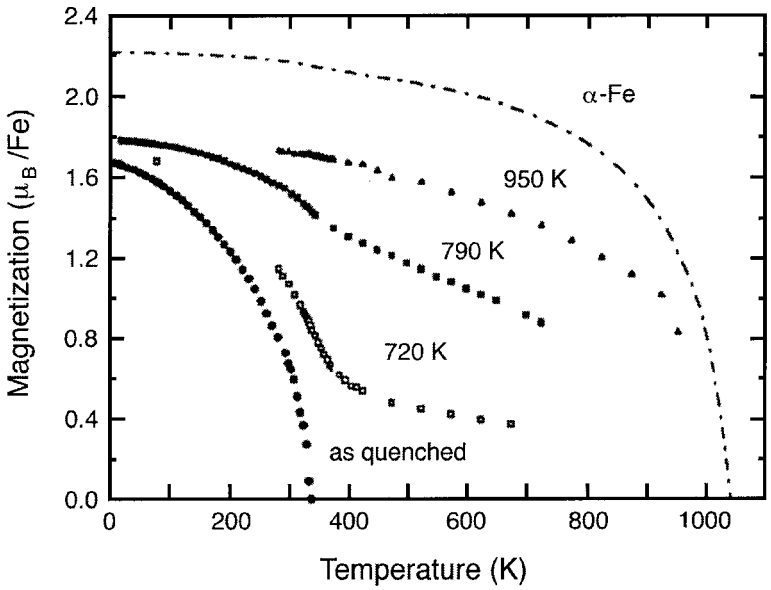

Fig. 53. $M(T)$ for an alloy with a NANOPERM composition $Fe_{88}Zr_7B_4Cu$, as-quenched and annealed (annealing temperatures noted) and for comparison $M(T)$ for α-Fe [71].

for two alloys, one of a NANOPERM composition and the other of a HITPERM composition. Initially, both of the samples are amorphous and as the samples are heated, the crystallization of the amorphous phase (~500°C) becomes apparent in each alloy. The NANOPERM material, shows the Curie temperature of the amorphous phase in the alloy to be just above room temperature. The magnetic phase transition is followed by primary crystallization at $T_{x1} \sim 500$°C. This is followed by secondary crystallization and then finally the magnetic phase transition for the α-Fe phase at ~770°C. The so-called re-enterant ferromagnetism is observed in amorphous alloys with primary crystallization temperatures above the Curie temperature of the amorphous phase.

Fig. 55 ($M(T)$ curve for HITPERM), shows that the magnetization decreases monotonically until ~400°C as the amorphous phase approaches its Curie temperature. Above 400–500°C structural relaxation and crystallization of the α′-FeCo phase occurs resulting in larger magnetization presumably due to the larger Curie temperature of the α′-FeCo phase. The crystallization temperature is apparently well below the Curie temperature of the amorphous phase, so that the magnetization of the amorphous phase is only partially suppressed prior to crystallization. At a temperature corresponding to the $\alpha \rightarrow \gamma$ phase transition (980°C), the material abruptly loses its magnetization consistent with the paramagnetic response of the γ-phase. The Curie temperature of the amorphous intergranular phase in nanocrystalline two-phase materials is extremely important to the exchange coupling of the nanocrystals, as will be discussed further in Section 7.

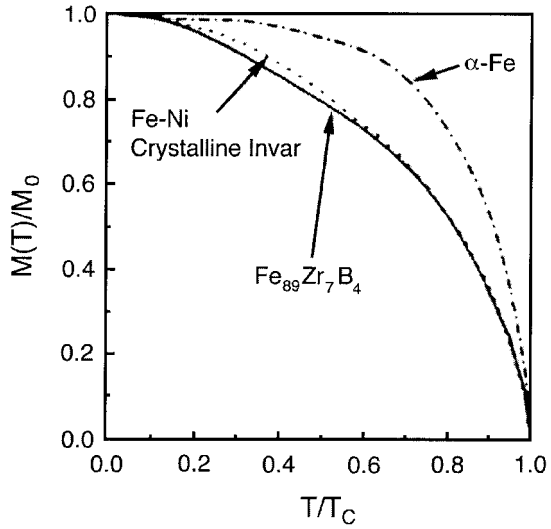

Fig. 54. $M(T)$ for an alloy with a NANOPERM composition as compared with α-Fe and with Fe–Ni substitutional solid solutions [254].

7. Extrinsic magnetic properties

7.1. Magnetic anisotropy and magnetostriction

7.1.1. Amorphous alloys

The discussion of an effective magnetocrystalline anisotropy in both amorphous and nanocrystalline materials is deeply rooted in the notion of a random local anisotropy as presented by Alben et al. [2,3]. The original basis for this model is in the work of Harris [82] who looked at the problem of averaging over randomly oriented local anisotropy axes. The random anisotropy model leads to a small effective magnetic anisotropy due to the statistical averaging (i.e. through a random walk) of the magnetocrystalline anisotropy. In amorphous alloys the notion of a crystal field (which determined K in crystalline materials) is replaced by the concept of a short-range local field on the scale of several Å. The symmetry of the local field determines the local magnetic anisotropy, $K_l(\mathbf{r})$. The symmetry of the local field in amorphous alloys depends on local coordination and chemical short-range order. The local anisotropy may in fact be large but is averaged out due to fluctuations in the orientation of easy axes. The statistical averaging of the local anisotropy takes place over a length scale equivalent to the ferromagnetic exchange length length, L_{ex}.

As in the macroscopic picture of a domain wall, presented in Section 2, the local anisotropy correlation length is determined by a balance of exchange and anisotropy energy densities. Considering these two terms in the previously described magnetic Helmholtz free energy (i.e. ignoring field and demagnetization terms) F_v can be expressed as:

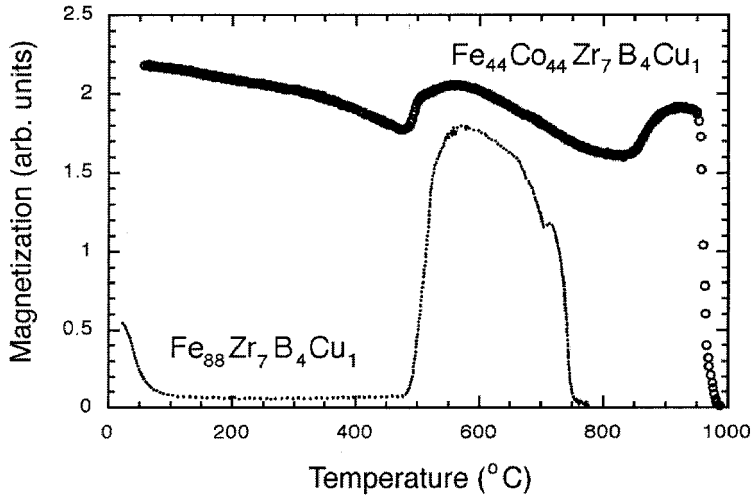

Fig. 55. $M(T)$ for an alloy with a NANOPERM composition $Fe_{88}Zr_7B_4Cu$ and an alloy with a HITPERM composition, $Fe_{44}Co_{44}Zr_7B_4Cu$ [284].

$$F_v = A[\nabla \mathbf{m}]^2 - K_1[\mathbf{m} \cdot \mathbf{n}]^2 \tag{50}$$

where $A = A(\mathbf{r})$ is the local exchange stiffness, $\mathbf{m} = \mathbf{M}(\mathbf{r})/\mathbf{M}_s$ is the reduced magnetization, $\mathbf{n}$ is the local direction of an easy axis, and $K_1 = K_1(\mathbf{r})$ is the leading term in the expansion of the local magnetic anisotropy. If we denote the length scale of chemical or structural fluctuations in the amorphous material as ℓ_s (this will be on the order of 10 Å for a typical amorphous material and nearly equal to the grain size, D_g, in nanocrystalline alloys). For these cases $L_{ex} \gg \ell_s$ (or D_g) in soft materials and a statistical averaging of $K_1(\mathbf{r})$ over a volume of $\sim L_{ex}^3$ is warranted. Considering a random walk through a volume L_{ex}^3 which samples all local anisotropies leads to a scaling of $K_1(\mathbf{r})$ by $(L_{ex}/\ell_s)^{3/2}$ to arrive at an effective anisotropy K_{eff}. This scaling is responsible for the substantial reduction of the magnetic anisotropy in amorphous alloys. In TM-based amorphous alloys where $K_1(\mathbf{r})$ is small to begin with and $L_{ex} \gg \ell_s$ then K_{eff} is very small in good agreement with experimental observations for amorphous transition metal alloys. On the other hand for amorphous rare earth based materials where $K_1(\mathbf{r})$ is large and L_{ex}^3 may sample only a few fluctuations in $\mathbf{n}$ then K_{eff} can still remain quite large [2,3,82,83]). Amorphous rare earth (or rare earth transition metal) alloys with substantial coercivities are observed often.

7.1.2. Weakly exchange coupled nanocrystalline alloys

Magnetic permeability of loose powders and compacts that are not fully dense are dependent on geometry and porosity. This is also the case in alloys produced from amorphous precursors which are not optimally coupled, because of too low a volume fraction of the nanocrystalline phase, for example. Low values of initial permeabilities in non-optimally compacted materials are believed to be due to residual porosity. Since the permeability of a magnetic core is reduced as a result of air gap, then the loss factor is reduced proportionally, one can infer that high loss peak frequencies are influenced by porosity. The relative importance of the porosity and a resistive intergranular phase is still an open question. As shown schematically in Fig. 56, changes in permeability can be imagined as a function of sample porosity.

7.1.3. Strongly exchange coupled nanocrystalline alloys

In a discussion of the benefits of nanocrystalline alloys for soft magnetic applications the extrinsic properties the coercivity and the permeability need to be considered. Reduction of coercivity and the not unrelated increase in permeability are both desirable properties that can be found in select amorphous and nanocrystalline alloys.

The concept of a magnetic exchange length and its relationship to the domain wall width and monodomain size is important in the consideration of magnetic anisotropy in nanocrystalline soft magnetic materials [16]. As described above, these can be defined by appealing to a Helmholtz free energy function as described by Coey [37]. These length scales again are:

$$\delta_w = \pi\sqrt{\frac{A}{K}}, \quad \text{and} \quad L_{ex} = \sqrt{\frac{A}{4\pi M_s^2}} \tag{51}$$

The extension of the random anisotropy model by Herzer [100–107] to nanocrystalline alloys has also been used as the premise for explaining the soft magnetic properties of these materials. The Herzer argument for effective anisotropies in nanocrystalline materials builds on the arguments of the random anisotropy model presented for amorphous alloys presented above. Herzer considers a characteristic volume whose linear dimension is the magnetic exchange length, $L_{ex} \sim (A/K)^{1/2}$ (Fig. 57). Given the discussion above the unstated constant of proportionality should be κ/π which for materials with very small K can in fact be quite large. Ignoring this constant of proportionality, the Herzer argument

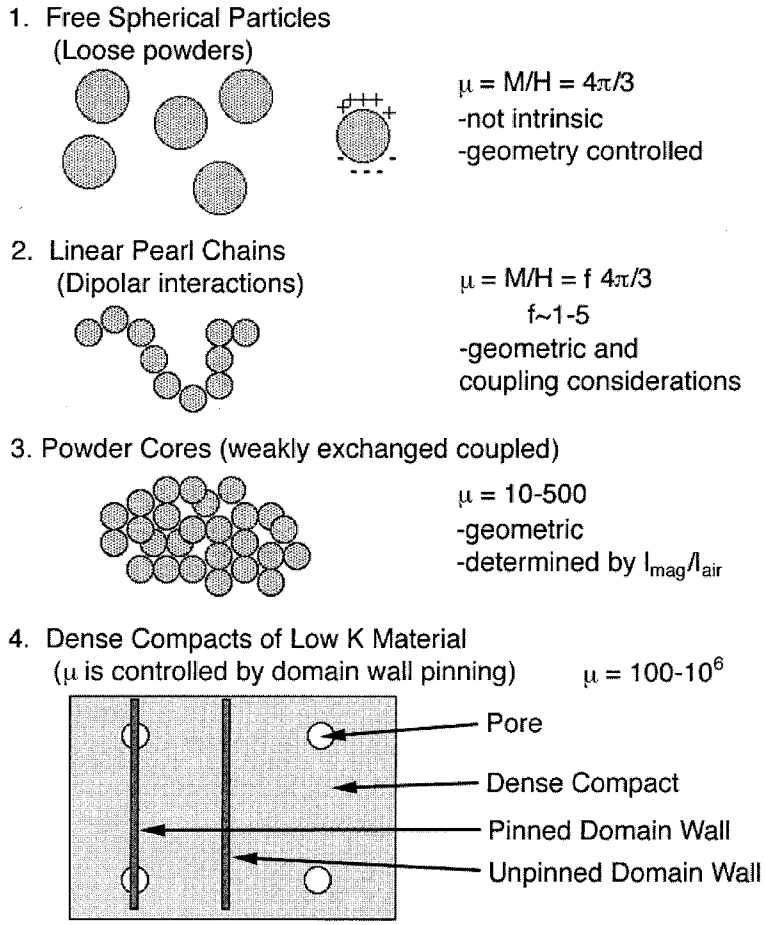

Fig. 56. Schematic representation of permeability as a function of compact density.

considers N grains, with random easy axes, within a volume of L_{ex}^3 to be exchange coupled. Since the easy axes are randomly oriented, a random walk over all N grains will yield and effective anisotropy which is reduced by a factor of $1/(N)^{1/2}$ from the value K for any one grain, thus $K_{eff} = K/(N)^{1/2}$. Now the number of grains in this exchange coupled volume is just $N = (L_{ex}/D)^3$, where D is the average diameter of individual grains. Treating the anisotropy self-consistently, then:

$$K_{eff} \sim KD^{3/2} \sim \left(\frac{K_{eff}}{A}\right)^{3/2} \sim \left(\frac{K^4 D^6}{A^3}\right) \tag{52}$$

Since the coercivity can be taken as proportional to the effective anisotropy, this analysis leads to Herzer's prediction that the effective anisotropy and therefore the coercivity should grow as the 6th power of the grain size:

$$H_c \sim H_K \sim D^6 \tag{53}$$

For such a reduction in the coercivity to be realized, Herzer noted that the nanocrystalline grains must be exchange coupled. This is to be contrasted with uncoupled particles that have an exchange length comparable to the particle diameter and are susceptible to superparamagnetic response. These coupling ideas will be developed more thoroughly in a later section.

Other functional dependences of the coercivity on grain size have been proposed for systems with reduced dimensionality in the literature and supported by experimental observations. Hoffmann and Fujii [114] have modeled the domain wall contribution to coercivity, H_W, showing it to depend on a ripple parameter and a uniaxial magnetic anisotropy. Hoffmann and Fujii point out that the coercivity, H_c could in fact be controlled by one of three different mechanisms. These are:

1. The reverse domain nucleation field, H_N

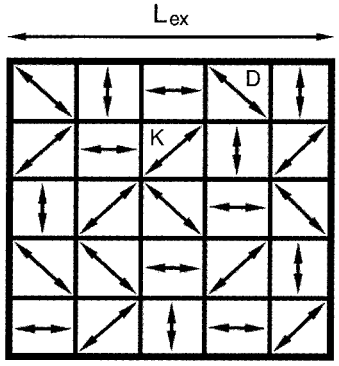

Fig. 57. Cartoon illustrating N nanocrystalline grains of dimension D in a volume L_{ex}^3 [104].

2. The field, H_G, at which the domain walls begin to grow or
3. The field at which the domain walls become mobile, H_W, the wall coercivity.

The coercivity is given by the largest of these three fields. The distinction between mechanism (2) and (3) is not developed fully.

In prior work by Hoffmann [111–113,140] a ripple theory of the static (DC) wall coercive force, H_W was offered for soft magnetic thin films. Like the Herzer theory, which followed years later, the Hoffmann model considered local fluctuations in the wall energy resulting from averaging of the anisotropies of crystallites which are included in the wall volume. He defines a ripple parameter, S, for the magnetic anisotropy as:

$$S = \frac{K_l D}{\sqrt{n}}\sigma \tag{54}$$

where $\sigma \sim 1$ is a numerical factor, D is the grain diameter and n is the number of grains in a characteristic film dimension, ($n = 1$ for columnar films and $n = t/D$ for films of thickness, t, and equiaxed grains). His expression for this wall coercivity, to within a factor on the order of 1, is given by:

$$H_W \sim \left(\frac{2}{\pi}\right)^{1/2} \frac{S}{M_s}\left(\frac{D}{\delta_W}\right)^{1/2} \times \frac{1}{L_{ex}} \tag{55}$$

where L_{ex} is the exchange length parallel to the film. Using expressions (53) and (54) the dependence of H_W on D was inferred for both polycrystalline and columnar thin films, respectively:

$$H_W \sim \frac{D^2}{M_s t^{1/2}}(K_u)^{1/4} \quad \text{Polycrystalline}$$

$$H_W \sim \frac{D^{3/2}}{M_s}(K_u)^{1/4} \quad \text{Columnar grains} \tag{56}$$

Notice that this model pertains to thin film systems with reduced dimensionality such that $t < L_{ex}$.

The original random anisotropy model of Alben addressed a chemically homogeneous amorphous phase. The extension of Herzer to address nanocrystalline materials [102] also treated A and K_l to be those of a single phase though $K_l(\mathbf{r})$ was spatially varying due to random easy axes. Herzer [106,107] extended his model to explicitly address the problem of two-phase microstructures characteristic of FINEMET materials. For a multiphase materials the effective anisotropy is expressed as:

$$D_{eff} = \left(\sum_i \frac{X_i D_i^3 K_i^2}{A^{3/2}}\right)^2 \tag{57}$$

where the sum is over the i phases in the material. In FINEMET $K_{am} \ll K_{BCC}$ and the simple two-phase nanocrystalline materials have an effective anisotropy given by:

$$K_{eff} \sim (1 - X_{am})^2 \frac{K_1^4 D^6}{A^3} \tag{58}$$

that applies only if X_{am} is small. This simple expression predicts a dilutional effect due to the amorphous phase.

Observations of a D^n power law dependence of H_c in nanocrystalline materials with $n < 6$ have been noted in the literature [58,263,264]. Unlike the FINEMET-type Fe–Si–B–M–Cu alloys, the coercivities of NANOPERM type Fe–Zr–B–(Cu) [276] and Fe–P–C–Ga–Si–Cu [61] follow a simpler D^3 power law. This power law dependence has been explained by Suzuki et al. [264–266] as an extension of Herzer's model considering the additional effect of a more long-range uniaxial anisotropy (K_u), i.e. with an interaction length scale $> > L_{ex}$. Under these conditions the effective anisotropy can be written as:

$$K_{eff}^{TOT} = \sqrt{\left(K_u^2 + K_{eff,nc}^2\right)} \tag{59}$$

where $K_{eff,nc}$ is the effective anisotropy of the nanocrystalline material in the absence of the additional uniaxial anisotropy, i.e. as originally expressed by Herzer. Inserting the Herzer expression into Eq. (59) yields:

$$K_{eff}^{TOT} = \left(K_u^2 + \frac{K_1^2 D^3 \left(K_{eff}^{TOT}\right)^{3/2}}{A^{3/2}}\right)^{1/2} \tag{60}$$

that cannot be solved analytically but in the limit $K_u \gg K_{eff,nc}$ reduces to:

$$K_{eff}^{TOT} = K_u + \frac{1}{2}\left(\frac{\sqrt{K_u} K_1^2 D^3}{A^{3/2}}\right)$$

$$= a + bD^3 \tag{61}$$

as is experimentally observed (Fig. 58). These macroscopic uniaxial anisotropies can be attributed to the effects of induced anisotropy due to the domain structure produced during annealing or due to magnetoelastic interactions. Suzuki et al. [276] have proposed a modification of the random anisotropy model for lower dimensional systems where the coercivity is expected to scale as:

$$H_c \sim K\left(\frac{D}{\sqrt{A/K}}\right)^{2n/(4-n)} \tag{62}$$

where A is the exchange stiffness and n is the dimensionality of the exchange coupled region.

The two-phase model of the effective anisotropy of Herzer, explicitly deals with the case that the exchange stiffness of the two phases (in the FINEMET case A_{am} and A_{cr}) are of comparable magnitude. Suzuki and Cadogan [267] have extended the two-phase random anisotropy model to consider the more realistic case that $A_{am} < A_{cr}$. In this model the effective anisotropy was expressed as:

$$K_{eff} \sim \frac{1}{\phi^6}(1 - X_{am})^4 K_1^4 D^6 \left(\frac{1}{A_{cr}^{1/2}} + \frac{(1 - X_{am})^{-1/3} - 1}{A_{am}^{1/2}} \right)^6 \tag{63}$$

where ϕ is a parameter reflecting the symmetry of K_{eff} and the spin rotation angle over L_{ex}. In Herzer's model $\phi \sim 1$.

Saturation magnetostriction constants, λ_s, for nanocrystalline alloys have been discussed by Herzer [103]. He suggests that λ_s is determined by a balance between contributions of the crystallites and that of the amorphous matrix. When $\lambda_{cr} < 0$ and $\lambda_{am} > 0$, a very small composite λ can be achieved. Herzer proposed a simple

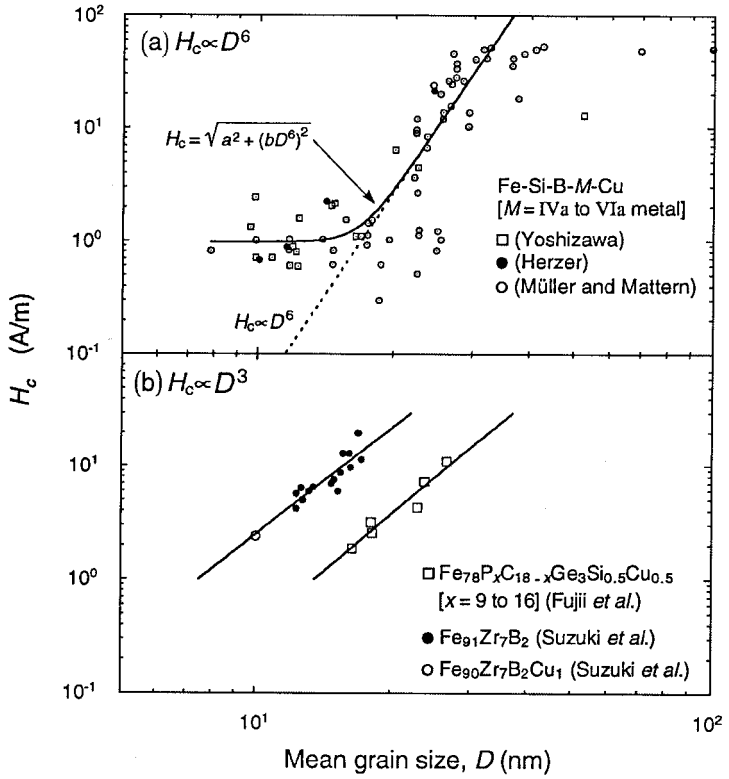

Fig. 58. Coercivity, H, vs. grain size for (a) Fe–Si–B–TE–Cu (TE = early transition metal) (FINEMET) and (b) Fe–Zr–B–Cu (NANOPERM) and Fe–P–C–Ge–Si–Cu alloys [264–266].

two-phase model for the saturation induction and the saturation magnetostriction, which are predicted from a simple rule of mixtures [100,101].

7.2. Induced anisotropies

Induced magnetic anisotropy is observed after annealing in a magnetic or stress field or in the presence of an electrical current for example. There are several proposed mechanisms for this induced anisotropy which include:

1. atomic pair ordering resulting in directional order in the sample [59];
2. induced texturing which line up easy axes;
3. structural relaxation and rearrangement of free volume in amorphous materials;
4. influence over the shape anisotropy of crystallites due to mechanical alignment.

Perhaps the most famous of these is the pair ordering which is thought to be operative in Si–Fe. The remarkable effects of field annealing on the shapes of magnetic hysteresis loops in Si–Fe and many amorphous materials can be related to directional ordering of bond axes and consequently their contributions to the magnetocrystalline anisotropy.

Directional ordering was first addressed in the important work of Néel [215]. In the Néel model of magnetocrystalline anisotropy, the anisotropy for a given bond is expanded in polynomials of the $\cos\theta$ where θ is the angle between the bond axis and the direction of the magnetization:

$$w_i = g(R) + l(R)\left(\cos^2\theta - \frac{1}{3}\right) + q(R)\left(\cos^4\theta - \frac{6}{7}\cos^2\theta + \frac{3}{35}\right) + \cdots \tag{64}$$

where w is the anisotropy energy density contribution of a pair of atoms separated by R, l is a dipolar and q a quadrupolar term in the energy expansion. To determine the magnetocrystalline energy density K, this pairwise interaction energy is summed over all pairs. This summation is typically limited to nearest neighbor pairs since the interactions are short range. This summation will be different for ordered, disordered and directionally ordered materials that are illustrated in Fig. 59.

Fig. 60 shows dramatically the influence of field annealing and consequent directional ordering on the magnetic properties of FINEMET ribbons. Hysteresis loops for FINEMET alloys without and with field annealing in either the longitudinal or transverse directions with respect to the ribbon axis are shown. A squarer hysteresis loop is observed for longitudinally field annealed materials.

Gonzalez et al. [69] have examined the influence of Joule heating anneals with simultaneous application of mechanical stress on the effective anisotropy and magnetostriction of $Fe_{73.5}Cu_1Ta_3Si_{13.5}B_9$ amorphous alloys (a FINEMET composition). A maximum in the uniaxial magnetic anisotropy K_u occurred at an annealing temperature of 450°C and was correlated with initial crystallization. At larger temperatures K decreases as the nanocrystal spacing decreases and the magnetic coupling increases. The stress dependence of the magnetization work

allowed for the separate determination of the magnetostrictive coefficients of the amorphous and nanocrystalline phases.

Hoffmann and Kronmuller [115] have shown the evolution of magnetization curves for FINEMET materials with and without induced transverse anisotropy. Annealing of amorphous and nanocrystalline ribbons (of the FINEMET composition) under the influence of a mechanical stress was shown to yield a creep induced transverse magnetic anisotropy. They concluded that the induced anisotropy was responsible for these effects.

Murillo et al. [211] have studied the dependence of coercivity and remnant magnetization as a function of annealing time for $Fe_{77.5}Si_{13.5}B_9$, $Fe_{76.5}Cu_1Si_{13.5}B_9$ and $Fe_{74.5}Ta_3Si_{13.5}B_9$ alloys. Annealing was performed by current application both with and without the application of a simultaneous tensile stress. Induced (stress) anisotropy promotes the evolution of the remnant magnetization.

Zuberek [306] has used current densities of 5000–7500 A/cm^2 during annealing to improve the magnetic permeability of these alloys. Park et al. [224] have annealed <10 nm thick ribbons of $Fe_{78}Al_4B_{12}Nb_8Cu_1$ and $Fe_{83}B_9Nb_7Cu_1$ in transverse magnetic fields. Large effective permeabilities and small core losses up to 1 MHz were observed for optimally annealed samples. The alloy with A1 additions showed larger improvements with field annealing and exhibited better high frequency soft magnetic properties.

7.3. Magnetic coupling in two phase microstructures

As discussed previously and illustrated below, the Herzer [102–107] model describes coercivity data in many nanocrystalline alloys quite well. However, two conditions are required for his model to have validity: (1) the grain size must be smaller than the magnetic exchange correlation length and (2) the grains must remain ferromagnetically coupled. In a single phase nanocrystalline alloy, as long as the first criterion is met and the alloy is below the Curie temperature the model

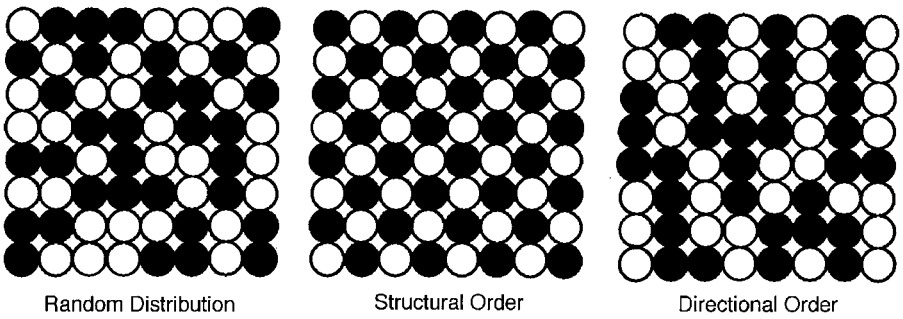

Fig. 59. Schematic of A (filled) and B (open) atom distributions in (a) a disordered (random), (b) a structurally ordered and (c) a directionally ordered AB alloy.

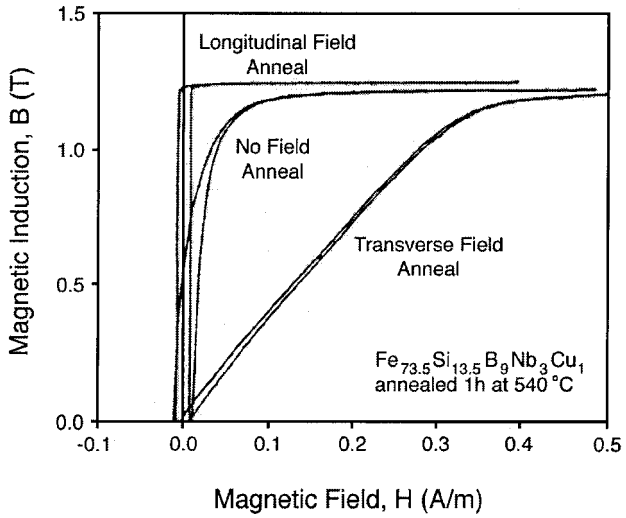

Fig. 60. Hysteresis loops for FINEMET alloys without and with field annealing in either the longitudinal or transverse directions with respect to the ribbon axis [103].

holds. This is not necessarily the case for a multiphase system such as we find in many of the nanocrystalline alloys that are produced from amorphous precursors.

For a two-phase microstructures with a ferromagnetic intergranular amorphous phase and a single ferromagnetic nanocrystalline phase, the nature of the nanocrystal-amorphous-nanocrystal coupling is of paramount importance to the properties of these materials. This coupling depends upon the size of the nanocrystallites, and more importantly upon the amount, chemistry, and thickness of the amorphous phase. The best properties, of course, are when both criteria are met, below the presumably lower Curie temperature of the amorphous phase.

Deviations of the reduced coercivity from values predicted by the random anisotropy model were first measured at temperatures near or higher than the Curie temperatures of the amorphous phase [100]. The decrease in coupling of the ferromagnetic nanocrystal grains through the amorphous phase was directly correlated with the coercivity increase. This finding became the basis of many studies to probe the limits of nanocrystalline alloys which contained very small grains or well spaced grains in an amorphous matrix.

Slawska–Waniewska et al. [251,252] have observed T-dependent magnetic response in partially and fully nanocrystallized FINEMET materials. They concluded that for sufficiently small nanocrystals with enough intergranular material between them to diminish or destroy coupling between grains that superparamagnetic response would be observed. This would not be the case for properly annealed samples with sufficient volume fraction of the nanocrystalline ferromagnet. Characteristics of superparamagnetic response, first proposed by Bean [12] include: (1) a Langevin function (H/T) scaling of magnetization data; (2) disappearance of the coercivity above a blocking temperature, and (3) time

dependent magnetization, due to thermally activated switching of the magnetization.

Mazaleyrat et al. [201] have investigated the evolution of magnetic properties over time in an isothermal annealing experiment and in cooling. Fig. 61 shows the progression of the saturation induction, B_s, the magnetic squareness (B_r/B_s) and the coercivity, H_c, during isothermal annealing and subsequent cooling. During the isothermal anneal, it was expected that the crystallization of the amorphous material would yield an increase in the saturation magnetization and the magnetic squareness. A superparamagnetic response was also found upon cooling until the Curie temperature of the amorphous phase was reached and the nanocrystals once again coupled to one another.

Additional work on the superparamagnetism of uncoupled nanoparticles in FINEMET alloys was carried out by Skorvanek and O'Handley [250]. They studied magnetic interactions between nanoparticles above the Curie temperature of the intergranular amorphous phase. They showed that the magnetic interactions increase with increasing nanocrystalline volume fraction. These interactions tend to suppress superparamagnetic fluctuations. They observed a peak $H_c(T)$ near the Curie temperature of the amorphous phase. The increasing branch of these curves were associated with the suppression of the interparticle exchange coupling. Beyond T_C^{am}, $H_c(T)$ decreased in accordance with the predictions of theories of superparamagnetic response.

Hernando et al. [96,106] have elucidated the dependence of spin-spin correlations in FINEMET alloys on the thermal treatment. They examined, in particular, the dependence of the coercivity of the nanocrystalline materials on annealing temperatures (for anneals 1 h in durations) as shown in Fig. 62. They have also examined the temperature dependence of the coercivity after annealing

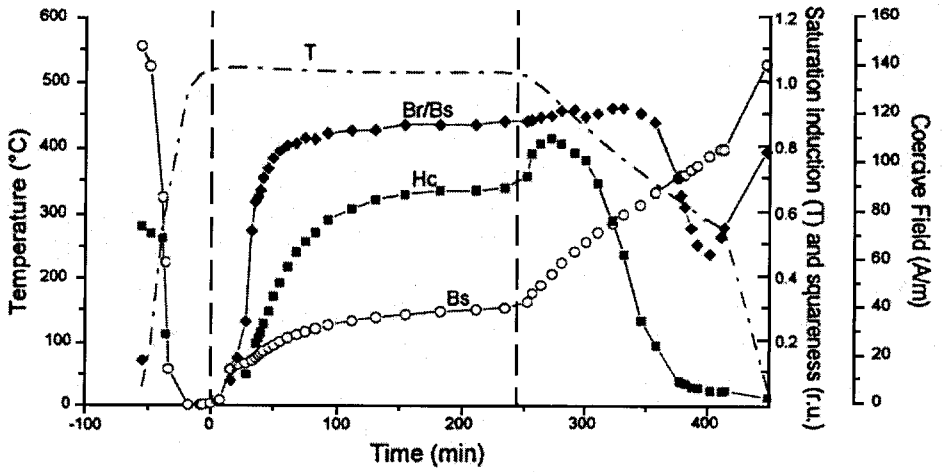

Fig. 61. Evolution of the saturation induction, B_s, the magnetic squareness (B_r/B_s) the coercivity, H_c during isothermal annealing at 500°C and subsequent cooling [201].

for 1 h at various temperatures. A strong annealing temperature dependence of the coercivity suggested an optimal nanoparticle distribution was quite sensitive to crystallization conditions. The temperature dependence of the coercivity suggested hardening through nanoparticle decoupling followed by superparamagnetic response.

Defining a phenomenological parameter, γ, which parameterizes the exchange interaction through the amorphous matrix phase, Hernando [94,95] has developed a model which predicts a peak in $H_c(T)$ at the Curie temperature of the amorphous phase. Further developments of this model are described by Hernando et al. [96,97]. Hernando [96] has found that above $\gamma_{am} \sim 0.85$ the material acts as an assembly of single domain particles that become superparamagnetic about T_c^{am}.

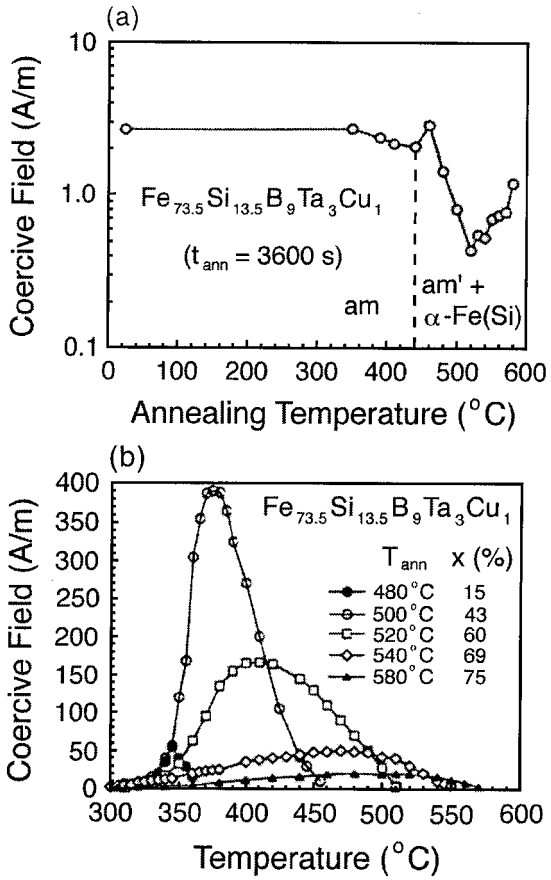

Fig. 62. Dependence of the coercivity of $Fe_{73.5}Cu_1Ta_3Si_{13.5}B_9$ the nanocrystalline materials (a) on annealing temperatures (for anneals 1 h in durations) and (b) on temperature after 1 h anneals at various temperatures [96,97].

Interestingly, the observed Curie temperature, T_C^{am} is nearly 100 K higher than $T_C^{am^*}$, that expected for the amorphous matrix of the same composition in an as cast ribbon. A parameterization of the intergranular spacing, A, is used in a description of the enhancement of T_C^{am} to $T_C^{am^*}$. This intergranular spacing is:

$$\Lambda = d\left[\left(\frac{1}{X}\right)^{1/3} - 1\right] \tag{65}$$

where d is the average grain size and X is the volume fraction of α-Fe nanocrystals. With this parameter defined, a linear dependence has been postulated of the form:

$$T_C^{am} - T_C^{am^*} = \frac{2L}{\Lambda}\left(T_C^{xtal} - T_C^{am^*}\right) \tag{66}$$

with L_{ex} is the exchange correlation length. This result has been attributed to exchange coupling enhancement in the amorphous phase near the interface with the ferromagnetic nanocrystals. This enhancement will only be observable in materials with large surface area/volume ratios.

As mentioned earlier, Hernando [97] has offered a parameterization that describes decoupling of ferromagnetic nanocrystals above the Curie temperature of the amorphous phase. The details of this model involve definition of an exchange correlation length coefficient, γ_{ex}, which has values ranging between zero (decoupled) and one (fully coupled-Herzer model). He has developed relationships for multiphase systems beginning by defining:

$$\gamma_{ex} = \exp\left[\frac{-\Lambda}{L_{am}}\right] \tag{67}$$

where L_{am} is the exchange length of the amorphous phase. Three notable relationships arise:

1. The first of these is a modified exchange correlation length, L^*, expressed as a function of the exchange correlation length coefficient:

$$L^* = \frac{L_{ex}\gamma_{ex}^2}{X} \tag{68}$$

   where L_{ex} is the single phase exchange correlation length originally proposed by Herzer. The dependence of L^* on X profoundly modifies the D^6 dependence of H_c.
2. The second of these is a new parameterization of the magnetocrystalline anisotropy that is also a strong function of the exchange correlation length coefficient:

$$k^* = \frac{K_0 X^2}{\gamma_{ex}^3} \tag{69}$$

where K_0 represents the macroscopic anisotropy and k^* the 'structural' anisotropy. Again, this expression reduces to Herzer's model for $\gamma_{ex} = 1$.

3. Finally, the third relationship describes critical size of crystallities, δ^*, below which a reduction in coercivity due to random anisotropy will be observed. It is:

$$\delta^* = \delta_0 \frac{\gamma_{ex}}{X^{2/3}} \tag{70}$$

where δ_0 is the maximum size of crystallites. In the Herzer model, where $\delta < \delta_0$ then the critical size is independent of the amount of crystalline phase at any temperature. However, in the two-phase model, since δ grows to exceed δ^* (either by increasing temperature or decreasing volume fraction of crystalline material) a variety of experimental results can be explained (i.e. magnetic hardening, etc.).

Gonzalez et al. [70] have investigated extrinsic magnetic properties for small nanocrystalline volume fractions. This work (interpreted in terms of Hoffmann's ripple theory [111–114] has shown that as the fraction of nanocrystallized material increases, the coercivity approaches the Herzer D^6 power dependence. This, as in the results of Hernando, is attributed to enhanced intergranular exchange due to smaller amorphous phase thickness.

Another observed phenomenon, known as magnetic hardening of dilute nanocrystalline alloys, has been observed by Gomez and Polo [68] and Malkinski [196]. These groups have investigated very dilute ($X = 0.15$–0.25) nanocrystalline materials and observed that the grains function as inclusions in an amorphous matrix. They noted that when $L_0 > A$, then the grains are coupled and behave comparably to single phase systems. When the materials are annealed at a temperature near the start of the crystallization peak (as determined by DSC), the coercivity is increased. However, for higher annealing temperatures, this phenomenon is not seen. An explanation offered to explain these results argues that for $\delta > \delta^*$ the grains are decoupled and the magnetization follows the easy axes of individual nanocrystallites thereby increasing the magnetocrystalline anisotropy locally giving rise to higher coercivities.

Gorria et al. [72] have studied critical phenomenon in two-phase nanocrystalline alloys. They found that, due to the exchange penetration, $M(T)$ cannot be described by a simple critical exponent. However, for small volume fractions of nanocrystalline phase, the critical phenomenon is well pronounced [68,94,95]. Suzuki and Cadogan [264,265] have proposed an expression for the critical phenomenon that described the temperature dependence of coercivity quite well. Suzuki's results are summarized by the following equations that are valid near T_C^{am}:

$$M_s^{am}(T) \sim M_0^{am}\left(1 - \frac{T}{T_C^{am}}\right)^{\beta};$$

$$A^{\mathrm{am}}(T) \sim \left(T_{\mathrm{C}}^{\mathrm{am}} - T\right)^{2\beta}; \langle K(T) \rangle \sim \left(T_{\mathrm{C}}^{\mathrm{am}} - T\right)^{-6\beta} \tag{71}$$

The results are interesting in that they pont to directions for improvement of two-phase nanocrystalline alloys. In particular, future improvements may be made by increasing the spontaneous magnetization of the amorphous phase. This is mainly due to the dominance of the exchange stiffness of the amorphous phase, A^{am} in the temperature region below $T_{\mathrm{C}}^{\mathrm{am}}$.

Buttino and Poppi [31] have performed interesting experiments aimed at elucidating the temperature dependence of the magnetic anisotropy in FINEMET alloys. These studies considered materials annealed in zero or finite longitudinal or transverse magnetic fields as well as comparing process induced anisotropies with those induced by applied external stresses. They have used both the temperature dependence of the initial relative permeability (measured) and the saturation magnetization (modeled) and calculated the T-dependence of the magnetic anisotropy constant, $K(T)$ using the relationship:

$$K(T) = \frac{M_{\mathrm{s}}^2(T)}{2\mu_0 \left[\mu_i(T)\right]_{\mathrm{rel}}} \tag{72}$$

Slawska-Waniewska and Greneche [255] have used Mössbauer spectroscopy to study $Fe_{89}Zr_7B_4$ nanocrystalline materials between 4.2 and 550 K. Contributions to the Mössbauer spectra from nanocrystals, amorphous regions and interfaces have all been identified. Interfacial structural and spin-disorder is inferred from the temperature dependence of the mean hyperfine field. The interface between α-Fe nanoparticles and the intergranular amorphous material has its magnetic properties dominated by exchange interactions between the interfacial Fe atoms and those in the bulk of the nanocrystals. Exchange coupling within the amorphous materials was determined to be relatively unimportant to the interfacial properties.

Hernando [98] has extended his two phase effective anisotropy ideas, considering temperature dependent effects. He has shown that that the average local anisotropy changes with temperature as $M_{\mathrm{s}}(T)^n$ with $n > 2$, which allows for a coercive field temperature-dependence for a single-phase system as M_{s}^{4n-7} ($n > 2$). For two-phase materials:

$$H_{\mathrm{c}}^{*}(T) = \frac{k^2 H_C(T)}{\gamma_{\mathrm{ex}}^3} \tag{73}$$

where $H_{\mathrm{c}}(T)$ gives the single-phase dependence. The dependence of γ on temperature is found by considering the temperature dependence of the terms used in the definition of γ_{ex}. In turn, $\gamma_{\mathrm{ex}}(T)$ can be used to determine the temperature dependence of the exchange correlation length charge:

$$L_{\mathrm{am}}(T) = \left[\frac{A_{\mathrm{am}}(T)}{K_{\mathrm{am}}(T)}\right]^{1/2} \sim \left[M'_{\mathrm{am}}(T)\right]^{2-n'/2} \tag{74}$$

where $n' > 2$ and A_{am} and K_{am} are exchange stiffness and magnetic anisotropy, respectively, for the amorphous phase. So when $L_{am} < \delta$, there is decoupling of adjacent grains so that H_c is a maximum at $L_{am} = \delta$. Further increase in temperature should result in monodomain response which for combinations of small particle volumes and magnetic anisotropies leads to superparamagnetic behavior and a characteristic temperature dependence of the coercivity:

$$H_c(T) = \frac{2k}{\mu_0 M_s}\left[1 - \frac{25k_B T}{k\delta^3}\right] \tag{75}$$

for temperatures exceeding the blocking temperature of the particles, T_B.

7.4. Experimental observations in bulk amorphous alloys

Table 7 summarizes experimental observations of intrinsic and extrinsic magnetic properties of bulk amorphous alloys. This includes saturation induction, permeability, coercivity, Curie temperature and magnetostrictive coefficient for these bulk amorphous materials. This data was compiled from a selection of literature sources.

Table 7
Experimental observations of intrinsic and extrinsic magnetic properties of bulk amorphous alloys

Alloy	Reference	T_c (K)	B_s (T)	μ_e ($\times 10^3$)	H_c (A/M)	λ_s (ppm)
$Fe_{72}Al_5Ga_2P_{11}C_6B_4$	[127]					
$Fe_{70}Al_5Ga_2P_{11}C_6B_4Nb_2$	[127]					
$Fe_{68}Al_5Ga_2P_{11}C_6B_4Mo_4$	[127]					
$Fe_{68}Al_5Ga_2P_{11}C_6B_4Cr_4$	[127]					
$Fe_{66}Al_5Ga_2P_{11}C_6B_4Co_6$	[127]					
$Fe_{73}Al_5Ga_2P_{11}C_5B_4$	[130]	~600	1.07	3.6	12.7	
$Fe_{72}Al_5Ga_2P_{11}C_5B_4Si_1$	[130]	~600	1.14	3.2	0.5	
$Fe_{80}P_{12}B_4Si_4$ (aq)	[128]		1.1	5.8	1.3	31
$Fe_{80}P_{12}B_4Si_4$ (ann 723 K)	[128]		1.34	22	1.1	
$Fe_{76}Al_4P_{12}B_4Si_4$ (aq)	[128]		0.96	2.6	12.7	30
$Fe_{76}Al_4P_{12}B_4Si_4$ (ann 723 K)	[128]		1.24	21	2.6	
$Fe_{74}Al_4Ga_2P_{12}B_4Si_4$ (aq)	[128]		0.91	1.9	19.1	21
$Fe_{74}Al_4Ga_2P_{12}B_4Si_4$	[128]		1.14	19	6.4	
$Fe_{72}Al_5Ga_2P_{11}C_6B_4$	[123]	605	1.07	9	5.1	2
$Fe_{74}Al_5P_{11}C_6B_4$	[124]					
$Fe_{72}Al_5P_{11}C_6B_4Ge_2$	[124]	590				
$Fe_{72}Al_5P_{11}C_6B_4Ga_2$	[124]					
$Fe_{73}Al_5Ga_2P_{11}C_5B_4$	[125]	606	1.26		82	
$Fe_{80}P_{11}C_5B_4$	[125]					
$Fe_{75}Al_5P_{11}C_5B_4$	[125]					
$Fe_{78}Ga_2P_{11}C_5B_4$	[125]					
$Fe_{56}Co_7Ni_7Zr_2Nb_8B_{20}$	[167]	508	0.71	18–20	1.7	10
$Fe_{56}Co_7Ni_7Zr_2Ta_8B_{20}$	[167]	538	0.85	17.4	1.5	14
$Fe_{56}Co_7Ni_7Zr_{10}B_{20}$	[132]	567	0.96	17.7	2.4	

Table 8
Experimental observations of primary and secondary crystallization temperatures, saturation induction, permeability, coercivity, Curie temperature, magnetostrictive coefficient and annealing temperatures for nanocrystalline alloys (FINEMET) and amorphous precursors

Sample	T_{x1} (K)	T_{x2} (K)	B_s (T)	μ_e	H_c(A/m)	T_C (K)	λ_s ($\times 10^{-6}$)	T_a (K)	Reference
$Fe_{73.5}Cu_1Nb_3Si_{13.5}B_9$			1.24	100*k*	0.53	843	2.1		[290]
$Fe_{73.5}Cu_1Nb_3Si_{16.5}B_6$			1.18	75*k*	1.1	833	~ 0		[290]
$Fe_{77.5}Si_{13.5}B_9$	808	823		5*k*				693	[216]
$Fe_{74.5}Nb_3Si_{13.5}B_9$	843	873		5*k*				713	[216]
$Fe_{76.5}Cu_1Si_{13.5}B_9$	753	808		3*k*				693	[216]
$Fe_{73.5}Cu_1Nb_3Si_{13.5}B_9$	803	908		12*k*	1.2			843	[216]
$Fe_{71.5}Cu_1Nb_5Si_{13.5}B_9$	805			11*k*		530		840	[294]
$Fe_{73.5}Cu_1W_3Si_{13.5}B_9$	760			7*k*		600		790	[294]
$Fe_{73.5}Cu_1Mo_3Si_{13.5}B_9$	760			7*k*		590		800	[294]
$Fe_{73.5}Cu_1Ta_3Si_{13.5}B_9$	785			4*k*				780	[294]
$Fe_{73.5}Cu_1Cr_3Si_{13.5}B_9$	730	810		500		620		740	[294]
$Fe_{73.5}Cu_1V_3Si_{13.5}B_9$	740	850		750		610		720	[294]
$Fe_{73.5}Cu_1Nb_3B_{22.5}$[a]				4.5*k*				693	[217]
$Fe_{73.5}Cu_1Nb_{35}Si_{4.5}B_{18}$[a]				5.5*k*				733	[217]
$Fe_{73.5}Cu_1Nb_{35}Si_9B_{13.5}$				7*k*				773	[217]
$Fe_{73.5}Cu_1Nb_3Si_{11.25}B_{11.25}$				10*k*		360	5.2	833	[217]
$Fe_{73.5}Cu_1Nb_3Si_{13.5}B_9$				12*k*		360	2.2	843	[217]
$Fe_{73.5}Cu_1Nb_3Si_{15.75}B_{6.75}$				14*k*		590	0.6	833	[217]
$Fe_{73.5}Cu_1Nb_3Si_{18}B_{4.5}$				17*k*		570	0.5	823	[217]
$Fe_{73.5}Cu_1Nb_3Si_{13.5}B_9$	770	906	1.23	35*k*	1.0		2.0	833	[148]
$Fe_{73.4}Al_{0.1}Cu_1Nb_3Si_{13.5}B_9$	773	917	1.10	40*k*	0.88			833	[148]
$Fe_{73}Al_{0.5}Cu_1Nb_3Si_{13.5}B_9$	757	913	1.10	37*k*	0.8			833	[148]
$Fe_{72.5}Al_1Cu_1Nb_3Si_{13.5}B_9$	760	916	1.09	33*k*	0.74		5.0	833	[148]
$Fe_{74.5}Cu_{0.75}Nb_{2.75}Si_{13.5}B_9$				32*k*				823	[238]
$Fe_{77}Cu_1Nb_3B_{19}$	740	850	1.16		106			743	[214]
$Fe_{76}Cu_1Nb_3B_{20}$	758	860							[214]
$Fe_{73.5}Cu_1Nb_3B_{22.5}$	799	848							[214]
$Fe_{71}Cu_1Nb_3B_{25}$	854								[214]
$Fe_{80}B_{20}$	722								[214]
$Fe_{73.5}Cu_1Nb_3Si_{13.5}B_9$					0.7			863	[19]
$Fe_{73.5}Cu_1Nb_3Si_{13.5}B_9$[a]	718	847	0.7		0.5		4	843	[175]
$Fe_{73.5}Cu_1Nb_3Si_{17.5}B_5$[a]	708	888	0.55		1			753	[175]
$Fe_{73.5}Cu_1Nb_3Si_{13.5}B_9$				7*k*	1.4			833	[286]
$Fe_{81.5}P_{12}Cu_{0.5}C_3Mo_{0.5}Si_{2.5}$			1.45	102*k*	6.7			633	[180]
$Fe_{83}Nb_7B_9Cu_1$			1.42	4*k*	2.24			823	[224]
$Fe_{78}Cu_1Nb_5Al_4B_{12}$			1.38	7*k*	0.96			723	[224]
$Fe_{72.7}Cu_1Nb_2V_{1.8}B_9Si_{13.5}$			1.21	81*k*				823	[281]
$Fe_{73.5}Cu_1Nb_3Si_{13.5}B_9$			1.21	92*k*				823	[281]
$Fe_{61}Co_{21}Nb_3B_{15}$	681	858	1.56		298		24.6	823	[172]
$Fe_{59}Co_{21}Nb_5B_{15}$	715	898	1.65		43.5		22.8	873	[172]
$Fe_{57}Co_{21}Nb_7B_{15}$	748	985	1.42		27		21.4	873	[172]
$Fe_{56}Co_7Ni_7Zr_2Nb_8B_{20}$	873	1050	0.71	19.4*k*	1.7	508	10	800	[167]
$Fe_{56}Co_7Ni_7Zr_2Ta_8B_{20}$	874	1080	0.85	17.4*k*	1.5	538	14	800	[167]
$Fe_{73.5}Al_2Cu_1Nb_3Si_{13.5}B_9$			1.3		0.32		10	793	[268]

(continued on next page)

Table 8 (*continued*)

Sample	T_{x1} (K)	T_{x2} (K)	B_s (T)	μ_e	H_c(A/m)	T_C (K)	λ_s ($\times 10^{-6}$)	T_a (K)	Reference
$Fe_{73.5}Cu_1Nb_{35}Si_9B_{13.5}$					13.5		1.94		[297]
$Fe_{73.5}Cu_1Nb_{35}Si_9B_{13.5}$					2			823	[297]
$Fe_{66.5}Co_7Cu_1Nb_{35}Si_9Bi_{13.5}$					10.1		2.16		[297]
$Fe_{66.5}Co_7Cu_1Nb_{35}Si_9B_{13.5}$					2.1			823	[297]
$Fe_{73.5}Cu_1Nb_3Si_{13.5}B_9$	840	980							[78]
$Fe_{72}Cu_1Cr_{1.5}Nb_3Si_{13.5}B_9$	860	985							[78]
$Fe_{69}Cu_1Cr_{4.5}Nb_3Si_{13.5}B_9$	870	1000							[78]
$Fe_{65.5}Cu_1Cr_8Nb_3Si_{13.5}B_9$	910	995							[78]
$Fe_{63}Cu_1Cr_{10.5}Nb_3Si_{13.5}B_9$	940	990							[78]
$Fe_{84}Si_6B_{10}$	693	806		$2k$				473	[212]
$Fe_{83}Si_6B_{10}Nb_1$	723	848		$1.5k$				473	[212]
$Fe_{82}Si_6B_{10}Nb_2$	727	873		$1.45k$				523	[212]
$Fe_{81}Si_6B_{10}Nb_3$	756	889		$5.5k$				523	[212]
$Fe_{80}Si_6B_{10}Nb_4$	798	964		$9k$				548	[212]
$Fe_{79}Si_6B_{10}Nb_5$	823	973		$10k$				573	[212]
$Fe_{78}Si_6B_{10}Nb_6$	844	998							[212]
$Fe_{74.5}Nb_3Si_{13.5}B_9$	863					590			[138]
$Fe_{74}Cu_{0.5}Nb_3Si_{13.5}B_9$	816	965				590			[138]
$Fe_{73.5}Cu_1Nb_3Si_{13.5}B_9$	812	962				595			[138]
$Fe_{73}Cu_{1.5}Nb_3Si_{13.5}B_9$	809	954				595			[138]

[a] Amorphous.

7.5. Experimental observations in nanocrystalline alloys

7.5.1. FINEMET alloys

summarizes experimental observations of primary and secondary crystallization temperatures, saturation induction, permeability, coercivity, Curie temperature, magnetostrictive coefficient and annealing for nanocrystalline alloys (FINEMETS) and amorphous precursors. This data was compiled from a selection of literature sources. In this section, we discuss several pertinent observations made in some of these studies.

Yoshizawa et al. [290,291] have reported a grain size of 10 to 15 nm for FINEMET alloys with attractive soft magnetic properties. These include coercivities of 0.01 Oe and permeabilities of $\sim 10^5$. In premiere soft magnetic materials, in which alloy and microstructural developments aim at eliminating magnetocrystalline anisotropy, it becomes quite important to consider the contribution due to other types of magnetic anisotropy. Important among these are stress or strain (magnetostrictive) induced anisotropy. The best materials have the smallest magnetostrictive coefficients. Substantial reduction of λ_s (from 20 to 3 ppm) on annealing can be explained in terms of the small λ associated with α-FeSi and with regions of $+\lambda$ coupled to regions of $-\lambda$.

Knoble et al. [151] have examined the influence of quench rate on magnetic properties in FINEMET alloys. Disaccommodation, pinning fields and the stress

dependence of the permeability were examined and found to be sensitive to quench rate from the melt. These effects can be attributed to quenched-in internal stress and free volume. Kane et al. [137] have used XRD and Mössbauer spectroscopy to study the quench rate dependence on short-range order (SRO) and internal stresses in amorphous precursors to FINEMET alloys. Samples prepared with smaller quench rates were found to have lower amounts of

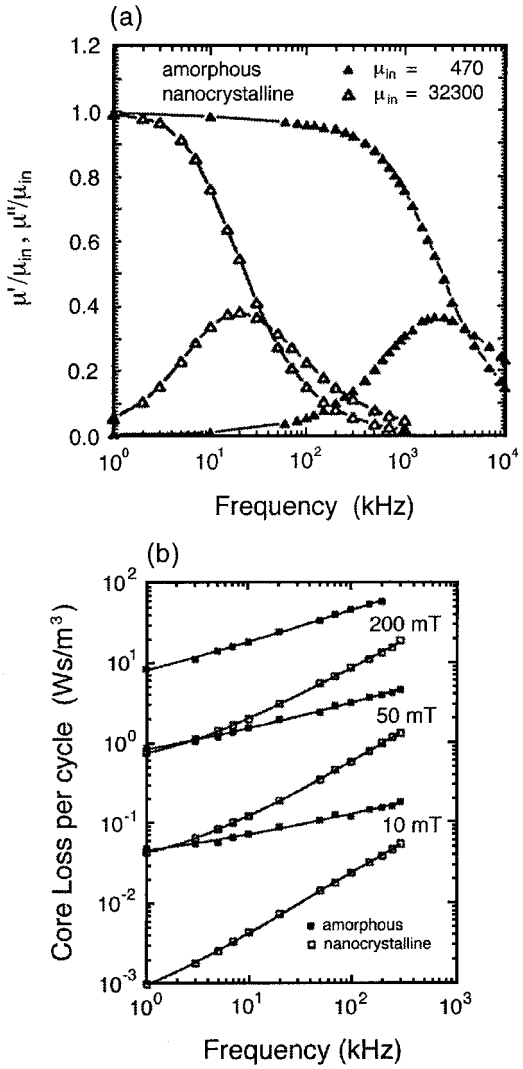

Fig. 63. (a) The real and imaginary components of the AC susceptibility for amorphous precursors and nanocrystalline FINEMET alloys and (b) comparison of the frequency dependence of the core losses for the same [235].

quenched in free volume and preferential longitudinal alignment of internal stresses.

Gonzalez et al. [69] have examined the influence of Joule heating anneals with simultaneous application of mechanical stress on the effective anisotropy and magnetostriction of $Fe_{73.5}Cu_1Ta_3Si_{13.5}B_9$ amorphous alloys of a FINEMET composition. A maximum in the uniaxial magnetic anisotropy K_u occurred at an annealing temperature of 450°C and was correlated with initial crystallization. At larger temperatures K_u decreased as the nanocrystal spacing decreased and the magnetic coupling increased. The stress dependence of the magnetization work allowed for the separate determination of the magnetostrictive coefficients of the amorphous and nanocrystalline phases.

Schaefer and Dietzmann [238] have examined frequency dependent AC magnetic response of amorphous and nanocrystalline (FINEMET) $Fe_{74.5}Cu_{0.75}Nb_{2.25}Si_{13.5}B_9$ ribbons. In the amorphous material the frequency-dependent, low field amplitude permeability was strongly influenced by magnetic after effects. Fig. 63(a) illustrates the real and imaginary components of the AC susceptibility for of amorphous and nanocrystalline $Fe_{74.5}Cu_{0.75}Nb_{2.25}Si_{13.5}B_9$ ribbons and Fig. 63(b) compares the frequency dependence of the core losses for the same.

Zbroszcyk et al. [290,296,297] have examined the magnetic after-effect in nanocrystalline (FINEMET) $Fe_{73.5}Cu_1Nb_3Si_{13.5}B_9$, alloys with different amounts of as-quenched disorder. The as quenched disorder was varied through variation of the ribbon thickness between 15 and 25 μm. The magnetic susceptibility, coercivity and Fe partitioning were all influenced by the ribbon thickness. The magnetization was studied by magnetic after effect (MAE) measurements that showed that the initial susceptibility and disaccommodation phenomena were also sensitively dependent on as-quenched disorder.

Malkinski and Slawska-Waniewska [196] have observed the temperature dependence of Barkhausen noise in an $Fe_{66}Cr_8Cu_1Nb_3Si_{13}B_9$ FINEMET alloy. A similar T-dependence of the DC permeability and RMS Barkhausen noise was noted to support the notion that magnetization rotation plays an important role in the magnetization process.

Aranda et al. [7] have studied the approach to saturation in nanocrystalline FINEMET materials. The magnetization prior to saturation associated with reversible rotation was fitted to the law:

$$M(H) = M_s\left[1 - \frac{a_1}{H} - \frac{a_2}{H^2}\right] + bH^{1/2} \tag{76}$$

where the term a_2/H^2 was described as being a direct consequence of the random anisotropy model, and attributable to FeSi grains. The coefficient a_2 reflects the Herzer predicted effective magnetic anisotropy of the nanocrystalline material, whereas in amorphous alloys it is postulated as being caused by local stress and magnetoelastic coupling. Xiong and Ho [286] have examined the effective magnetic anisotropy, K_{eff} of FINEMET alloys annealed at various temperatures

Table 9
Experimental observations of primary and secondary crystallization temperatures, saturation induction, permeability, coercivity, Curie temperature, magnetostrictive coefficient, grain size, resistivity and annealing temperature for nanocrystalline alloys (NANOPERM) and amorphous precursors

Sample	T_{x1}	T_{x2}	B_s	μ_e	H_c	T_C	λ_s	t	ρ_e	T_a	Reference
	(K)	(K)	(T)		(A/m)	(K)	($\times 10^{-6}$)	(nm)	(μΩm)	(K)	
$Fe_{92}Zr_8$	804	900	1.62	2*k*	66			23		823	[262]
$Fe_{91}Zr_7B_2$	785	1024	1.70	14*k*	7.2			18		923	[146,258,260]
$Fe_{91}Zr_7B_2$	790	1030	1.67	27*k*	5.5			16		873	[262]
$Fe_{91}Zr_7B_2$	786	998		9*k*						923	[146]
$Fe_{90}Zr_7B_3$	825	1025	1.63	22*k*	5.6		−1.1	18	0.44	923	[158,191–194]
$Fe_{89}Zr_7B_4$	796	980	1.65	15*k*	7.4			19			[146,258]
$Fe_{89}Zr_7B_4$	792	983		8*k*						873	[146]
$Fe_{89}Zr_7B_4$	809										[164]
$Fe_{87}Zr_7B_6$	839	978		19*k*						723	[146]
$Fe_{87}Zr_7B_6$	835	981		6*k*						623	[147]
$Fe_{87}Zr_7B_6$	819										[164]
$Fe_{85}Zr_7B_8$	865	990		6*k*						673	[146]
$Fe_{85}Zr_7B_8$	861	993		19*k*						673	[146]
$Fe_{85}Zr_7B_8$	820										[164]
$Fe_{81}Zr_7B_{12}$	836										[164]
$Fe_{89}Zr_5B_6$			1.70	13*k*	8.3			16			[258]
$Fe_{86}Zr_5B_8Cu_1$	750	870	1.54				0.5	13		823	[247]
$Fe_{90}Zr_7B_2Cu_1$			1.65	17*k*	2.4			18			[259]
$Fe_{89}Zr_7B_3Cu_1$			1.64	34*k*	4.5		−1.1	18	0.51		[193,194]
$Fe_{87}Zr_7B_5Cu_1$			1.55	20*k*	3.5			17			[260]
$Fe_{86}Zr_7B_6Cu_1$	800	995	1.52	48*k*	3.2		1	10		873	[247,260,261]
$Fe_{86}Zr_7B_6Cu_1$	730–750										[71]
$Fe_{85}Zr_7B_6Cu_2$	791	993									[164]
$Fe_{83}Zr_7B_8Cu_2$	795	991									[164]
$Fe_{79}Zr_7B_{12}Cu_2$	806	986									
$Fe_{89}Zr_7B_3Pd_1$			1.62	30*k*	3.2						
$Fe_{88}Zr_7B_3Al_2$	805	1020	1.57	11*k*			0			873	[129]
$Fe_{86}Zr_7B_3Si_4$	815	1040	1.54	10*k*			0.5			873	[129]
$Fe_{87}Zr_7B_2Si_4$	810	1050	1.56	14*k*			0			873	[129]
$Fe_{89}Zr_7B_2Al_2$	800	1030	1.61	17*k*			0			873	[129]
$Fe_{88}Zr_7B_2Si_2Al$			1.55	12*k*			−1			873	[129]
$Fe_{87}Zr_7B_3Si_2Al$			1.52	11*k*			−0.5			873	[129]
$Fe_{86}Zr_9B_4Cu_1$	810	900									[247]
$Fe_{86}Zr_7B_6Cu_1$	795	990									[276]
$Fe_{86}Zr_7B_6Pd_1$	813	1000									[276]
$Fe_{86}Zr_7B_6Sb_1$	824	1030									[276]
$Fe_{86}Zr_7B_6Au_1$	827	1000									[276]
$Fe_{86}Zr_7B_6Pt_1$	847	1010									[276]
$Fe_{86}Zr_7B_6Ag_1$	838	1000									[276]
$Fe_{86}Zr_7B_6Ga_1$	846	1010									[276]
$Fe_{87}Zr_7B_6$	846	1000									[276]
$Fe_{86}Zr_7B_6Y_1$	862	1035									[276]
$Fe_{87}Zr_4Nb_3B_6$	802		1.50	3.5*k*	15.9					923	[259]

(continued on next page)

Table 9 (*continued*)

Sample	T_{x1}	T_{x2}	B_s	μ_e	H_c	T_C	λ_s	t	ρ_e	T_a	Reference
$Fe_{86}Zr_4Nb_3B_6Cu_1$	757		1.54	18*k*	3.7					923	[259]
$Fe_{86}Zr_{325}Nb_{3.25}B_{6.5}Cu_1$			1.61	110*k*	2.0		−0.3	9	0.56		[194]
$Fe_{856}Zr_{3.3}Nb_{3.3}B_{6.8}Cu_1$			1.57	160*k*	1.2		-0.3	8		0.56	[194]
$Fe_{84}Zr_{3.5}Nb_{3.5}B_8Cu_1$			1.53	120*k*	1.7		0.3	8	0.61		[194]
$Fe_{86}Zr_4Nb_3B_6Ni_1$	778		1.56	9.3*k*	5.7					923	[259]
$Fe_{86}Zr_4Nb_3B_6Pd_1$	771		1.54	9.8*k*	5.1					923	[259]
$Fe_{86}Zr_4Nb_3B_6Pt_1$	782		1.47	10*k*	7.7					873	[259]
$Fe_{86}Zr_4Nb_3B_6Au_1$	772		1.51	11*k*	6.1					923	[259]
$Fe_{84}Nb_7B_9$	800	1070	1.4	9.8*k*	220		0.4	8		923	[157]
$Fe_{84}Nb_7B_9$	800	1060	1.49	22*k*	8.0		0.1	22	0.58	923	[158,191,193,194]
$Fe_{84}Nb_7B_8Cu_1$	705	1045	1.48	16*k*	8.9					823	[260]
$Fe_{83}Nb_7B_9Cu_1$				37*k*	2.94					673	[142]
$Fe_{83}Nb_7B_9Ga_1$			1.48	38*k*	4.8			10	0.70		[193]
$Fe_{83}Nb_7B_9Ge_1$			1.47	29*k*	5.6		0.2	24	0.69		[193]
$Fe_{83}Nb_7B_9Cu_1$			1.52	49*k*	3.8		1.1	8	0.64		[193]
$Fe_{84}Nb_{3.5}Zr_{3.5}B_8Cu_1$			1.53	100*k*	1.7		0.3	19	0.61		[193]
$Fe_{85}Nb_{3.5}Hf_{3.5}B_7Cu_1$			1.44	92*k*	1.3		0.2	20	0.58		[193]
$Fe_{91}Hf_7B_2$			1.60	18*k*	4.1			18			[258]
$Fe_{91}Hf_7B_2$			1.65	15*k*	4.1			18			[260]
$Fe_{90}Hf_7B_3$			1.59	32*k*	4.5		−1.2	13	0.48		[194]
$Fe_{89}Hf_7B_4$	840	1030	1.59	32*k*	5.6		−1.2	17	0.48	923	[191,193]
$Fe_{87.9}Hf_{9.8}B_{2.3}$			1.40	1.4*k*			−0.75	15		873	[190]
$Fe_{87.9}Hf_{9.8}B_{2.3}$			1.65	1*k*			−1.2	19		923	[190]
$Fe_{90}Hf_7B_2Cu_1$	770	1022	1.60	18*k*	3.0					873	[260]
$Fe_{82}Ti_7B_{10}Cu_1$	707	997	1.39	20*k*	3.5					723	[260]
$Fe_{82}Ta_7B_{10}Cu_1$	736	1022	1.46	11*k*	8.9					923	[260]
$Fe_{78}Si_9B_{13}$			1.56	9*k*	2.4	688	27	20	1.37	648	[25,191,193,194]
$Fe_{73.5}Si_{13.5}B_9Nb_3Cu_1$			1.24	100*k*	0.53	873	2	18	1.15		[25,146,258,260,261]
$Fe_{81}Si_2B_{13}Nb_3Cu_1$			1.55	9*k*	12.8			18			[258,260]
$Fe_{56}Co_7Ni_7Zr_{10}B_{20}$	890		0.96	18*k*	2.41	567*gl*				750	[132]
$Fe_{60}Co_3Ni_7Zr_{10}B_{20}$	870				5						[132]
$Fe_{49}Co_{14}Ni_7Zr_{10}B_{20}$	895				11						[132]
$Fe_{46}Co_{17}Ni_7Zr_{10}B_{20}$	905				12						[132]
$Fe_{4.5}Co_{70.5}Si_{10}B_{15}$			0.88	70*k*	1.2	688*gl*	0	21	1.47		[193,194,218]
$Fe_4Co_{67}Mo_1Si_{17}B_{11}$			0.55	100*k*	0.3	483	< 0.2		1.35		[25]
$Fe_2Co_{74}Mn_4Si_{11}B_9$			1.0	2*k*	1.0	753	< 0.2		1.15		[25]
$Fe_{88.65}Co_{1.35}Zr_7B_3$			1.65	27*k*	4.2		0	19			[193]
$Fe_{88.2}Co_{1.8}Zr_7B_2Cu_1$			1.70	48*k*	4.2		−0.1	12	0.53		[194]
$Fe_{89.55}Ni_{0.45}Zr_7B_3$			1.62	34*k*	3.5			21			[193]
$Fe_6Co_{74}B_{20}$			1.18		2.8	700*g*	< 0.4				[218]
$Fe_3Co_{72}P_{16}Al_3B_6$			0.63		1.0	600*g*	0			573	[218]
					1						
$Fe_{39}Ni_{39}Mo_2Si_{12}B_8$			0.8	20*k*	2.0	533	8		1.35		[25]
$Fe_{63.5}Co_{35}Cr_{1.5}$			2.42	10*k*	80				0.28		[32]
$Fe_{50}Co_{50}$			2.45	5*k*	160				0.07		[32]
$Fe_{49}Co_{49}V_2$			2.40	60*k*	16				0.27		[32]
$Fe_{67}Co_{18}Si_1B_{14}$			1.80	1.5*k*	5.0	823	35		1.23		[25]

also by means of analysis of the approach to saturation of the magnetization. In the region of the approach to saturation, the magnetization coefficient corresponding to the coefficient a_2 in Eq. (76) can be related to Herzer's effective anisotropy, K_{eff}. Measuring the differential susceptibility as a function of field allowed for determination of a_2 and by inference K_{eff}. K_{eff} was observed to vary from 860 to 910 J/m^3 with increasing annealing temperature. This increase correlates with an increasing α-Fe(Si) nanocrystal grain size.

Tate et al. [268] have examined the influence of Al additions on nanostructure and soft magnetic properties of FINEMET alloys. They studied $Fe_{73.5-x}Al_xSi_{13.5}B_9Cu_1Nb_3$ alloys with $0 \leq x \leq 10$. A reduction in the (bulk-line) magnetocrystalline anisotropy for α-FeSi was used to explain a reduced coercivity in alloys with $2 < x \leq 8$. A nearly linear reduction in the induction was observed from 1.5 T ($x = 0$) to 0.9 T ($x = 10$) with Al addition. Alves et al. [6] have designed a device to measure saturation magnetostriction in ferromagnetic ribbons (width up to 30 mm, thickness 20 μm), based on the 'small-angle magnetization rotation' method. They have used saturation magnetostriction measurements to analyze, the evolution of composite structure (amorphous + crystalline) in for annealing between 450 and 600°C of nanocrystalline FINEMET $Fe_{73.5}Si_{15.5}B_7Cu_1Nb_3$ ribbons.

7.5.2. NANOPERM alloys

Table 9 summarizes experimental observations for NANOPERM alloys. This

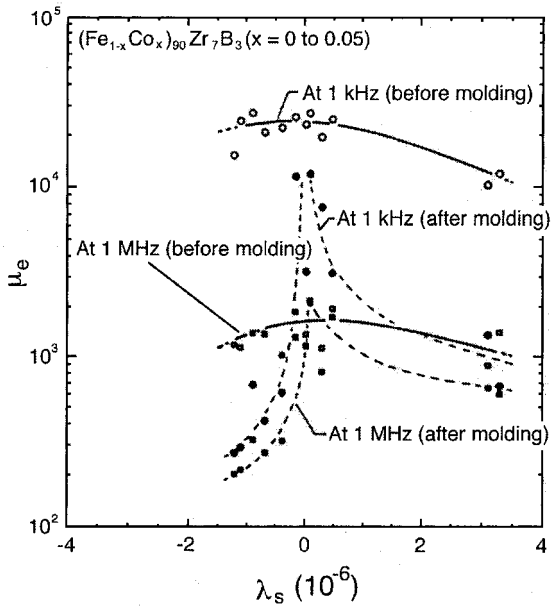

Fig. 64. Relationship between the saturation magnetostriction (λ_s) and permeability (μ_e) at 1 kHz and 1 MHz before and after compacting $Fe_{90}Zr_7B_3$ nanocrystalline alloys [193].

includes primary and secondary crystallization temperatures, saturation induction, permeability, coercivity, Curie temperature, magnetostrictive coefficient, grain size, resistivity and annealing for nanocrystalline alloys and amorphous precursors, as compiled from a selection of literature sources. Here we discuss pertinent observations made in some of these studies.

Suzuki et al. [258–260] described soft magnetic properties of $Fe_{91}Zr_7B_2$, $Fe_{87}Zr_7B_5Cu_1$ and $Fe_{86}Zr_7B_6Cu_1$ alloys. He stressed the significance of the decrease in the saturation magnetostriction (λ_s) in the nanocrystallization of the BCC α-Fe phase, in determining the soft magnetic properties. λ_s values smaller than 1 ppm were observed for these materials (Fig. 64). Shiga et al. [247] noted a departure from the D^6 dependence of the effective anisotropy at small nanocrystal size, in $Fe_{86}Zr_xB_{18-x}Cu_6$ alloys.

Kim et al. [144–148] examined the magnetic after effect (MAE) in a nanocrystalline $Fe_{88}Zr_7B_4Cu_1$ alloy. It was found that the intensity of a disaccomodation-based after effect decreased with increasing volume fraction of

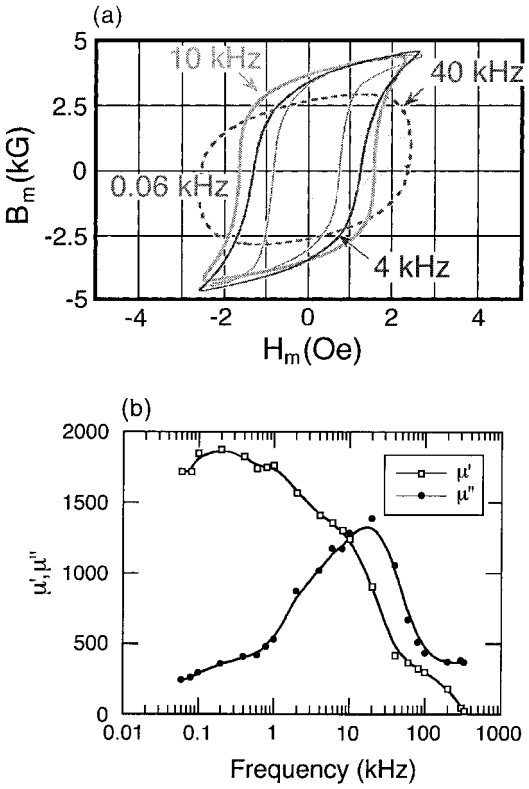

Fig. 65. AC hysteresis loops for the HITPERM alloy at 0.06, 4, 10, and 40 kHz. The sample was annealed at 650°C for 1 h and the measurements were made at room temperature with a field amplitude, $H_m = 2.5$ Oe [285].

the nanocrystalline α-Fe phase. The after-effect was therefore attributed to the residual amorphous phase.

Zhou and He [303] measured the effective magnetic anisotropy constant, K_{eff}, using fits of the law of approach to saturation of the magnetization for $Fe_{89}Zr_7B_4$ nanocrystalline soft magnetic alloys. K_{eff} between 879 and 1038 J/m^3 were reported for materials having 14-20 nm grains. A D^6 law was not observed for these materials. Suzuki et al. [263] have studied the structure, grain size and volume fraction of the residual amorphous phase for an amorphous $Fe_{91}Zr_7B_2$ alloy annealed for 60–10^5 s at temperatures between 823 and 973 K. He has used his data to construct time–temperature-transformation curves for the coercivity and permeability of these nanocrystalline alloys. The highest permeability (31,000) and lowest coercivity (4.2 A/m) was observed for an alloy annealed at 923 K for 60 s having a nanocrystalline grain size and ~35% volume fraction of the residual amorphous phase. These alloys showed K_{eff} to scale like D^3. This deviation from the D^6 dependence was explained in terms of a reduced dimensionality (i.e. between 2 and 3) within Hoffmann's ripple theory of the magnetic anisotropy. This reduced d is attributed to in-plane magnetic alignment.

Garcia-Tello et al. [64,65] have examined the compositional dependence of the effective magnetic anisotropy in $Fe_{93-x}Zr_7B_xCu_y$ ($x = 6$–8 and $y = 0$–2) nanocrystalline alloys. They conclude that an enhancement in soft magnetic properties occurs due to two factors: (1) low values of effective anisotropy associated with the onset of nanocrystallization and (2) decrease in the saturation magnetostriction. Cu additions are postulated as increasing the intergranular coupling due to a larger number of α-Fe nanocrystals in a coupled unit. This presumably reflects the role of Cu in the α-Fe nucleation process.

7.5.3. HITPERM alloys

Willard et al. [284] have measured permeability in an $Fe_{44}Co_{44}Zr_7B_4Cu_1$ HITPERM sample. The sample was prepared as a laminate in a toroidal geometry, and then annealed at 600°C to promote primary crystallization. AC permeability measurements were performed with a field amplitude of 2.5 Oe. Fig. 65(a) illustrates low field amplitude ($H_m = 2.5$ Oe) hysteresis loops measured at AC frequencies of 0.06, 4, 10, and 40 kHz, respectively. These are reasonably well fit by using a Raleigh loop model for maximum fields less than the AC coercivity. In the phenomenological Raleigh loop model, the hysteretic magnetic response can be modeled as:

$$B \pm B_m = \mu_i(H \pm H_m) \pm \nu(H \pm H_m)^2 \tag{77}$$

where H_m is the AC field amplitude, B_m is the induction at H_m, μ_i is the initial permeability and $\nu = \partial\mu_i/\delta H$. The hysteretic contribution to the core loss increases as H_m^3 until saturation. Field annealing during primary crystallization, should promote square loops and increase the low field induction of the material. With the low coercivity up to high frequencies, these materials show great promise if properly optimized for many of the applications being pursued with FINEMET

and NANOPERM. More significantly, many of the high temperature applications discussed in Section 8 do not have as stringent requirements for permeabilities. Finally, it is well know that permeability, magnetostrictive coefficents, etc. decrease as a function of temperature, further buoying the possibility of HITPERM as a high temperature material.

Fig. 65(b) illustrates the frequency dependence of the real and imaginary components of the complex permeability, μ' and μ'', respectively. μ'' reflects the power loss due to eddy currents and hysteretic response. The maximum permeability for this material was determined to be 1800. $\mu''(T)$ peaks at a frequency of ~20 kHz. The high peak frequency is thought to be reflective of the higher resistivity in the nanocrystalline materials than that of the conventional alloys and the AC losses reflect domain wall in a viscous medium. The larger resistivity ($\rho_e = 50$ μΩ cm at 300 K) extends the large permeability to higher frequencies where eddy currents (classical and those due to domain wall motion) dominate the losses. The resistivity of the nanocrystalline materials is intermediate between the amorphous precursor and crystalline materials of similar composition. The resistivity is a significant term in eddy current related damping of domain wall motion.

Iwanabe et al. [134] have studied nanocrystalline $(Fe_{1-x}Co_x)_{88}Hf_7B_4Cu_1$ alloys as candidates of soft magnetic materials for internal generators in a MORE electric aircraft. The materials are to be used in a high temperature atmosphere (500–600°C) and are expected to have (a) a 2 T or higher induction at the working temperature, 500°C; (b) thermal stability at 600°C for 5000 h; (c) core losses less than 480 W/kg at 5 kHz and 500°C. The ferromagnetic exchange length of an equiatomic ordered Fe–Co alloy was estimated as 46 nm by assuming $A = 1.7 \times 10^{-11}$ J/m and K = 8 kJ/m^3. If a larger anisotropy is assumed (for a 30% Co alloy, i. e. $K \sim 25$ kJ/m^3), but all other parameters are equivalent to the equiatomic alloy, an exchange length of 26 nm is predicted. The two numbers bracket Herzer's estimate of 35 nm for Fe–Si alloy. For grain smaller than the exchange length a random anisotropy model should be considered. Here the anisotropy is replaced with the effective anisotropy that is a statistical (random walk) average over grains coupled within an exchange length. The Herzer analysis predicts that a material with a ~30 nm grain size should be expected to have an ~100 A/m coercivity, which is comparable with Iwanabe's data. Coercivities on the order of 10^{-2} A/m are predicted for 10 nm particles suggesting that further refinement of grain size could result in even softer magnets.

8. Applications of amorphous and nanocrystalline materials

8.1. Amorphous materials

Luborsky [181,182] surveyed potential magnetic application of amorphous alloys. The key beneficial feature of amorphous alloys lied in their low losses but this was at the price of lower inductions (see also Refs.[66,221,227]). The standard

for power devices at the time was Fe-3.2% Si steel that has a $4\pi M_s$ of 2.0 T. In comparison $Fe_{80}B_{20}$ had only a 1.6 T value of $4\pi M_s$. Device applications that were considered included power transformers, magnetic shields, acoustic delay lines, tensile stress transducers and transverse filters. Warlimont [280] and Boll and Warlimont [24] surveyed the properties of amorphous magnetic alloys with respect to applications in electronics. In particular, saturation inductions, permeabilities, hysteretic and eddy current losses and magnetoelastic properties were considered. Applications for amorphous magnets that were suggested included:

1. 400 Hz power transformers;
2. Inductive components for switched mode power supplies;

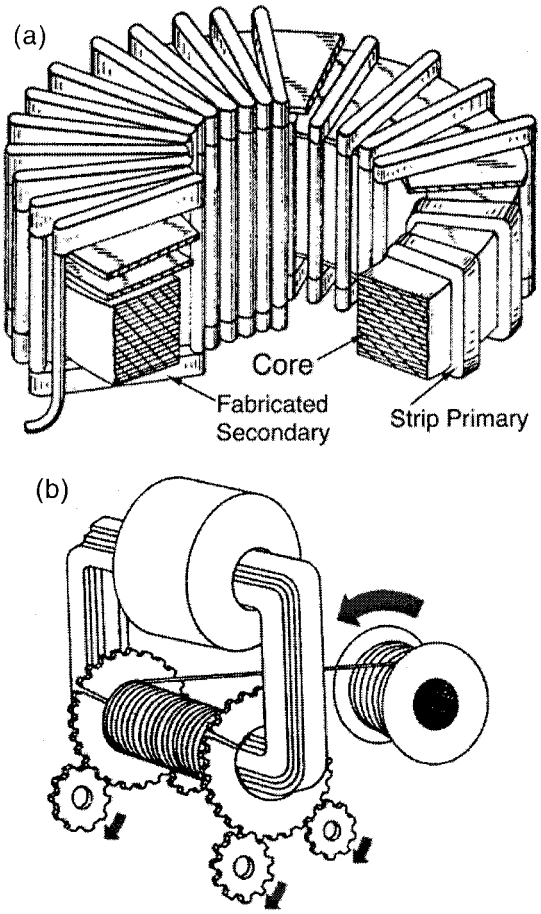

Fig. 66. (a) 60 Hz distribution, and (b) ribbon wound cruciform distribution transformer applications [256].

3. Magnetic shields;
4. Magneto-elastic transducers;
5. Magnetic heads for data storage applications and
6. Magnetic springs.

Materials requirements for conventional magnetic heads (as opposed to giant magnetoresistive heads) include: (a) large permeabilities, (b) large saturation inductions, (c) large electrical resistivities, mechanical hardness and wear resistance. Smith [269] marked ten years of amorphous magnetic applications. Among the applications he discussed for amorphous magnetic materials were the 60 Hz and cruciform distribution transformers illustrated in Fig. 66.

8.2. Nanocrystalline materials

8.2.1. FINEMET alloys

Yoshizawa et al. [290,291] have shown that the attenuation of pulse voltages in choke coils was improved using FINEMET cores as compared with Fe-based amorphous and Mn–Zn ferrite materials. These choke coils can be used over a wide frequency range as well as for protection from high voltage noise caused by lightning. Fig. 67 illustrates the frequency dependence of the permeability for a FINEMET material as compared with an Fe-based amorphous material and with Mn–Zn ferrites.

8.2.2. NANOPERM alloys

Makino et al. [189] have reported a core loss of 0.066 W/kg at 1 T and 50 Hz

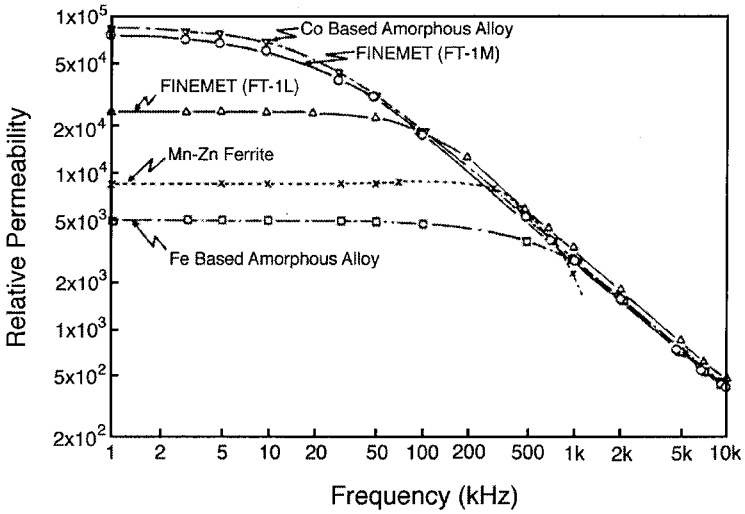

Fig. 67. Frequency dependence of the permeability for a FINEMET material as compared with an Fe-based amorphous material and with Mn–Zn ferrites [290,291].

for nanocrystalline $Fe_{86}Zr_7B_6Cu_1$. These values were shown to compare favorably with amorphous $Fe_{78}Si_9B_{13}$ and crystalline Fe-3.5% Si steels used as transformer core materials, as were the saturation inductions and permeabilities. They suggested these materials for applications as transformer core materials, including high frequency transformers, in which amorphous Fe–Si–B alloys have found a niche.

Makino et al. [193] have discussed the advantages of thermal stability and higher inductions of NANOPERM materials for magnetic device applications. Nanocrystalline alloys films have been proposed as core materials for thin-film magnetic heads as well as high frequency transformers and inductors. Makino et al. [194,195] have enumerated applications for NANOPERM alloys as including:

1. power transformers;
2. common-mode choke coils;
3. pulse-transformers; and
4. flux gate magnetometers.

NANOPERM has permeabilities of 1.6×10^5 which are comparable to FINEMET alloys and zero magnetostrictive Co-based amorphous alloys. Saturation inductions of more than 1.57 T are comparable or exceeding amorphous Fe-based alloys.

Naitoh et al. [213] have described the application of NANOPERM alloys to choke coils. A choke coil is an active filter used to prevent signal distortion in the reactor elements of phase modifying equipment. They provide line current corrections in all current signals. The core material of a choke coil needs large saturation induction, B_s and low core losses as well as small magnetostrictive coefficients. NANOPERM having B_s values comparable to amorphous Fe–Si–B [89] and lower losses allows for significant reduction of the core volume and consequently the choke coil dimensions. Fig. 68 shows a schematic of a laminated transformer core and (b) toroidal choke coil core.

8.2.3. HITPERM alloys

FeCo alloys have figured prominently in high temperature magnetic applications in space power systems [11,36]. Keuser et al. [141] reviewed magnetic alloys for applications in high temperature space power systems. More recently, Weichold et al. [223,283] have surveyed materials (bulk materials) for 300–500°C applications as magnetic components. Applications included core materials and winding wires for audio and radio frequency transformers. Alloys based on Fe–Co (Permendur and Supermendur) figured prominently in their analysis. The development of high temperature soft magnetic materials for jet engine applications is at the forefront of current development needs. The goal of developing a more electric plane [242] is driven by the strong impetus for weight reduction and performance enhancement associated with replacement of fluid systems used for cooling with electronic systems and air cooling. These electronic systems have components in which magnetic materials figure prominently. This necessitates the development of magnets capable of operating at significantly higher temperatures.

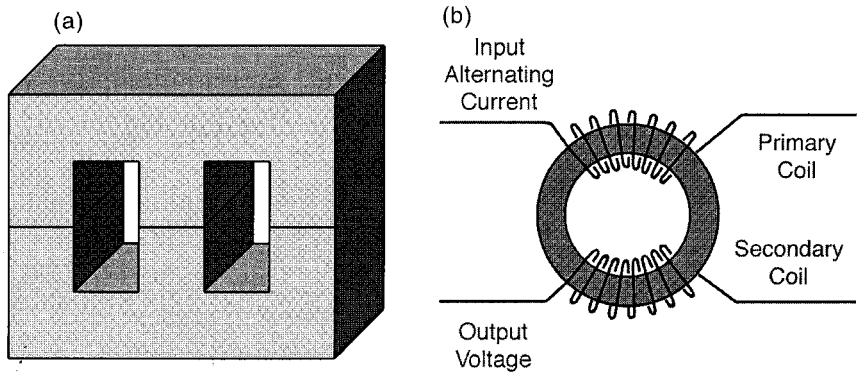

Fig. 68. (a) Schematic of a laminated transformer core and (b) toroidal choke coil core.

As illustrated in Fig. 69, the more electric aircraft integrated power unit (MEA–IPU) is a specific example of a component in which bulk magnets, both hard and soft, are important. Such materials are critical to power generation, in power inversion (transformers), in magnetic bearings and magnetomechanical actuators. In the MEA–IPU, soft FeCo alloy laminate stacks are incorporated in the rotor and hard magnets in the IPU bearings. Operation of the IPU at the higher temperatures associated with air cooling requires materials with excellent high

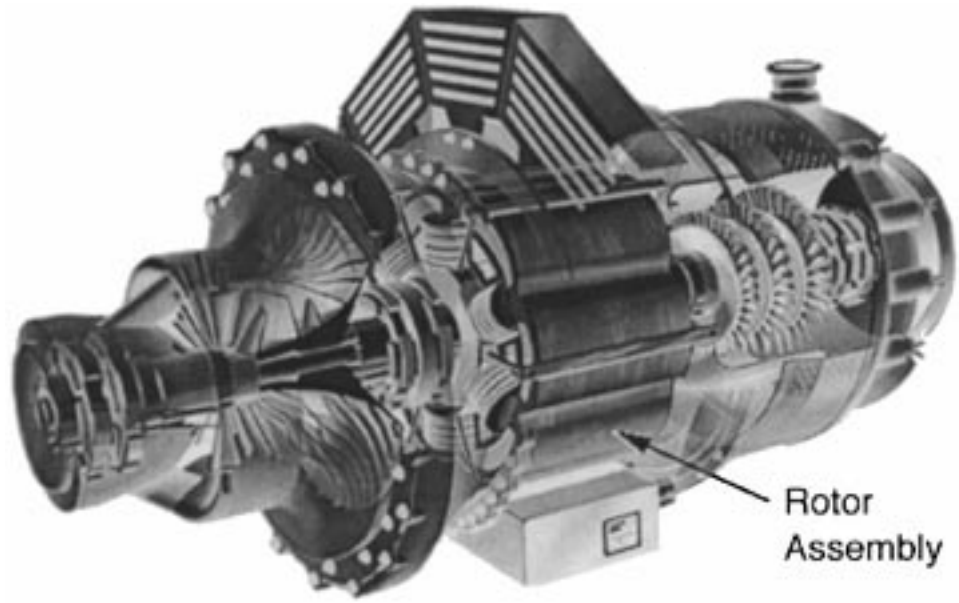

Fig. 69. More-Electric Aircraft Integrated Power Unit (MEA–IPU) (courtesy G. Hoffman WPAFB [38].

temperature magnetic and mechanical properties. Realization of this exciting potential will require:

1. Development of high permeability, large saturation and remanent induction, low-loss and (hysteretic and eddy current) soft magnets capable of operating at higher temperatures.
2. Development of high energy product permanent magnets capable of operating at high temperatures.
3. Improved mechanical properties and corrosion resistance at higher operating temperatures.
4. Development of new magnetic device geometries which exploit the new materials.

Nanocrystalline materials have been suggested for use in the soft magnet rotor applications of the MEA–IPU unit [134,203,285]. Turgut et al. [271] have described initial efforts aimed at producing FeCo nanoparticles for use as precursors for such novel soft magnetic materials. Soft magnetic properties require that nanocrystalline grains be exchange coupled and therefore any of the processing routes based on powder production must be coupled with a compaction method in which the magnetic nanoparticles end up exchange coupled. Nanocrystallization of amorphous precursors will also require compaction to produce shapes (laminate) and to improve mechanical properties, as ribbons are quite brittle after nanocrystallization.

The soft magnetic properties required for rotor applications in the more electric aircraft are in some sense less restrictive than those for the applications of FINEMET and NANOPERM described above. Permeabilities of 10^2–10^3 are sufficient for this application. The frequency requirements, based on 10,000 rpm rotor speeds and 6 flux changes per cycle, require these permeabilites to only 1 kHz. On the other hand, large inductions at temperatures between 500 and 600°C are an important requirement which seemingly eliminates all but Co or FeCo based alloys from consideration. Further, mechanical integrity at these temperatures in an extremely important consideration since rotational stresses and creep, at these elevated temperatures, must be a significant consideration in the design of these components [56,57].

9. Conclusions

Since the early discoveries of magnetic amorphous metallic glasses, their promise for soft magnetic applications has continued to be exploited. Recently, however, a revolution in the understanding of magnetic properties on a nanoscale and the discovery of exciting new nanocrystalline magnetic materials has led to new vistas for applications of these soft magnetic materials. It appears that a significant need for state of the art applications of soft magnetic materials will include high temperature performance of soft magnetic materials. Promising initial results on HITPERM alloys suggest that they might also find their way in high

temperature soft magnetic applications. The playground of microstructural engineering of soft magnetic properties will undoubtedly offer new discoveries for future materials scientists and engineers.

Acknowledgements

MEM thanks the National Science Foundation for support through NYI award DMR-9258450, grant award DMR-95000313 and grant award DMR-9803700. DEL acknowledges support from a NEDO grant. This material reviewed here is also based in part on work supported by the CMU Data Strorage Systems Center through the National Science Foundation under Grant No. ECD - 8907068. Efforts reviewed here have also been sponsored by the Air Force Office of Scientific Research, Air Force Material Command, USAF, under grant number F49620-96-10454. The assistance of the CMU SURG program, and the participation of the CMU Buckyball Project members have been invaluable.

The authors acknowledge helpful discussions with Prof. Henry Piehler, Prof. W. Ed Wallace, Prof. Anthony Rollett, Prof. Sara Majetich, Prof. David Lambeth, Dr. R. C. O'Handley, Dr. Sury Sankar, Dr. John Henry Scott, Dr. Vince Harris, Mr. Mark Storch, Mr. Hiro Iwanabe, Dr. Bin Lu, Ms. Katie Gallagher, Mr. Vladimir Zabenkin, Mr. Zafer Turgut, Dr. Shaoyan Chu, Dr. Mei-Qing Huang.

References

[1] Akai H, Akai M, Blugel S, Zeller R, Dederichs PH. J Mag Mag Mat 1984;45:291.
[2] Alben R, Budnick J, Cargill III GS. In: Metallic glasses. Metals Park: OH:ASM, 1978. p. 304.
[3] Alben R, Becker JJ, Chi MC. J Appl Phys 1978;49:1653.
[4] Al-Haj M, Barry J, Olofinjana A. Mat Lett 1997;33:107.
[5] Allia P, Baricco M, Tiberto P, Vinai F. J Appl Phys 1993;74:3137.
[6] Alves F, Houée P, Lécrivain M, Mazaleyrat F. J Appl Phys 1997;81:4322.
[7] Aranda GR, Gonzalez J, Kulakowski K. J Appl Phys 1998;83:6341.
[8] Ayers JD, Konnert JH, Dantonio P, Pattnaik A, Vold CL, Jones HN. J Mat Sci 1995;30:4492.
[9] Ayers JD, Harris VG, Sprague JC, Elam WT. Appl Phys Lett 1994;64:974.
[10] Ayers JD, Harris VG, Sprague JC, Elam WT, Jones HN. Acta Mater 1998;46:1861.
[11] Barranger JP. NASA Technical Note, NASA TND-3693, 1966.
[12] Bean CP, Livingston JD. J Appl Phys 1959;30:120S.
[13] Benjamin JS, Bamford MS. Met Trans 1977;A8:1301.
[14] Bernal JD. Nature (London) 1960;185:68.
[15] Bernal JD. Liquids: structure properties, solid interactions. New York: Elsevier, 1965.
[16] Bertotti G, Ferrara E, Fiorillo F, Tiberto P. Mat Sci Eng 1997;A226–228:603.
[17] Bethune DS, Johnson RD, Salem JR, de Vries MS, Yannoni CS. Nature 1993;366:123.
[18] Bhatnagar AK, Bhanu Prasad B, Jagannathan R. Phys Rev 1984;B 29:4896.
[19] Bigot J, Lecaude N, Perron JC, Milan C, Ramiarinjaona C, Rialland JF. J Mag Mag Mat 1994;133:299.
[20] Birgeneau RJ, Tarvin JA, Shirane, G, Gyorgy EM, Sherwood, RC, Chen HS, et al. Phys Rev 1978;B18:2192.
[21] Bitoh T, Nakazawa M, Makino A, Inoue A, Masumoto T; J Appl Phys 1999;85:5127.
[22] Blatter A, Von Allmen M. Phys Rev Lett 1985;54:2103.

[23] Boettinger WJ. In: Kear BH, Giessen BC, Cohen M, editors. Rapidly solidified amorphous and crystalline alloys. New York: Elsevier, 1982.
[24] Boll R, Warlimont H. IEEE Trans Mag 1981;17:3053.
[25] Boll R. Soft magnetic metals and alloys. In: Buschow KHJ, editor. Materials science and technology, a comprehensive treatment, vol. 3B, 1994, p. 399 [chapter 14].
[26] Boulos MI. Pure Appl Chem 1985;57:1321.
[27] Boulos MI. J High Temp Mat Process 1997;1:17.
[28] Bozorth RM. Ferromagnetism. New York: van Nostrand, 1951.
[29] Brown GW, Hawley ME, Markiewitz DJ, Spaepen F, Barth EP. J Appl Phys 1999;85:4415.
[30] Brzozka K, Slawska-Waniewska A, Jezuita K. J Mag Mag Mat 1996;160:255.
[31] Buttino G, Poppi M. J Mag Mag Mat 1997;170:211.
[32] Chen CW. Magnetism and metallurgy of soft magnetic Materials. New York: Dover Publications, 1986.
[33] Chen HS. Rep Prog Phys 1980;43:353.
[34] Chien CL. Phys Rev 1978;B 18:1003.
[35] Chikazumi S. Physics of magnetism. Malabar, FL: Kreiger, 1978.
[36] Chu S-Y, Huang M-Q, Kline C, McHenry ME, Cross JO, Harris VG. J Appl Phys 1999;85:6031.
[37] Coey JMD. Rare-earth iron permanent magnets. Oxford: Oxford Science Publications, Clarendon Press, 1996.
[38] Colegrove PG. AIAA paper No. 93-1188, 1993, p. 5.
[39] Conde CF, Conde A. Mat Lett 1994;21:409.
[40] Corb BW, Grant NJ, O'Handley RC. J Appl Phys 1982;53:7728.
[41] Corb BW. Phys Rev B 1985;31:2521.
[42] Cserei A, Jiang J, Aubertin F, Gonser U. J Mat Sci 1994;29:1213.
[43] Cullity BD. Introduction to magnetic materials. Reading, MA: Addison-Wesley, 1972.
[44] Cullity BD. Elements of X-ray diffraction. Reading, MA: Addison-Wesley, 1978.
[45] Dahlgren M, Grossinger R, Hernando A, Holzer D, Knobel M, Tiberto P. J Mag Mag Mat 1996;160:247.
[46] Davies HA. In: Steed S, Warlimont H, editors. Rapidly quenched metals, vol. 1. Amsterdam: North Holland, 1985.
[47] Deriu A, Malizia F, Ronconi F, Vittori-Antisari M, King SM. J Appl Phys 1996;79:2296.
[48] Dravid VP, Teng MH, Host JJ, Elliot BR, Johnson DL, Mason TO, et al. US Patent No. 5472 749, 1995.
[49] Dravid VP, Host JJ, Teng MH, Elliot BR, Hwang J-H, Johnson DL, et al. Nature (London) 1995;374:602.
[50] Duhaj P, Svec P, Janickovic D, Matko I. Mat Sci Eng 1991;A133:398.
[51] Duwez P. J Am Inst Metall Eng 1951;191:765.
[52] Duwez P, Willens RH, Klement W. J Appl Phys 1960;31:1136.
[53] Duwez P. Trans Am Soc Met 1967;60:607.
[54] Duwez P. Ann Rev Mat Sci 1976;6:83.
[55] Efthimiadis KG, Achilleos CA, Chadjivasiliou SC, Tsoukalas IA. J Mag Mag Mat 1997;171:141.
[56] Fingers RT, Kozlowski G. J Appl Phys 1997;81:4110.
[57] Fingers RT, Coate JE, Dowling NE. J Appl Phys 1999;85:6037.
[58] Fujii Y, Fujita H, Seki A, Tomida T. J Appl Phys 1991;70:6241.
[59] Fujimori H, Morita H, Obi Y, Ohta S. In: Levy RA, Hasegawa R, editors. Amorphous magnetism II. New York: Plenum Press, 1977. p. 393.
[60] Gallagher K, Johnson F, Kirkpatrick E, Scott JH, Majetich S, McHenry ME. IEEE Trans Mag 1996;32:4842.
[61] Gallagher KA, Willard MA, Zabenkin VN, Laughlin DE, McHenry ME. J Appl Phys 1999;85:5130.
[62] Gao YQ, Wang W, Zheng FQ, Liu X. J Non-Cryst Solids 1986;81:135.
[63] Gao YQ, Wang W. J Non-Cryst Solids 1986;81:129.
[64] Garcia-Tello P, Blanco JM, Zuberek R, Murillo N, Gonzalez J, Slawska-Waniewska A, et al. IEEE Trans Mag 1997;33:3919.

[65] Garcia Tello P, Blanco JM, Murillo N, Gonzalez J, Zuberek R, Slawska-Waniewska A, et al. J Appl Phys 1998;83:6338.
[66] Gilman JJ. Phys Today 1975;28:46.
[67] Gleiter H. Prog Mat Sci 1989;33:223.
[68] Gomez-Polo C, Holzer D, Multigner M, Navarro E, Agudo P, Hernando A, Vazguez M. Phys Rev B 1996;53:3392.
[69] Gonzalez J, Murillo N, Blanco JM, Gonzalez JM, Kulik T. J Appl Phys 1994;76:1131.
[70] Gonzalez JM, Murillo N, Gonzalez J, Blanco JM, Echeberria J. J Mat Res 1996;11:512.
[71] Gorria P, Orue I, Plazaola F, Fernandez-Gubieda ML, Barandiaran J. IEEE Trans Mag 1993;29:2682.
[72] Gorria P, Garitaonandia JS, Barandiaran JM. J Phys Condens Mat 1996;8:5925.
[73] Grabias A, Kopcewicz M. Mat Sci Forum 1998;269–272:725.
[74] Graf T, Kopcewicz M, Hesse J. J Mag Mag Mat 1995;140–144:423.
[75] Graf T, Kopcewicz M, Hesse J. Nanostructured Mat 1995;6:937.
[76] Gubanov VA, Liechtenstein AI, Postnikov AV. Magnetism and the electronic structure of crystals. Berlin: Springer–Verlag, 1992.
[77] Guinier A, Dexter DL. X-ray studies of materials. New York: Interscience Publishers, 1963.
[78] Hajko V, Csach K, Pan S, Danilenko N. Nanostructured Mat 1997;8:961.
[79] Hampel G, Pundt A, Hesse J. J Phys Condens Matter 1992;4:3195.
[80] Handrich K. Phys Stat Solidi 1969;32:K55.
[81] Haruyama O, Asahi N. Mat Sci Forum 1992;88-90:333.
[82] Harris R, Plischke M, Zuckermann MJ. Phys Rev Lett 1973;31:160.
[83] Harris R, Zobin D. J Phys F: Metal Phys 1977;7:337.
[84] Hasegawa R. J Appl Phys 1970;41:4096.
[85] Bertotti G. J Non-cryst Solids 1984;61/62:725.
[86] Hasegawa R. J Appl Phys 1985;57:2110.
[87] Hasegawa N, Saito M. IEICE Technical Report, MR89-12, 1989.
[88] Hasegawa N, Kataoka N, Fujimori H, Saito M. J Appl Phys 1991;70:6253.
[89] Hasegawa N, Saito M, Kataoka N, Fujimori H. J Mat Eng Perf 1993;2:181.
[90] Bertolli G, Makino A, Inoue A, Masumoto T. J Mag Mag Mat 1996;160:249.
[91] Herber RH. Mossbauer effect. In: McGraw-Hill encyclopedia of physics. New York: McGraw-Hill, 1982.
[92] Hernando A, et al. Symposium on Magnetic Properties of Amorphous Metals. Amsterdam: North-Holland, 1987.
[93] Hernando A, et al. Rapidly solidified alloys. Libermann, 1988.
[94] Hernando A, Kulik T. Phys Rev B 1994;49:7064.
[95] Hernando A, Navarro I. In: Hadjipanyis GC, Siegel RW, editors. Nanophase materials. The Netherlands: Kluwer, 1994. p. 703.
[96] Hernando A, et al. Phys Rev B 1995;51:3281.
[97] Hernando A, Vazquez M, Kulik T, Prados C. Phys Rev B 1995;51:3581.
[98] Hernando A, Marin P, Vazquez M, Herzer G. J Mag Mag Mat 1998;177–181:959.
[99] Herzer G, Hilzinger HR. J Mag Mag Mat 1986;62:143.
[100] Herzer G, Hilzinger HR. Physica Scripta 1989;39:639.
[101] Herzer G. IEEE Trans Mag 1989;25:3327.
[102] Herzer G. IEEE Trans Mag 1990;26:1397.
[103] Herzer G. Mat Sci Eng A 1991;133:1.
[104] Herzer G. J Mag Mag Mat 1992;112:258.
[105] Herzer G, Warlimont H. Nanostructured Mat 1992;1:263.
[106] Herzer G. IEEE Trans Mag 1995;26:1397.
[107] Herzer G. Scripta Metall Mater 1995;33:1741.
[108] Herzer G. In: Buschow KHJ, editor. Handbook of magnetic materials, vol. 10. Amsterdam: Elsevier Science, 1997. p. 415 [chapter 3].
[109] Hihara T, Onodera H, Sumiyama K, Suzuki K, Kasuta A, Nishina Y, et al. Jpn J Appl Phys 1994;33:L24.

[110] Hilzinger HR, Hillmann H, Mager A. Phys Stat Sol 1979;A55:763.
[111] Hoffmann H. IEEE Trans Mag 1968;4:32.
[112] Hoffmann H. IEEE Trans Mag 1973;9:17.
[113] Hoffmann H. IEEE Trans Mag 1979;15:1215.
[114] Hoffmann H, Fujii T. J Mag Mag Mat 1993;128:395.
[115] Hoffmann B, Kronmuller H. Nanostructured Mat 1995;6:961.
[116] Hono K, Inoue A, Sakurai T. Appl Phys Lett 1991;58(19):2180.
[117] Hono K, Hiraga K, Wang Q, Inoue A, Sakurai T. Acta Metall Mater 1992;40:2137.
[118] Hono K, Zhang Y, Tsai AP, Inoue A, Sakurai T. Scripta Metall Mater 1995;32:131.
[119] Host JJ, Teng MH, Elliot BR, Hwang J-H, Mason TO, Johnson DL, et al. J Mat Res 1997;12(5):1268.
[120] Host JJ, Block JA, Parvin K, Dravid VP, Alpers JL, Sezen T, et al. J Appl Phys 1998;83:793.
[121] Inoue A, Zhang T, Masumoto T. Mat Trans JIM 1989;30:965.
[122] Inoue A, Yamanoto H, Masumoto T. Mat Trans JIM 1990;31:1021.
[123] Inoue A, Gook JS. Mat Trans JIM 1995;36:1180.
[124] Inoue A, Gook JS. Mat Trans JIM 1995;36:1282.
[125] Inoue A, Shinohara Y, Gook JS. Mat Trans JIM 1995;36:1427.
[126] Inoue A, Miyauchi Y, Makino A, Masumoto T. Mat Trans JIM 1996;37:78.
[127] Inoue A, Gook JS. Mat Trans JIM 1996;37:32.
[128] Inoue A, Park RE. Mat Trans JIM 1996;37:1715.
[129] Inoue A, Miyauchi Y, Makino A, Masumoto T. Mat Trans JIM 1996;37:78.
[130] Inoue A, Takeuchi A, Zhang T, Murakami A, Makino A. IEEE Trans Mag 1996;32:4866.
[131] Inoue A, Nishiyama N, Matsuda T. Mat Trans JIM 1996;37.
[132] Inoue A, Zhang T, Itoi T, Takeuchi A. Mat Trans JIM 1997;38:359.
[133] Inoue A, Zhang T, Koshiba H, Makino A. J Appl Phys 1998;83:6326.
[134] Iwanabe H, Lu B, McHenry ME, Laughlin DE. J Appl Phys 1999;85B:4424.
[135] Johnson WL. Prog Mat Sci 1986;30:81.
[136] Kaneyoshi T. Amorphous magnetism. Boca Raton, FL: CRC Press, 1984.
[137] Kane SN, Bhagat N, Gupta A, Varga LK. J Mag Mag Mat 1997;167:241.
[138] Kataoka N, Inoue A, Masumoto T, Yoshizawa Y, Yamauchi K. Jpn J Appl Phys 1989;28:L1820.
[139] Kemeny T, Balogh J, Farkas I, Kaptas D, Kiss LF, Pusztai T, et al. J Phys Condens Matter 1998;10:L221.
[140] Kempter K, Hoffmann H. Phys Stat Sol 1969;34:237.
[141] Keuser PE, Pavlovic DM, Laue DH, Clark JJ, Spewock M. NASA Special Publication, NASA SP-3043, 1967.
[142] Kim CS, Kim SB, Lee HM, Uhm YR, Kim KY, Noh TH, Ok HN. IEEE Trans Mag 1997;33:3790.
[143] Kim KS, Yu SC, Rao KV. J Appl Phys 1997;81:4649.
[144] Kim KS, Yu S-C, Kim K-Y, Noh T-H, Kang I-K. IEEE Trans Mag 1993;29:2679.
[145] Kim KY, Noh TH, Lee YH, Kang IK, Kang T. J Appl Phys 1993;73:6594.
[146] Kim KY, Noh TH, Kang IK, Kang T. Mat Sci Eng 1994;A179/A180:552.
[147] Kim SH, Matsuura M, Sakurai M, Suzuki K. Jpn J Appl Phys 1993;32:676.
[148] Kim SH, Pi WK, Noh TH, Kim HJ, Kang IK. J Appl Phys 1993;73:6591.
[149] Kissinger HE. J Res NBS 1956;57:217.
[150] Kneller EF, Hawig R. IEEE Trans Mag 1991;27:3588.
[151] Knoble M, Sinnecker JP, Sato Turtelli R, Rechenberg HR, Grossinger R. J Appl Phys 1993;73:6603.
[152] Kobe S. Phys Stat Solidi 1970;41:K13.
[153] Kobe S, Handrich K, Fiz. Tverd Tela (Leningard) 1971;13:887 [Sov Phys-Solid State 1971;13:734].
[154] Koch CC. Ann Rev Mat Sci 1986;30:81.
[155] Koch CC. Mat Sci Forum 1992;88–90:243.
[156] Kohlbrecher J, Wiedenmann A, Wollenberger H. Physica B 1995;213/214:579.

[157] Kojima A, Horikiri H, Kamamura Y, Makino A, Inoue A, Matsumoto T. Mat Sci Eng 1994;A179/A180:511.
[158] Kojima A, Horikiri H, Makino A, Kawamura Y, Inoue A, Matsumoto T. Mat Trans JIM 1995;36:945.
[159] Kopcewicz M. Struct Chem 1991;2:313.
[160] Kopcewicz M, Grabias A, Nowicki P, Mat Sci Eng A 1997;A226–228:515.
[161] Kopcewicz M, Grabias A. J Appl Phys 1996;80:3422.
[162] Kopcewicz M, Grabias A, Nowicki P, Williamson DL. J Appl Phys 1996;79:993.
[163] Kopcewicz M, Grabias A, Nowicki P. Mat Sci Eng 1997;A226–228:515.
[164] Kopcewicz M, Grabias A, Williamson DL. J Appl Phys 1997;82:1747.
[165] Kopcewicz M, Grabias A, Idzikowski B. J Mag Mag Mat 1998;177–181:1434.
[166] Kopcewicz M, Grabias A, Skorvanek I. J Appl Phys 1998;83:935.
[167] Koshiba H, Inoue A, Makino A. Nanostructured Mat 1997;8:997.
[168] Koster U, Schunemann U, Blank-Bewersdorff M, Brauer S, Sutton M, Stephenson GB. Mat Sci Eng 1991;A133:611.
[169] Koster U, Meinhardt J. Mat Sci Eng 1994;A178:271.
[170] Kouvel JS. In: Berkowitz E, Kneller E, editors. Magnetism and metallurgy, vol. 2A. New York: Academic Press, 1969. p. 523.
[171] Kratschmer W, Lamb LD, Fostiropoulos K, Huffman DR. Nature 1990;347:354.
[172] Kraus L, Haslar V, Duhaj P, Svec P, Studnicka V. Mat Sci Eng 1997;A226–228:626.
[173] Kuhrt C, Schultz L. J Appl Phys 1993;73:6588.
[174] Kulik T. Mat Sci Eng 1992;A159:95.
[175] Kulik T, Hernando A, Vazquez M. J Mag Mag Mat 1994;133:310.
[176] Lanotte L, Iannotti V. J Appl Phys 1995;78:3531.
[177] Lee SE, Ra HY, Yim TH, Kim WT. Mat Sci Forum 1995;179–181:121.
[178] Lim SH, Pi WK, Noh TH, Kim HJ, Kang IK. J Appl Phys 1993;73:865.
[179] Lim SH, Pi WK, Noh TH, Kim HJ, Kang IK. J Appl Phys 1993;73:6591.
[180] Liu T, Gao YF, Xu ZX, Zhao ZT, Ma RZ. J Appl Phys 1996;80:3972.
[181] Luborsky FE. In: Levy RA, Hasegawa R, editors. Amorphous magnetism II. New York: Plenum Press, 1997.
[182] Luborsky FE. IEEE Trans Mag 1978;14:1008.
[183] Luborsky FE. Amorphous metallic alloys. London: Butterworths, 1983.
[184] MacLaren JM, Crampin S, Vvedensky DD, Eberhart ME. Phys Rev Lett 1989;63:2586.
[185] MacLaren, JM, Schulthess TC, Butler WH, Sutton RA, McHenry ME. J Appl Phys 1999;85:4833.
[186] Mader S, Nowick AS. Appl Phys Lett 1965;7:57.
[187] Majetich SA, Artman JO, McHenry ME, Nuhfer NT, Staley SW. Phys Rev B 1993;48:16845.
[188] Majetich SA, Scott JH, Brunsman EM, McHenry ME, Nuhfer NT. In: Ruoff RS, Kadish KM, editors. Fullerenes: physics, chemistry, and new directions VI. Pennington, NJ: The Electrochemical Society, 1994. p. 1448.
[189] Makino A, Suzuki K, Inoue A, Masumoto T. Mat Trans JIM 1991;32:551.
[190] Makino A, Yamamoto Y, Hirotsu Y, Inoue A, Masumoto T. Mat Sci Eng 1994;A179/A180:495.
[191] Makino A, Suzuki K, Inoue A, Masumoto T. Mat Sci Eng 1994;A179/A180:127.
[192] Makino A, Suzuki K, Inoue A, Hirotsu Y, Masumoto T. J Mag Mag Mat 1994;133:329.
[193] Makino A, Inoue A, Masumoto T. Mat Trans JIM 1995;36:924.
[194] Makino A, Hatanai T, Naitoh Y, Bitoh T, Inoue A, Masumoto T. IEEE Trans Mag 1997;33:3793.
[195] Makino A, Hatanai T, Inoue A, Masumoto T. Mat Sci Eng 1997;A226–228:594.
[196] Malkinski L, Slawska-Waniewska A. J Mag Mag Mat 1996;160:273.
[197] Massalski T. Binary alloy phase diagrams, Materials Park, OH ASM International 1990.
[198] Malozemoff AP, Williams AR, Moruzzi VL. Phys Rev B 1984;29:1620.
[199] Matsuura M, Sakurai M, Kim SH, Suzuki K, Tomida T. J Phys Condens Matter 1995;7:7087.
[200] Mazaleyrat F, Faugieres JC, Rialland JF. J Mag Mag Mat 1996;159:L33.
[201] McHenry ME, Majetich SA, De Graef M, Artman JO, Staley SW. Phys Rev B 1994;49:11358.

[202] McHenry ME, Gallagher K, Johnson F, Scott JH, Majetich SA. Recent advances in the chemistry and physics of fullernes and related materials. In: Kadish KM, Ruoff RS, editors. PV 96-10, ECS Symposium Proceedings, Pennington, NJ, 1996. p. 703.
[203] McHenry ME, Subramoney S. New York: Wiley 1999 [in press].
[204] McHenry ME, Willard MA, Iwanabe H, Sutton RA, Turgut Z, Hsiao A, Laughlin DE. IUMRS 1998. Bull Mat Sci 1999 [in press].
[205] Mizushima T, Makino A, Inoue A. J Appl Phys 1998;83:6329.
[206] Moorjani K, D Coey JM. Magnetic glasses. Amsterdam: Elsevier, 1984.
[207] Moya J, Vazquez M, Cremaschi V, Arcondo B, Sirkin H. Nanostructure Mat 1997;8:611.
[208] Müller M, Mattern N, Illgen L. Z Metallkd 1991;82:895.
[209] Müller M, Mattern N, Illgen L. J Mag Mag Mat 1992;112:263.
[210] Murillo N, Gonzalez J, Blanco JM, Gonzalez JM. J Appl Phys 1996;79:5465.
[211] Naohara T. Acta Metall 1998;46:397.
[212] Naitoh Y, Bitoh T, Hatanai T, Makino A, Inoue A. J Appl Phys 1998;83:6332.
[213] Navarro I, Hernando A. J Mag Mag Mat 1994;133:306.
[214] Neel L. J Phys Radium 1954;15:225.
[215] Noh TH, Lee MB, Kim HJ, Kang IK. J Appl Phys 1990;67:5568.
[216] Noh TH, Pi WK, Kim HJ, Kang IK. J Appl Phys 1991;69:5921.
[217] O'Handley RC. IEEE Trans Mag MAG 1976;12:942.
[218] O'Handley RC, Megusar J, Sun S-W, Hara Y, Grant NJ. J Appl Phys 1985;57:3563.
[219] O'Handley RC. J Appl Phys 1987;62:R15.
[220] O'Handley RC. In: Levy RA, Hasegawa R, editors. Amorphous magnetism II. New York: Plenum Press, 1977. p. 379.
[221] Ohnuma M, Suzuki J, Funahashi S, Ishigaki T, Kuwano H, Hamaguchi Y. Physica B 1995;213/214:582.
[222] Pandey K, Weichold MH, Palmer DW. IEEE Trans Magn MAG 1980;16:749.
[223] Park JR, Suh SJ, Kim KY, Noh TH. IEEE Trans Mag 1997;33:3799.
[224] Perepesko JH, Paik JS. In: Kear BH, Giessen BC, Cohen M, editors. Rapidly solidified amorphous and crystalline alloys. New York: Elsevier, 1982.
[225] Pfeifer F, Radeloff C. J Mag Mag Mat 1980;19:190.
[226] Polk DE, Giessen BC, Gardner FS. Mat Sci Eng 1976;23:309.
[227] Pradell T, Clavaguera N, Zhu J, Clavaguera-Mora MT. J Phys Condens 1995;7:4129.
[228] Pundt A, Hampel G, Hesse J. J Phys Condens Matter 1992;87:65.
[229] Quigley RE. WPAFB, 1993.
[230] Rajkovic M, Buckley RA. Metal Sci 1981;15:21.
[231] Rixecker G, Schaaf P, Gonser U. J Phys Condens Matter 1992;4:10295.
[232] Rixecker G, Schaaf P, Gonser U. Phys Stat Solidi nA 1993;139:309.
[233] Russell KC, Aaronson HI. J Mat Sci 1991;10:1975.
[234] Saito Y, Okuda M, Yoshikawa T, Kasuya A, Nishina Y. J Phys Chem 1994;98:6696.
[235] Schafer M, Dietzmann G. J Mag Mag Mat 1994;133:303.
[236] Schaefer R, Hubert A, Herzer G. J Appl Phys 1991;69:5325.
[237] Schwarz RB, Johnson WL. Phys Rev Lett 1983;51:415.
[238] Schwarz RB, Koch CC. Appl Phys Lett 1986;49:146.
[239] Schwarz RB. Mat Sci Forum 1998;269-272:665.
[240] Scott JH, Majetich SA, Turgut Z, McHenry ME, Boulos M. In: Parker JC, editor. Nanostructured materials. MRS Symposium Proceedings. Pittsburgh, PA: Materials Research Society 1997;219:567.
[241] Scott JH, Turgut Z, Chowdary McHenry ME, Majetich SA. MRS Symposium Proceedings 1999;121:412.
[242] Scott JH, Chowdary K, Turgut Z, Majetch SA, McHenry ME. J Appl Phys 1999;85(8):4409.
[243] Shiga N, Kogiku F, Yukumoto M. Mat Trans JIM 1995;36:939.
[244] Skomski R, Coey JMD. Phys Rev B 1993;48:15812.
[245] Skorvanek I, O'Handley RC. J Mag Mag Mat 1995;140–144:467.

[246] Slawska-Waniewska A, Gutowski M, Lachowicz HK, Kulik T, Matyja H. Phys Rev B 1992;46:14594.
[247] Slawska-Waniewska A, Munoz JS, Nowicki P. J Mag Mag Mat 1996;160:251.
[248] Slawska-Waniewska A, Zuberek R. J Mag Mag Mat 1996;160:253.
[249] Slawska-Waniewska A, Greneche JM. Phys Rev B 1997;56:R8491.
[250] Smith CH. IEEE Trans Mag 1982;18:1376.
[251] Stolloff NS. Mat Res Soc Proc 1985;39:3.
[252] Suzuki K, Kataoka N, Inoue A, Makino A, Masumoto T. Mat Trans JIM 1990;31:743.
[253] Suzuki K, Makino A, Kataoka N, Inoue A, Masumoto T. Mat Trans JIM 1991;32:93.
[254] Suzuki K, Makino A, Inoue A, Masumoto T. J Appl Phys 1991;70:6232.
[255] Suzuki K, Kikuchi M, Makino A, Inoue A, Masumoto T. Mat Trans JIM 1991;32:961.
[256] Suzuki K, Makino A, Tsai AP, Inoue A, Masumoto T. Mat Sci Eng 1994;A179/A180:501.
[257] Suzuki K, Cadogan JM, Sahajwalla V, Inoue A, Masumoto T. J Appl Phys 1996;79:5149.
[258] Suzuki K, Cadogan JM. Phil Mag Lett 1998;77:371.
[259] Suzuki K, Cadogan JM. Phys Rev B 1998;58:2730.
[260] Suzuki K, Herzer G, Cadogan JM. J Mag Mag Mat 1998;177–181:949.
[261] Suzuki K, Cadogan JM. J Appl Phys 1999;85:4400.
[262] Tate BJ, Parmar BS, Todd I, Davies HA, Gibbs MRJ, Major RV. J Appl Phys 1998;83:6335.
[263] Tsuei CC, Duwez P. J Appl Phys 1960;37:435.
[264] Turgut Z, Huang M-Q, Gallagher K, Majetich SA, McHenry ME. J Appl Phys 1997;81:4039.
[265] Turgut Z, Scott JH, Huang MQ, Majetich SA, McHenry ME, J Appl Phys 1998;83:6468.
[266] Turgut Z, Nuhfer NT, Piehler HR, McHenry ME. J Appl Phys 1999;85(8)4406.
[267] Varga LK, Bakos E, Kiss LF, Bakonyi I. Mat Sci Eng 1994;A179/A180:567.
[268] Varga LK, Lovas A, Pogany L, Kiss LF, Balogh J, Kemeny T. Mat Sci Eng 1997;A226–228:740.
[269] Velisek J. Czech J Phys B 1970;20:250.
[270] Vojtanik P, Komova E, Petrovic P, Varga R, Sassik H, Grossinger R. Acta Phys Slovaca 1998;48:1.
[271] Vojtanik P, Matejko R, Varga R, Sassik H, Grossinger R. EMMA 1998.
[272] Warlimont H. Phys Technol 1980;11:28.
[273] Wang Z, He KY, He SL, Zhang YM, Fu YJ, Zhang L. J Mag Mag Mat 1997;171:300.
[274] Weichold MH, Pandey K, Palmer D. IEEE Trans Mag 1980.
[275] Williams A, Moruzzi VL, Malozemoff AP, Tekuta K. IEEE Trans Mag 1983;19:1983.
[276] Willard MA, Laughlin DE, McHenry ME, Thoma D, Sickafus K, Cross JO, et al. J Appl Phys 1998;84:6773.
[277] Willard MA, Huang M-Q, Laughlin, DE, McHenry, ME, Cross JO, Harris, VG, Frascetti, C, J Appl Phys 1999;85(8):4421.
[278] Xiong X-Y, Ho K-Y. J Appl Phys 1995;77:2094.
[279] Yavari AR, Desre PJ. Mat Sci Forum 1992;88-90:43.
[280] Yavari AR, Drbohlan O. Mat Trans JIM 1995;36:896.
[281] Yavari AR, Negri D. Nanostructured Mat 1997;8:969.
[282] Yoshizawa Y, Oguma S, Yamauchi K. J Appl Phys 1988;64:6044.
[283] Yoshizawa Y, Yamauchi K, Yamane T, Sugihara H. J Appl Phys 1988;64:6047.
[284] Yoshizawa Y, Yamauchi K. J Jpn Inst Met 1989;53:241.
[285] Yoshizawa Y, Yamauchi K. Mat Trans JIM 1990;31:307.
[286] Yoshizawa Y, Yamauchi K. Mat Sci Eng 1991;A133:176.
[287] Zbroszcyk J, Fukanaga H, Olszewski J, Ciurzynska WH, Hasiak A. J Mag Mag Mat 1996;160:277.
[288] Zbroszcyk J, Narita K, Olszewski J, Ciurzynska W, Lijun W, Wyslocki B, et al. J Mag Mag Mat 1996;160:281.
[289] Zbroszcyk J, Varga LK, Olszewski J, Ciurzynska W, Wyslocki B, Szymura S, et al. J Mag Mag Mat 1996;160:279.
[290] Zhang Y, Hono K, Inoue A, Sakurai T. Appl Phys Lett 1996;69:2128.
[291] Zhang Y, Hono K, Inoue A, Makino A, Sakurai T. Acta Mater 1996;44:1497.
[292] Zhang J, Wu B, Wu X, Wang G, Zhao J. J Appl Phys 1996;79:5473.

[293] Zhang XY, Zhang JW, Xiao FR, Liu JH, Liu RP, Zhao JH, Zheng YZ. Mat Lett 1998;34:85.
[294] Zhou XZ, Morrish AH, Naugle DG, Pan R. J Appl Phys 1993;73:6597.
[295] Zhou F, He KY. J Appl Phys 1996;79:8851.
[296] Zhu J, Clavaguera N, Clavaguera-Mora MT, Howells WS. J Appl Phys 1998;84:6565.
[297] Zuberek R, Murillo N, Gonzalez J, Blanco JM, Garcia-Tello P. Nanostructured Mat 1997;8:711.
[298] McHenry ME, Brunsman EM, Majetich SA. IEEE Trans Mag 1995;31:3787.
[299] Suzuki K, 1998 Private Communication.
[300] Willard MA, Gingras M, Lee M, Harris VG, Laughlin DE, McHenry ME. MRS Symposium I. Spring 1999 [in press].
[301] Hawley ME, Brown GW, Thoma DJ, Willard MA, McHenry ME. MRS Symposium I. Spring 1999 [in press].
[302] Makino A, Suzuki K, Inoue A, Masumoto T. Mat Trans 1992;JIM-33:80.